NUMERICAL SIMULATION OF DIFFERENTIAL RAILWAY TRACK SETTLEMENT

Chonlatis Charoenwong

Submitted in accordance with the requirements for the degree of
Doctor of Philosophy

The University of Leeds
Institute for High Speed Rail and Systems Integration
School of Civil Engineering

April 2024

Intellectual Property and Publication Statements

I confirm that the work submitted is my own, except where work which has formed part of jointly authored publications has been included. My contribution and the other authors to this work has been explicitly indicated below. I confirm that appropriate credit has been given within the thesis where reference has been made to the work of others.

Citation details	Charoenwong, C, Connolly, D.P., Woodward, P.K., Galvín, P., Alves Costa, P., 2022. Analytical forecasting of long-term railway track settlement. Computers and Geotechnics 143, 104601. https://doi.org/10.1016/j.compgeo.2021.104601
Contribution of the authors	C. Charoenwong: Methodology, Software, Writing D.P. Connolly: Conceptualization, Methodology Resources, Supervision P.K. Woodward: Supervision P. Galvín: Supervision P. Alves Costa: Supervision
Chapters in thesis	Chapter 5

Citation details	Charoenwong, C., Connolly, D.P., Odolinski, K., Alves Costa, P., Galvín, P., Smith, A., 2022. The effect of rolling stock characteristics on differential railway track settlement: An engineering-economic model. Transportation Geotechnics 37, 100845. https://doi.org/10.1016/j.trgeo.2022.100845
Contribution of the authors	C. Charoenwong: Methodology, Software, Validation, Writing-original draft, Writing – review & editing D.P. Connolly: Conceptualization, Methodology, Resources, Supervision, Writing – original draft, Writing – review & editing K. Odolinski: Methodology, Writing – original draft, Writing – review & editing P. Alves Costa: Supervision P. Galvín: Supervision A. Smith: Supervision
Chapters in thesis	Chapter 8

Citation details	Charoenwong, C., Connolly, D.P., Colaço, A., Alves Costa, P., Woodward, P.K., Romero, A., Galvín, P., 2023. Railway slab vs ballasted track: A comparison of track geometry degradation. Construction and Building Materials 378, 131121. https://doi.org/10.1016/j.conbuildmat.2023.131121
Contribution of the authors	C. Charoenwong: Methodology, Software, Formal analysis, Validation, Writing – original draft, Writing– review & editing D.P. Connolly: Conceptualization, Methodology, Resources, Supervision, Writing – original draft,

	Writing – review & editing A. Colaço: Supervision, Writing – original draft P. Alves Costa: Conceptualization, Supervision P.K. Woodward: Supervision A. Romero: Supervision P. Galvín: Supervision
Chapters in thesis	Chapter 6

Citation details	Charoenwong, C., Connolly, D.P., Costa, P.A., Galvín, P., Romero, A., 2024. The effect of ballast moisture content and fouling index on railway track settlement. Transportation Geotechnics 45, 101193. https://doi.org/10.1016/j.trgeo.2024.101193
Contribution of the authors	C. Charoenwong: Writing – review & editing, Writing – original draft, Validation, Software, Methodology, Investigation D.P. Connolly: Writing – review & editing, Writing – original draft, Supervision, Methodology P. Alves Costa: Supervision P. Galvín: Supervision A. Romero: Supervision
Chapters in thesis	Chapter 7

Thesis Outcomes

Parts of this thesis have been published in 3 journal papers and 5 conference papers.

Journal papers

1. Charoenwong, C, Connolly, D.P., Woodward, P.K., Galvín, P., Alves Costa, P., 2022. Analytical forecasting of long-term railway track settlement. Computers and Geotechnics 143, 104601. https://doi.org/10.1016/j.compgeo.2021.104601
2. Charoenwong, C., Connolly, D.P., Odolinski, K., Alves Costa, P., Galvín, P., Smith, A., 2022. The effect of rolling stock characteristics on differential railway track settlement: An engineering-economic model. Transportation Geotechnics 37, 100845. https://doi.org/10.1016/j.trgeo.2022.100845
3. Charoenwong, C., Connolly, D.P., Colaço, A., Alves Costa, P., Woodward, P.K., Romero, A., Galvín, P., 2023. Railway slab vs ballasted track: A comparison of track geometry degradation. Construction and Building Materials 378, 131121. https://doi.org/10.1016/j.conbuildmat.2023.131121
4. Charoenwong, C., Connolly, D.P., Costa, P.A., Galvín, P., Romero, A., 2024. The effect of ballast moisture content and fouling index on railway track settlement. Transportation Geotechnics 45, 101193. https://doi.org/10.1016/j.trgeo.2024.101193

Conference papers

1. Charoenwong, C., Connolly, D. P., Dong, K., Alves Costa, P., Soares, P. J., & Woodward, P. K. (2022). A Multi-model Approach to Analyse Railway Track-Ground Dynamics and Soil Nonlinearity. Lecture Notes in Civil Engineering, 165, 37–48. https://doi.org/10.1007/978-3-030-77234-5_4
2. Charoenwong, C., Connolly, D. P., Woodward, P. K., Galvín, P., & Alves Costa, P. (2022). Numerical modelling of the evolution of differential settlement of railway tracks. In Eleventh International Conference on the Bearing Capacity of Roads, Railways and Airfields, Volume 3 (pp. 291–300). CRC Press. https://doi.org/10.1201/9781003222910-30

3. Charoenwong, C., Connolly, D. P., Woodward, P. K., Galvín, P., & Alves Costa, P. (2022b). Modelling changes in railway vibration due to differential settlement. ICSV28 – The 28th International Congress on Sound and Vibration.
4. C. Charoenwong, D.P. Connolly, P.K. Woodward, P. Galvin, P. Alves Costa, "Modelling railway track differential settlement for prediction of future deterioration and maintenance intervals", in J. Pombo, (Editor), "Proceedings of the Fifth International Conference on Railway Technology: Research, Development and Maintenance", Civil-Comp Press, Edinburgh, UK, Online volume: CCC 1, Paper 8.9, 2022, doi:10.4203/ccc.1.8.9
5. Charoenwong, C., Connolly, D. P., Woodward, P. K., Galvín, P., & Alves Costa, P. (2022c). The effect of train type and timetable on differential railway track settlement. EURODYN2023 – XII International Conference on Structure Dynamics.

Acknowledgements

First and foremost, I wish to extend my sincere appreciation to Professor David Connolly, who acted as my main research supervisor, for his outstanding guidance and unwavering support during the entirety of this research endeavour. His boundless enthusiasm and unwavering dedication have been my enduring wellsprings of inspiration. His support was indispensable in accomplishing all of these

I would like to thank Professor Peter Woodward, my co-supervisor, for the invaluable guidance and constructive suggestions, particularly in developing the settlement formulation.

I would also like to extend my heartfelt gratitude to Dr. Pedro Galvin for providing detailed explanations and invaluable assistance during the development of the 2.5D FEM model. Additionally, I wish to express my appreciation to Dr. Pedro Alves Costa for his consistent guidance and support throughout the development of the track-track interaction model.

I would like to express my gratitude to all my co-authors: Dr. Kristofer Odolinski, Professor Andrew Smith, Dr. Aires Colaço, and Dr. Antonio Romero Ordóñez, for their supervision and assistance in revising the papers.

Special thanks to my colleagues Panudech Chumyen, Angie Lamprea Pineda, and Chutiphon Moranon, whose invaluable assistance and friendship provided crucial support in overcoming various research challenges throughout my PhD journey.

I wish to express my profound appreciation to the Royal Thai Government, the sponsoring organization of my PhD. Without their generous financial support, the successful completion of this project would not have been possible.

Finally, I am deeply indebted to my beloved family for their unwavering encouragement, sacrifices, and unwavering support throughout the duration of this project. They have consistently been my primary source of motivation, and I could not have completed this thesis without their enduring encouragement and support.

Abstract

Railway tracks undergo plastic settlement when subject to repeated train loading. This occurs differentially along the track rather than in a uniform manner, and the profile is a key parameter when scheduling track maintenance operations. Therefore, this thesis presents a novel numerical approach to predict track irregularity evolution. The model combines empirical settlement laws with finite element modelling, where the track-ground structure is modelled explicitly, and multi-body train-track interaction is considered. A 2.5D finite element approach with perfectly matched layers is used to simulate static and dynamic stress fields from trains. The stresses induced by the trains are solved using a hybrid frequency-wavenumber and time-space approach, considering non-linear track-soil material behaviour. The model has several novelties: 1) after every load passage, the track profile is updated before applying the next load, meaning the train-track interaction is constantly evolving; 2) new empirical settlement laws are derived that account for evolving train-track forces and track profiles; 3) full 3D stress fields in the track and ground are considered.

Firstly, the model development is described, before validating its prediction of track geometry evolution as captured from track recording vehicles. Next, the first analysis shows that modelling error is introduced if the geometry is not updated frequently (e.g. after every load passage). A parametric study also shows track subgrade material properties have a marked effect on track settlement. The second analysis investigates the train-induced differential settlement of ballast and non-ballasted tracks, considering typical modern intercity (200 km/h) and high speed (300km/h) lines. It is shown that the ballasted track exhibits higher train-induced differential settlement compared to the slab track and at higher linespeeds the degradation of track geometry is increasingly pronounced for the ballasted track. The next analysis introduces a novel equation for ballast settlement, considering the fouling index and moisture of fines. Moisture of fines is found to have a more significant impact on track deterioration than the fouling index. However, increased fines content contributes to moisture retention, exacerbating track settlement. Higher train speeds and lower earthwork stiffness’s make this effect more pronounced. Finally, a novel combined engineering-economic approach is proposed to investigate the effect of increasing train speeds, adding additional passenger movements, and adding additional freight movements to an existing line. It is shown that higher speeds result in higher dynamic forces and cause a faster rate of deterioration of track geometry, thus increasing marginal cost. The

model is then used to investigate the effect of adding additional train movements to a passenger line. It is shown that additional movements increase the rate of track degradation and marginal costs, particularly if the additional traffic is freight. This is because freight vehicles typically have only one layer of (stiff) suspension, thus generating elevated dynamic forces compared to passenger vehicles.

Table of Contents

List of Tables

List of Figures

Chapter 1
Introduction

The high-speed rail network is currently undergoing rapid expansion across continents worldwide. This expansion is driven by the need for fast and efficient mobility solutions. As a result, there have been various efforts to increase the speed of trains. Notably, Japan has developed its train reaching a top speed over 600 km/h, setting a new world record. However, increasing the train speed can cause several concerns, particularly in cost and safety aspects. With a very high train speed, the large vibrations generated along railway routes have become a primary concern. These vibrations are similar to the sonic boom caused by supersonic jets passing through the sound barrier and cause the train and track to shake (in a similar way to an earthquake). Over time, the cumulative impact of these vibrations leads to a progressive degradation of the track structure.

Taking into account cost and safety considerations, regular inspections and maintenance of railway tracks are essential to ensure that track quality remains within acceptable limits. The regularity of these inspections and maintenance are vital, however, they come with significant expenses. As such, methodologies that can predict potential track deterioration may serve as alternative strategies, effectively reducing costs while preserving track in optimal condition. If prediction methods indicate that track quality may approach the lower acceptable threshold, timely and precise inspection and maintenance action can be assigned to the appropriate track section.

Furthermore, when railway operators consider increasing linespeed, increasing the annual number of rolling stock movements, or changing track design, it is imperative to comprehend the subsequent implications these adjustments might have on track deterioration. In this context, numerical tools that encompass these multifaceted considerations stand as invaluable assets. They guide railway operators nuanced insights, enabling them to make investment decisions that are not only judicious but also future-proof.

1.1 Motivation of the research

Several factors from a scientific perspective have influenced the author's motivation to study the subject of this thesis.

Despite the very important advances achieved over the past decade by different authors, there were considerable gaps from a numerical point of view, which the author intends to contribute to solving. Regarding forecasting methodologies, the balance between computational efficiency and the accuracy of the results displayed by existing models presented important deficiencies. Despite notable computational progress, the use of powerful 3D numerical models requires an enormous computational effort, given the vastness of the domain to be analysed (Chumyen et al., 2023; Connolly et al., 2013). On the other hand, the semi-analytical methodologies proposed by most authors constitute efficient approaches from a computational point of view, however, they are limited when aiming for a more detailed analysis (Dong et al., 2018). Therefore, as is done in the present work, the development of numerical methodologies adapted to the context of the present study, namely through 2.5D techniques, proves to be a compromise solution, which makes it possible to obviate most of the limitations mentioned (Colaço et al., 2016). The Perfectly Matched Layers (PML) method is used to manage boundary effects resulting from the truncation of finite element meshes. Due to the similarity between the PML equations and those commonly used in finite element analysis, the compatibility of both methods is achieved without necessitating specialised numerical procedures (Lopes et al., 2013).

In predicting future track geometry alterations, it is typical to employ statistical methods to extend historical trends (Ali et al., 2021; Sasidharan et al., 2022; Vale and M. Lurdes, 2013). However, when modifications to the track or traffic conditions are anticipated, relying solely on historical extrapolation may compromise accuracy. This is because past conditions might not always mirror those of the future. Consequently, a more robust approach involves determining future track geometry changes based on first principles, rather than statistical extrapolation. By explicitly modelling the physics of the train-track interaction, this method allows for a comprehensive consideration of potential future changes.

1.2 Aim and Objectives

This thesis aims to develop a better understanding of the railway track deterioration behaviours across various situations. The primary goal of this

thesis is to develop a numerical tool adept at predicting the future track deterioration with both efficiency and accuracy. The purpose of the numerical tool is to provide the practitioners with a framework for investigations, which at the beginning of the PhD activities was not available. To achieve the primary goal of the research, the following specific objectives have been set:

1. To develop a numerical model capable of predicting track irregularity evolution for a wide range of situations, based on the existing 2.5D technique. This model will integrate a novel iterative approach, solved in a hybrid manner, across both time-space and frequency-wavenumber domains.

2. To investigate the influence of subgrade material properties on track deterioration. The numerical model will facilitate the study of how changes in the elastodynamic and settlement properties of the subgrade impact differential track settlement.

3. To compare track deterioration behaviour of both ballasted and slab tracks. Using the numerical model, differential track settlement behaviours for both track types will be scrutinised and compared.

4. To investigate the effects of ballast fouling and moisture of fines on track deterioration. The numerical model will be able to simulate the degraded ballast subjected to both dry and wet conditions.

5. To investigate the impact of rolling stock characteristics on track deterioration. The numerical model will be able to simulate daily rolling stock patterns, accounting for interactions between the different traffic types that operate in the railway infrastructure.

1.3 Outline of the thesis

This thesis is divided into nine chapters. The current chapter includes a brief introduction to the research work and states the aim, the objectives and thesis outline. A summary of the remaining chapters is given below.

Chapter 2 reviews the key literature which covers a wide range of topics related to the work presented in the following chapters. The chapter begins with a brief introduction of railway track structures and mechanisms of its deterioration. This is followed by the assessment of track quality and the methods used for

track geometry maintenance. A review of settlement models including both constitutive and empirical approaches are presented in the same section. Lastly, various approaches in the literature to predict differential settlement are reviewed, encompassing analyses in both the time and frequency domains.

Chapter 3 outlines the features of a differential settlement prediction model as well as an overview of the numerical modelling. It provides a detailed explanation of the 2.5D FEM-PML concept and formulation. Subsequent sections explore train-track interaction, geostatic stress, ballast settlement, subgrade settlement, and the comprehensive solution procedure.

Chapter 4 provides model validation comprising four distinct cases. Validation Case 1 focuses on short-term predictions, while Validation Case 2 investigates track-ground dynamics and non-linearity. Validation Case 3 then explores train-track interaction, and Validation Case 4 examines differential settlement.

Chapter 5 commences with an investigation into the impact of updating the track geometry after each axle load on the differential settlement prediction. Subsequently, it delves into the effect of altering the elastodynamic and settlement properties of the subgrade.

Chapter 6 presents a comparison of settlement behaviour between ballasted and slab tracks. The analysis includes track deflection time histories, early life settlement, settlement after 30MGT of traffic, and deviatoric stresses within track-bed and subgrade layers.

Chapter 7 presents a study of ballast fouling and moisture of fines. This begins with the development of fouled ballast settlement model. Two case studies are analysed: one examining the effect of ballast fouling under dry subgrade conditions and the other considering the impact of moisture on fines within fouled ballast.

Chapter 8 introduces a study of rolling stock characteristics. At the outset of this chapter, an engineering-economic approach is presented. This approach is employed to compute the marginal costs, taking into account the evolution of railway track geometry. Two scenarios are analysed: one involves increasing the linespeed on a passenger line, and the other pertains to amplifying the number of either passenger or freight movements on a line primarily used for passenger traffic. Both an engineering analysis and a marginal tamping cost analysis are detailed.

Chapter 9 summarises the outcomes of this research work and presents the main concluding remarks. Recommendations for future work are also provided. This chapter is followed by a list of references.

Chapter 2
Literature review

2.1 Introduction

Railway tracks undergo plastic settlement when subject to repeated train loading. This occurs differentially along the track rather than in a uniform manner, and the track geometry profile is a key parameter when scheduling track maintenance operations. This chapter aims to conduct a comprehensive review of settlement modelling, while concurrently providing a resource for facilitating further investigations and studies in the field. A brief introduction of railway track structures and mechanisms of its deterioration are presented in sections 2.2 and 2.3. Subsequently, sections 2.4 and 2.5 delve into the assessment of track quality and the methods used for track geometry maintenance. In continuation, section 2.6 presents a review of settlement models including both constitutive and empirical approaches. Finally, in Section 2.7, various approaches in the literature to predicting differential settlement are reviewed, covering analyses in both the time and frequency domains.

2.2 Railway track structures

A railway track structure is comprised of a superstructure on top of a substructure as illustrated in Figure 2.1. The superstructure consists of the rails, fasteners and sleepers or slab. The substructure consists of the ballast, subballast, embankment and subgrade. Typical track structures are divided into two main categories: ballasted and non-ballasted tracks. The adoption of one solution over the other is based on a variety of technical and economic requirements, including initial investment and long-term maintenance. France and Spain adopt a predominant ballasted network. Contrarily, the high-speed railway network in Germany and China is predominantly non-ballasted. This is especially true for lines, which are constructed in the last 20 years (Bastin, 2006). Although the Japanese high speed network now consists of approximately 70% slab track, conventional ballasted track was used for their first line connecting Tokyo and Shin-Osaka in 1964. Comparison between ballasted and non-ballasted high speed lines in Japan shows that the lower maintenance costs associated with the slab track can offset the higher construction costs after 9 years (Miura et al., 1998). Figure 2.2 also shows this, where the four times higher maintenance costs associated with the ballasted

track partially justify the current policy of adopting a slab track solution. Typically slab track systems are considered to be cost-effective if the initial cost is no more than 30% higher than that of ballasted track (Tayabji and Bilow, 2001).

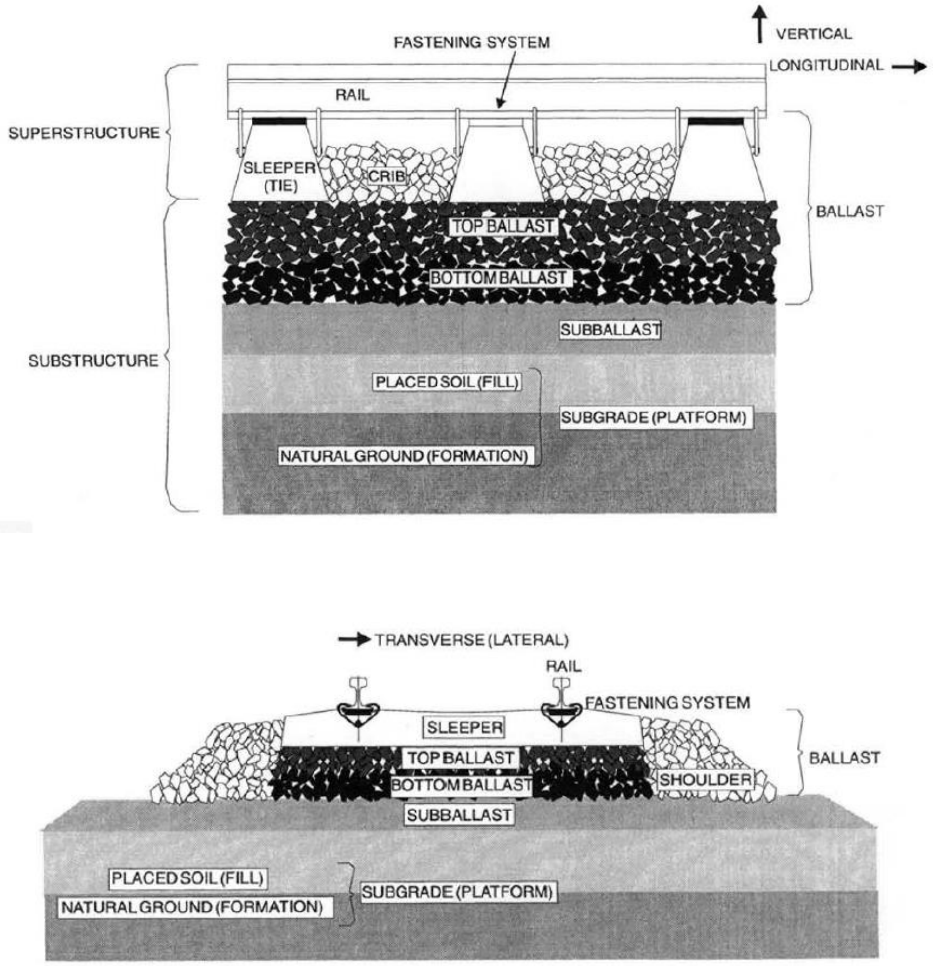

Figure 2.1 Railway track structure components **(Selig and Waters, 1994)**

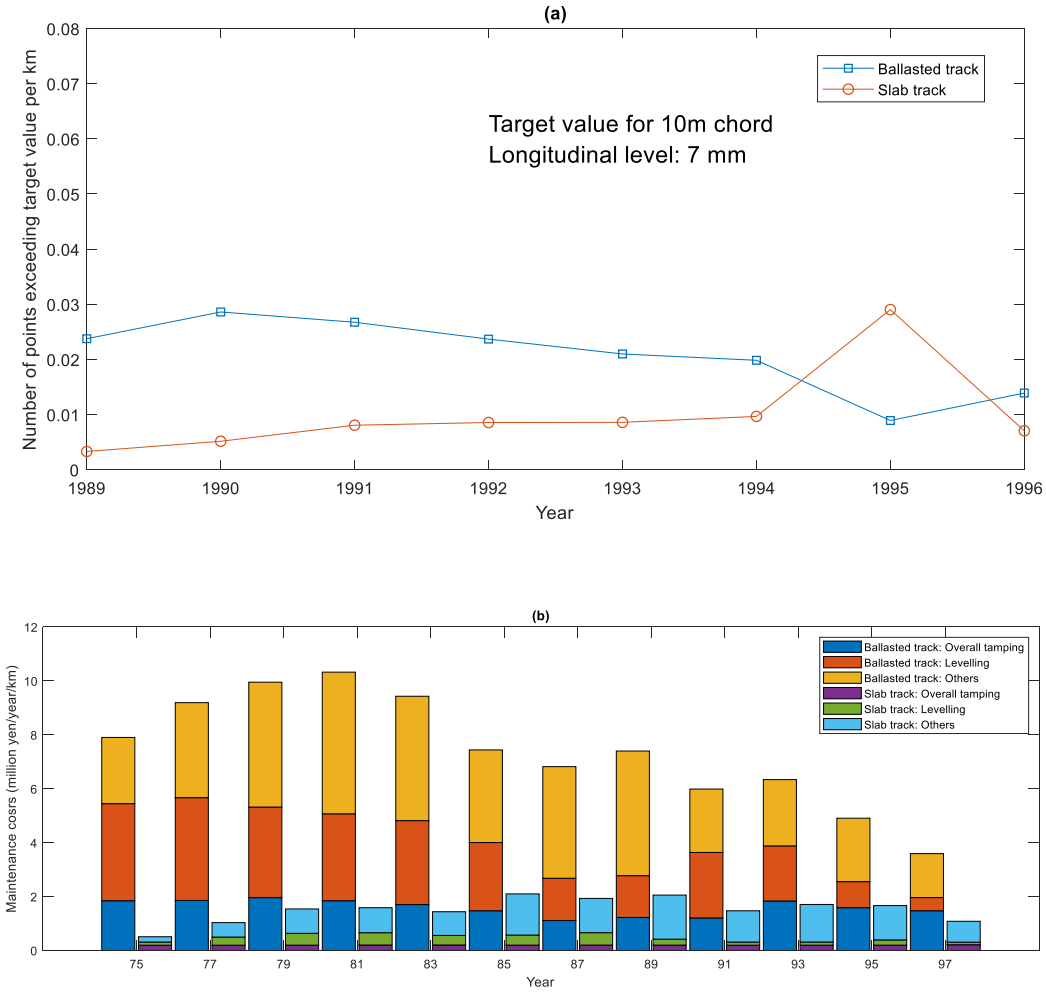

Figure 2.2 Japanese HSR – Sanyo Shinkansen: a) Track irregularities (modified from **(Ando et al., 2001)**); b) Maintenance costs (modified from **(Ando et al., 2001)**)

2.3 Track deterioration

The deterioration of railway tracks is a multifaceted process. The mechanism is influenced by numerous parameters, including axle load, traffic speed, climatic conditions, track characteristics, and topography. Among the physical variables that could potentially influence track deterioration, the decline in track quality is primarily influenced by three parameters: dynamic forces, axle load, and train speed (Ferreira and Murray, 1997). The mechanical processes of track deterioration can be categorised into short-term and long-term mechanisms (Ferreira, 2010). The short-term mechanical process is concerned with the viscoelastic properties and immediate dynamic behaviour of the track. In contrast, the long-term mechanical process involves non-linear plasticity that becomes significant after a substantial number of train passages. This prolonged process results in irreversible track responses and permanent

deformations in the track structure. The deterioration of a railway track resulting from these processes is the phenomenon known as track settlement.

The process of track settlement increment evolves in response to applied loads and the progress of time. Describing the progression of track settlement, a hypothetical scenario is considered wherein an initial track position is assumed, conceptualising an ideal track without any initial defects. Following thousands of train axle passages, the accumulation of non-elastic deformations causes a repositioning of the track. As time progresses and trains continue to traverse the track, modifications in track alignment and elevation introduce irregularities spanning from medium to long wavelengths. Subsequently, these track irregularities trigger low-frequency oscillations in the dynamic loading induced by the moving trains, resulting in permanent and residual deformations within the track. This process occurs randomly along the track, leading to the emergence of differential track settlements. Track geometry can deteriorate rapidly once differential settlement starts to occur, because degradation induces higher train-track dynamic interaction forces, thus leading to further track settlement. In practical applications, the geometric imperfections arising from differential track settlements, coupled with other defects, undergo consistent monitoring in terms of their maximum values and standard deviations.

Consequently, track settlement finds its manifestation in the form of track geometry irregularities. These geometric irregularities are discernible within both the vertical and horizontal planes. Within the vertical plane, irregularities might manifest either in the measured cant (quantified as the vertical disparity between both rails) or in longitudinal levelling, which is the discrepancy between a defect's peak and the recording line within a specific base. Within the horizontal plane, two types of defects can manifest: the track alignment defect, which denotes the lateral deviation of the rail's midpoint from its theoretical position, and the track gauge defect. The gauge is precisely defined as the distance between the inner faces of both rails, measured 14mm below the rolling surface. Finally, track twist, also known as track warping, denotes the vertical discrepancy measured between two rail elevations along a specific rail length (within a 3m base). Figure 2.3 illustrates track longitudinal levelling defect and track alignment defect, recognised as the most significant defects for maintenance considerations in high-speed rail.

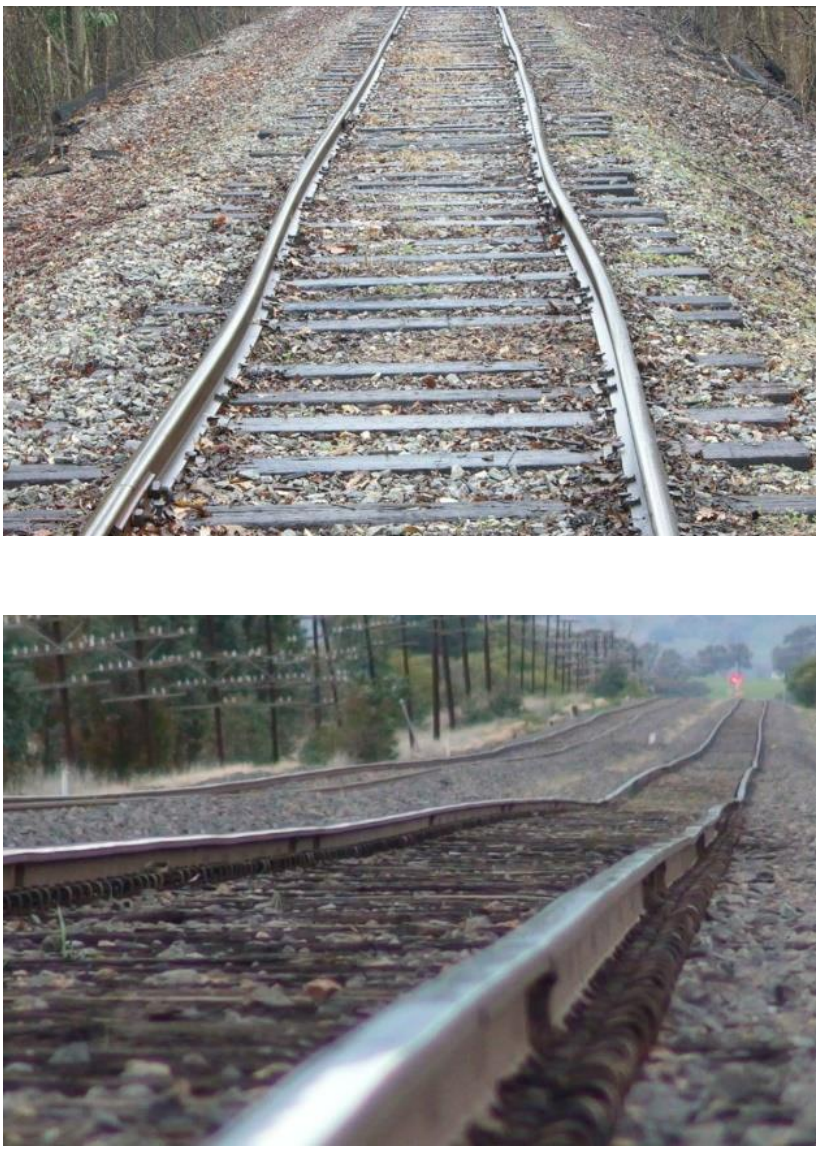

Figure 2.3 Visible geometric defects in a railway track: alignment (above) and longitudinal levelling (below)

Over a long period of service, fine particles originating from multiple sources gather within the ballast, consequently diminishing the performance of the ballast. This phenomenon is commonly referred to as "fouling" and is closely associated with track deterioration. The sources of fouling can be categorised into five distinct groups (Selig and Waters, 1994):

1. Ballast breakdown
2. Infiltration from ballast surface
3. Sleeper wear
4. Infiltration from underlying granular layers
5. Subgrade infiltration

The consequence of ballast fouling is the obstruction of the ballast's capacity to fulfil its designated functions. The impact of ballast fouling varies based on the quantity and size of the fouling. As the mass of smaller sand and fine-gravel-sized fouling particles (0.075 – 19 mm) increases, the ballast's capacity to withstand vertical deformation and maintain void space diminishes. This contributes to the complexity of surface and lining operations and leads to decreased drainage efficiency. As voids progressively fill up, the ballast's density increases, resulting in loosening during tamping. This subsequently leads to a heightened rate of ballast settlement following tamping operations.

A rise in the quantity of fouling particles of clay and silt (with a size smaller than 0.075 mm) also diminishes drainage, subsequently leading to ballast erosion and subgrade attrition. Fine particles can also combine with water, generating an abrasive slurry. Additionally, when the content of clay-sized and silt-sized fouling particles is elevated, it poses challenges for the tamping machine to effectively penetrate and rearranging the ballast.

Table 2.1 provides an overview of ballast fouling indices suggested by different researchers to assess the level of ballast fouling.

Table 2.1 Ballast fouling indices

Fouling index (FI)			**Level of ballast fouling**
$FI = P_{0.075} + P_{4.75}$ (Selig and Waters, 1994)	$FI = P_{0.075} + P_{13.2}$ (Ionescu, 2004)	$FI = D_{90}/D_{10}$ (Ionescu, 2004)	
< 1	< 2	< 2.1 and $P_{13.2} \leq$ 1.5%	Clean
1 to < 10	2 to < 10	2.1 to < 4	Moderately clean
10 to < 20	10 to < 20	4 to < 9.5	Moderately fouled
20 to < 40	20 to < 40	9.5 to < 40	Fouled
≥ 40	≥ 45	≥ 40, $P_{13.2} \geq$ 40%, $P_{0.075}$ > 5%	Highly fouled
P_x = Percentage passing at x mm / 100 D_y = Particle size at y percentage passing (mm)			

In the context of UK practice, ballast is considered to be fully fouled when approximately 30% by weight of particles smaller than 14 mm are present within it. The acceptability of ballast is determined by the following criteria:

1. Ballast is deemed acceptable if it maintains the desired geometry, requiring only routine maintenance activities such as annual or bi-annual tamping or stone blowing.
2. Acceptable ballast exhibits minimal occurrences of wet spots, which refer to track sections with trapped water. Alternatively, any existing wet spots can be attributed to factors other than the ballast.

It is important to note that even if both these criteria are met, the condition of the ballast is considered unacceptable if the proportion of particles smaller than 14 mm within the track exceeds 30%.

2.4 Track quality assessment

In order to establish track quality, the assessment of track geometry parameters is conventionally undertaken at designated intervals. The outcomes are recorded as numerical values, serving as indicators of the track quality level. To obtain these values, rail operators often employ two common measurement methods. In the first method, measurements are conducted manually by personnel who traverse the track to identify potential geometry issues. However, this method is inefficient, especially considering the substantial time and labour costs associated with the extensive railway network. Moreover, the repeatability can vary, as not all rail defects can be discerned directly by the human eye. Advancements in technology have introduced a complementary method wherein specialised inspection cars are employed. The integration of track inspection cars has proven to be effective, resulting in a higher yield of track information data. In the present day, track quality measurement is typically performed using in-service or dedicated trains and a variety of metrics can be used to define a track quality index (TQI) (Yan and Corman, 2020). Figure 2.4 illustrates a track recording car employed by Network Rail (NR) in the UK.

Figure 2.4 Track recording car

Different countries have developed and implemented TQI's in different ways. The European Committee for Standardisation (CEN) has established a set of standards known as EN 13848. The main objective of these standards is to establish a distinctive methodology for assessing the geometric quality of tracks across several member countries. The standard deviation (SD) of track geometric irregularities is applied in the assessment of either longitudinal profile or alignment, involving wavelengths ranging from 3-25m. This metric signifies the scattering of geometry defects (position of measured points along the track) concerning the mean signal (mean track position) within a 200m segment. Increased SD values correlate with poorer track quality, whereas lower SD values signify an improved condition. To ensure operational safety and train service interoperability, the Standard has established three different quality levels: Alert Limit, Intervention Limit, and Immediate Action Limit. The maintenance strategies are linked to these levels. When a value exceeds the Alert Limit, corrective measures must be incorporated into the regular maintenance plan. If a value exceeds the Intervention Limit, immediate corrective action is required before the next inspection. If a value exceeds the Immediate Action Limit, steps should be taken to minimise the risk of derailment (such as line closure, speed reduction, immediate tamping, etc.).

However, the SD of longitudinal profile (vertical track geometry) over a given distance is the most widely used (Neuhold et al., 2020). When the SD of the track geometry reaches a threshold limit value, maintenance action is required. Table 2.2 exhibits the allowable SD threshold values for longitudinal profile.

Table 2.2 SD Threshold values for Longitudinal Profile **(EN 13848-5:2008+A1, 2010)**

Speed (km/h)	Limit value of standard deviation (in mm)
$V \leq 80$	2.3 - 3
$80 < V \leq 120$	1.8 – 2.7
$120 < V \leq 160$	1.4 – 2.4
$160 < V \leq 220$	1.2 – 1.9
$220 < V \leq 300$	1.0 – 1.5

In the UK, NR computes the Standard Deviation (SD) across track sections measuring 1/8 mile, classifying track quality into five bands: Good; Satisfactory; Poor; Very Poor; and Maximum. Table 2.3 shows the maximum allowable values for each quality band, categorised by speed range for 35m wavelength filter.

Table 2.3 Track geometry quality band Standard Deviation values for Longitudinal Profile **(Network Rail, 2015)**

Speed range (mph)	Limit value of standard deviation (in mm)				
	Good	Satisfactory	Poor	Very Poor	Maximum
45 – 60	3.8	5.4	6.3	6.7	>6.7
55 – 60	3.5	5.0	5.9	6.3	>6.3
65 – 70	3.0	4.3	5.4	6.0	>6.0
75 – 80	2.7	3.8	4.8	5.7	>5.7
85 – 95	2.2	3.2	4.0	5.3	>5.3
100 – 110	1.9	2.7	3.4	5.0	>5.0
115 - 125	1.7	2.4	3.0	4.7	>4.7

2.5 Track geometry maintenance

The maintenance of railway tracks can be categorised into two distinct classifications (Shimatake, 1997). The first classification encompasses the remediation of defects in the track geometry arising from the deformation of supporting track layers such as ballast and sleepers. To address this issue, a specific track intervention called tamping is employed, utilising either manual or automatic tamper machines. In the second classification, maintenance activities are undertaken to restore mechanical parameters that often cannot be reinstated without the replacement of components. Typically, on railway lines with moderate traffic loads, the intervention for correcting geometrical parameter defects are undertaken after approximately 40-50 million gross tonnes (MGT), whereas addressing mechanical parameter concerns such as rail unit generally takes place after approximately 500-600MGT (Profillidis, 2000).

Various techniques for intervention, repair, and replacement are employed in track maintenance. However, tamping is a common track maintenance activity. The tamping process is executed by a tamping machine (Figure 2.5), with the objective of correcting geometric faults and compacting the ballast beneath the sleepers.

Figure 2.5 Ballast tamping machine

The operational principle of the tamping machine involves the following procedures (illustrated in Figure 2.6):

A. The tamping machine aligns itself above the sleeper intended for tamping.
B. The lifting rollers elevate the targeted sleeper to the desired level, creating a gap beneath it.
C. The tamping tines penetrate the ballast on both sides of the sleeper.
D. The tamping tines compress ballast into the void below the sleeper, effectively securing the sleeper in its elevated state.
E. The tamping tines are extracted from the ballast, followed by the lowering of the track using the lifting rollers, and then the tamper proceeds to its next location.

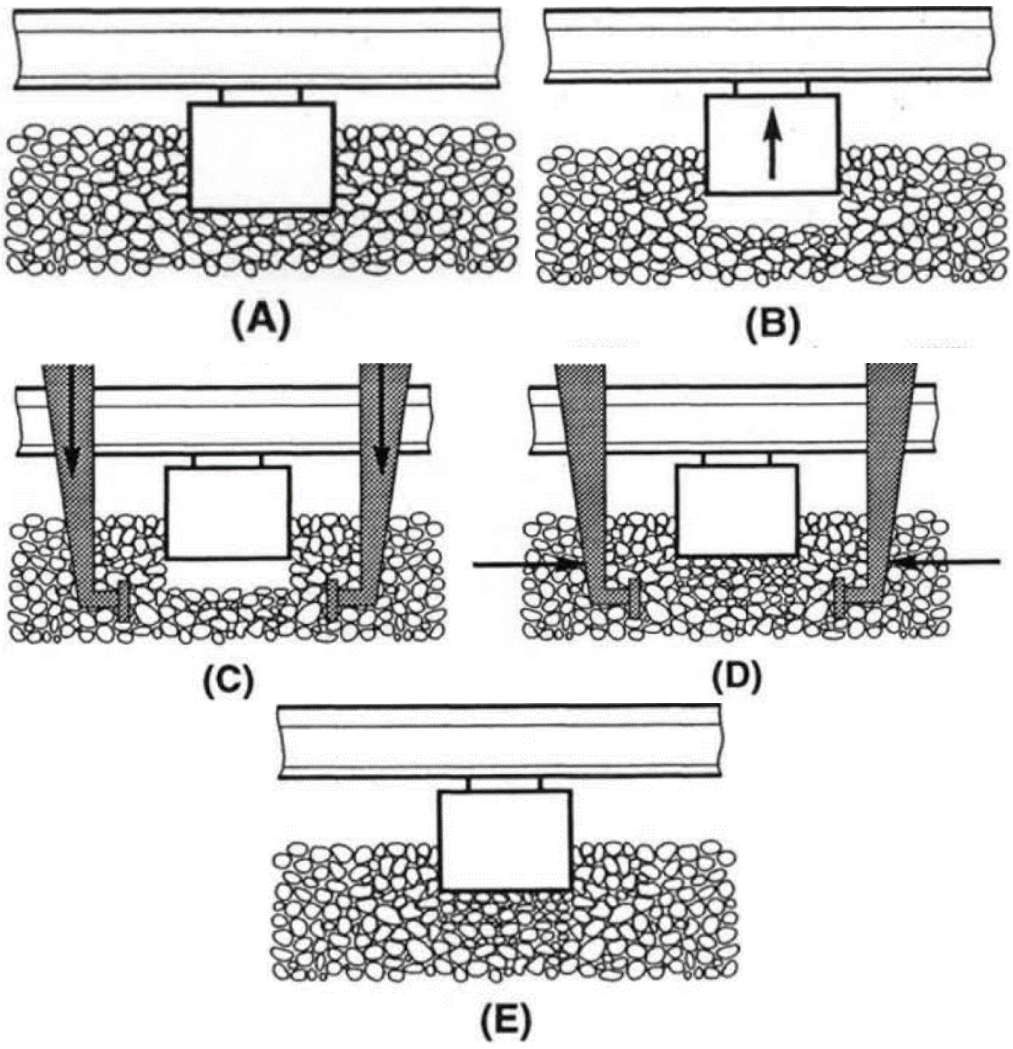

Figure 2.6 Ballast tamping process **(Selig and Waters, 1994)**

Tamping is specifically used to correct vertical track geometry faults for wavelengths within a certain range (for example, between 3-25 m (Esveld, 2001), or 3-35m (Network Rail, 2015)). When the variation in geometry

exceeds a threshold limit, corrective tamping restores it to an acceptable value, thus helping to extend the track life between full track reconstructions. Rather than wait until a SD threshold value is reached and then perform emergency maintenance, common practise is to attempt to predict the future date when maintenance is required. Then it can be planned, resulting in minimal line disruption.

To predict these maintenance schedule dates, most commonly, on existing lines, historical changes in track geometry at a given location are extrapolated into the future to determine degradation (Lee et al., 2020). However, this approach is challenging for cases where significant changes are made to the track or rolling stock. In such situations, historical data is unlikely to be representative of future behaviour. For example:

- New track construction. In this case historical geometry records do not exist.
- The changing of rolling stock characteristics. For example, raising line speed, increased freight-passenger traffic ratios, and deploying new rolling stock. In these cases, the changes in vehicle-track dynamics will lead to different dynamic stress fields in the track. Therefore the settlement rate may be different from the historical one.
- The changing of track characteristics. For example, new track designs, adding new track components, and renewing the track/subgrade. In these cases the dynamic stiffness and strength characteristics of the track may lead to settlement rates that differ from historical ones.

Furthermore, the settlement of railway trackbed is non-linear (Ramos et al., 2020), and changes in TQI are also often non-linear. Thus, to analyse changes in different settlement and TQI requires a numerical model that is capable of simulating daily rolling stock patterns, accounting for interactions between the different traffic types that operate in the railway infrastructure. For example, if a solely passenger line was upgraded to carry multiple freight train movements, the track resulting geometry would likely be different depending upon whether these freight trains were all run consecutively, or interspersed between passenger movements.

2.6 Settlement models

The settlement prediction model comprises two fundamental components: firstly, the computation of the stress/strain response of the structure, and secondly, the determination of the corresponding settlement. In terms of settlement calculation, two common modelling approaches are constitutive and empirical. The constitutive approach typically demands higher computational

effort and involves a significant number of material input properties that are difficult to quantify, thus making real-life application challenging. An alternative modelling approach is to use empirical equations which have fewer input parameters and require minimal computation, yet if used with care, can provide similar accuracy to constitutive models.

2.6.1 Constitutive models

Models based on constitutive relationships attempt to simulate the physical behaviour of materials, using for example, yield criterions, flow rules and hardening rules (Dahlberg, 2001; Indraratna et al., 2012; Suiker and de Borst, 2003). These can be implemented within a finite element model, however the discrete element method (DEM) can also be used to simulate local deformations and heterogeneous particle displacements (Guo et al., 2020; Saussine et al., 2006). Considering the FE approach, an implementation in 3D made in a commercial FE software combining with an elasto-plastic constitutive model was presented by (Shih et al., 2019) to calculate differential settlement in ballasted tracks. A constitutive model integrated with an iterative procedure was developed in (Li et al., 2016) to compute differential track settlement accounting for longitudinal variations in load and track characteristics. However, a challenge with such constitutive models is that they often require input parameters related to the ballast and subgrade that are difficult to measure/quantify. Further, they are often computationally intensive, thus making the prediction of long-term differential settlement due to dynamic train loads challenging (Chen and McDowell, 2016; Shan et al., 2017).

2.6.2 Empirical models

An alternative approach for settlement modelling is to use empirical settlement equations. Several models, see for example (Indraratna and Nimbalkar, 2013; ORE, 1970; Sato, 1995; Shenton, 1985), have been developed for the prediction of ballast settlement under cyclic loading. These typically identify empirical parameters using cyclic triaxial test data, reduced-scale models (Menan Hasnayn et al., 2017; Yu et al., 2019), or in situ measurements. Similarly, empirical parameters for the prediction of subgrade settlement have been obtained by conducting laboratory tests on different soil conditions to investigate plastic deformation under repeated load applications (Li, 1994; Li and Selig, 1996; Liu and Xiao, 2010). Compared with constitutive modelling, the published results achieved using empirical models are similar in accuracy to

constitutive ones, however only depend upon a minimal number of input parameters that are usually relatively straightforward to determine (Ramos et al., 2020).

However, one drawback of the existing empirical models presented in the literature is that they assume the ballast and subgrade materials are subject to cyclic loads of equivalent magnitudes. This is not the case in real life, because track irregularities evolve with each axle passage. Therefore, for each subsequent passage, the train-track dynamic interaction forces, the distribution of stresses within the track layers, and ultimately the induced settlement is different. Further, in real life, most tracks are subject to mixed types of rolling stock (e.g. freight and passenger), running together on a timetable. In such situations, where the simulation of multiple vehicles is required, it is challenging to use the current forms of empirical settlement equations, because the dynamic loads are different for each vehicle.

A key input to constitutive and empirical settlement models are stresses induced in both ballast and subgrade. These stresses are often calculated using a numerical model. One example of using numerical modelling combined with empirical settlement laws is presented by Sayeed and Shahin (Sayeed and Shahin, 2018). Settlement is calculated in both the ballast and subgrade, using a 3D finite element approach to compute the deviatoric stress, considering the effect of a moving dynamic train load. However, the track geometry profile is not updated after subsequent axle passages. Instead, an empirical settlement law is used to extrapolate its change, based upon the results of the initial train passage. This is a drawback because changes in the track geometry influence the train-track interaction forces, which are closely linked to track unevenness (Burrow et al., 2017). Therefore, under certain circumstances, this approach may under-predict the deterioration of track geometry.

2.7 Differential settlement

Deterioration in vertical track geometry results in a cycle of increased train-track dynamic interaction forces and further track deterioration. These track irregularities evolve with each load passage, meaning the characteristics of the train-track dynamic interaction forces, track stress distributions and the settlements also evolve over time. If each track section is subject to relatively constant operational conditions (i.e. no significant changes to rolling stock types, speeds and timetables), and no heavy maintenance/renewal is

performed, then future track geometry changes can be approximated by extrapolating from historical data, with minimal regard for the underlying physics of track degradation (Ali et al., 2021; Bai et al., 2015; Kawaguchi et al., 2005; Sasidharan et al., 2022; Sharma et al., 2018; Vale and M. Lurdes, 2013). This means variables such as changes in train-track interaction and track stress distributions can be ignored. Figure 2.7 shows an example of using an extrapolation method to estimate future track geometry based on historical SD data.

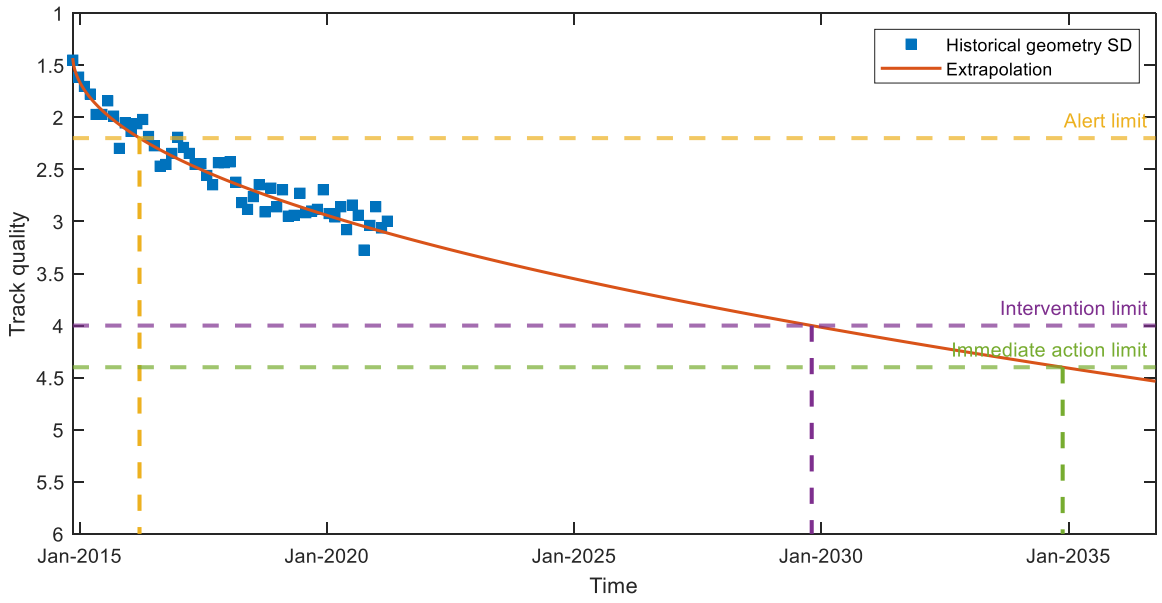

Figure 2.7 Extrapolation approach

Although useful for routine cases, if a railway operator wishes to increase linespeed, or increase the annual number of rolling stock movements (either freight or passenger), maintenance frequency prediction using statistical extrapolation of historical records becomes more difficult because experimental data to perform forecasting analysis is not available. This then introduces uncertainties into marginal cost calculations, and thus the operator's economic appraisal. An important driver behind operational cost is track maintenance frequency. To predict future maintenance intervals requires modelling of operational conditions that are different from the past.

Rather than a statistical approach, this task is well suited to numerical modelling from first principles, where arbitrary future operational conditions can be simulated without relying on past track geometry records. Alternatively, methodologies have been proposed to predict differential track settlement considering train-track dynamic interaction, accounting for the evolution of track

geometry irregularities. For example, Zuada Coelho (Zuada Coelho et al., 2021) introduced a methodology to predict track settlement considering the effect of traffic changes, but at the network scale. The corresponding forces due to the dynamic deformation during train operation are computed, however not every axle passage is considered. Alternatively, Guo and Zhai (Guo and Zhai, 2018) applied an iterative method to estimate the long-term settlement of ballastless track, considering the evolution of differential settlement in the subgrade. An empirical model for subgrade settlement was proposed, combining the deviatoric stress exerted on the surface of the subgrade with an exponential attenuation equation. Further, Nielsen and Li (Nielsen and Li, 2018) proposed a numerical method based on an iterative approach combined with an empirical model to predict the deterioration of track geometry due to differential settlement. The foundation is modelled using a beam-on-elastic-foundation approach (i.e. springs and dampers). Grossoni (Grossoni et al., 2021) presented a semi-analytical approach based on an investigation of material behaviour under cyclic loading combined with a train-track interaction model, that allows for the estimation of differential ballast settlement due to evolving track roughness. Plastic settlement is modelled at each loading cycle as a function of the vertical stress.

A common strategy in the aforementioned approaches is to model the track using springs and dashpots, and then solve in the time domain. Although this provides some advantages, it does not allow for the calculation of 3D dynamic stress fields in the track and the subgrade. Deviatoric stress is one of the most influential parameters on permanent deformation (Indraratna et al., 2010; Li and Selig, 1996) and therefore is closely linked to differential settlement. Comparisons of 2D and 3D modelling have been performed for example by (Arcos et al., 2021; Xu et al., 2015). For railway research applications that require dynamic stress wave simulation (e.g. ground-borne vibration and critical velocity) the calculation of 3D fields is common.

2.8 Conclusion

This chapter has provided a comprehensive review of settlement modelling in railway tracks, emphasising the differential plastic settlement along the track and the significance of the track geometry profile in maintenance operations. The review encompassed various aspects, including the assessment of track quality, methods for track geometry maintenance, and an examination of settlement models, both constitutive and empirical. Furthermore, the discussion highlighted the limitations of existing modelling techniques, particularly in

predicting differential settlement, and emphasised the importance of considering 3D dynamic stress fields in track and subgrade analysis. The influence of deviatoric stress on permanent deformation and the significance of 3D modelling have been highlighted through literature examples (Arcos et al., 2021; Indraratna et al., 2010; Li and Selig, 1996; Xu et al., 2015). For applications requiring dynamic stress wave simulation in railway research, especially in scenarios like ground-borne vibration and critical velocity, the calculation of 3D fields becomes crucial. Overall, this chapter serves as a resource for further investigations and studies in the field of railway track settlement modelling.

Chapter 3
Numerical model review and development

3.1 Characteristics of a differential settlement prediction model

Long-term track geometry changes are important for predicting future maintenance schedules, particularly automated tamping. Therefore any numerical model should be able to predict differential settlement for the wavelength range over which tamping is effective, and the timeline until the next tamping cycle should be scheduled. The forecasting of long-term track settlement is challenging, involving numerous variables such as train-track interaction, an evolving track profile and non-linear soil behaviour. Further, when considering a large number of load passages, small inaccuracies at each iteration are magnified and can greatly affect the final predicted settlement. Thus, for a numerical approach attempting to do this, the following are important to consider:

1. Calculation of 3D stress fields in the track and ground. This is important because deviatoric stress is an influential parameter on settlement (Li and Selig, 1996).
2. Calculation of train-track interaction forces. The dynamic forces caused by the interaction between track geometry irregularities and rolling stock are a key source of differential settlement on plain line. The degradation of track geometry results in higher train-track dynamic interaction forces which affect the distribution of the stresses, and thus further track settlement (Bian et al., 2015).
3. Simulation of changes in track geometry and the evolution of train-track interaction forces. Track geometry degrades after train passages, meaning future train passages are likely to generate different deviatoric stresses and differential settlement, compared to previous trains. This is particularly important when modelling a line with mixed rolling stock (C. Charoenwong et al., 2022).
4. Simulation of the evolution of track-subgrade settlement laws. Track settlement rate is dependent upon the settlements from ballast and subgrade layers induced by previous axle loads. Considering the dynamic forces exerted on the track change, as the track geometry evolves, the settlement relationship should consider changes in track geometry (C Charoenwong et al., 2022).

These characteristics can be achieved using different modelling approaches. For example, a direct approach can be used where non-linear soil behaviour is modelled directly. An alternative method involves an indirect approach, wherein the ground stress fields are estimated through an equivalent linear method. Subsequently, these stress fields can be utilised to calculate settlement using empirical laws. Although the first approach is more exact from the theoretical viewpoint, its application requires significant computational resources and the estimation of many input parameters to accurately define non-linear soil behaviour. Therefore, with the aim of acting as a practical tool for engineering purposes, the second strategy using an equivalent linear method is preferred.

3.2 Numerical modelling overview

A variety of numerical simulation approaches can be used to meet the characteristics mentioned above, however the criteria imply that the problem should be modelled in 3D, consider vehicle dynamics and train-track interaction, and be able to update the track geometry after an arbitrary number of loads with arbitrary magnitude. To achieve these objectives, this paper proposes a novel, 2-step coupled modelling strategy, solved in a hybrid manner, across both time-space and frequency-wavenumber domains. The two primary steps are as shown in Figure 3.1:

Step A: Calculates the 3D elastodynamic response of the track-ground system in the frequency-wavenumber domain. The geo-static stresses and the moving load transfer function that accounts for soil stiffness non-linearity are computed. The 3D stress fields, which include quasi-static and dynamic components, are then calculated in terms of wavenumber and frequency. This part is only computed once for each moving speed of vehicle being considered. Also, the matrices for train and track compliance required for train-track dynamic interaction are computed. These various pre-calculated fields then allow Step B to be computed in an efficient manner for every axle passage.

Step B: Calculates the differential track settlement using a combination of time and frequency domain methods. The train-track dynamic interaction force, the deviator stress and the settlement in the track and ground are calculated. The total deviator stress includes quasi-static stress, dynamic stress and geo-static stress. After every load passage the track irregularity profile is updated and thus the new train-track dynamic force is recalculated. These steps are repeated until the defined number of load cycles or threshold geometry criteria is reached.

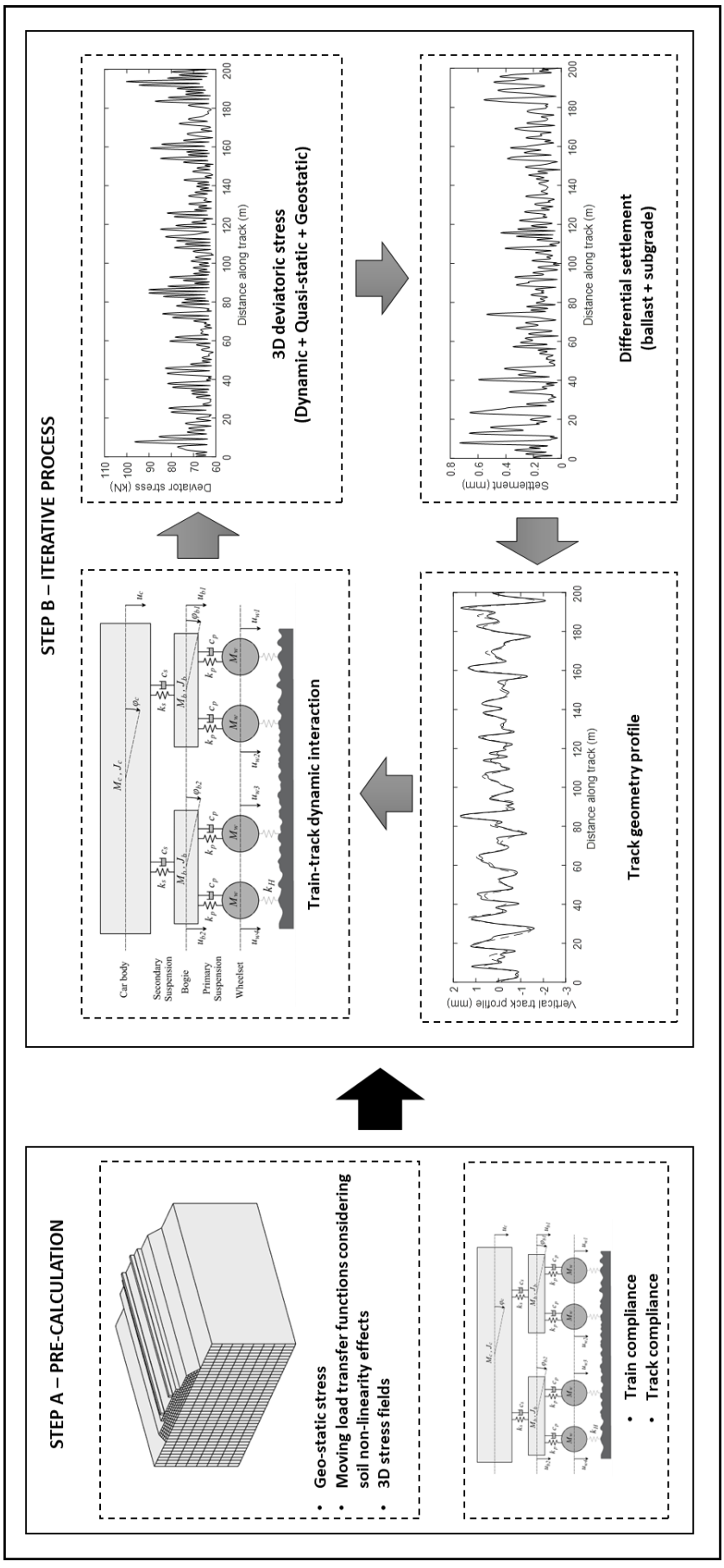

Figure 3.1 Model overview

It is important to acknowledge the limitations of the model, which is constructed based on the 2.5D Finite Element Method (FEM). This method assumes invariant geometry and material properties in one direction, making it suitable for plain line railways where material properties remain constant longitudinally. However, it is worth noting that plain line tracks constitute the majority of railway lines in terms of distance covered.

3.3 Concept and formulation of 2.5D FEM-PML

3.3.1 General formulation

The wavenumber finite element method (aka two-and-a-half dimension approach) is a computationally efficient method for the solution of three-dimensional domains. Two dimensions are solved via finite element theory while the third is solved analytically. It is therefore well-suited for 3D structures that can be approximated as having invariant geometry and material properties in one direction (e.g. railways, highways and tunnels). An example discretisation of the track-ground structure using the developed mesh generator is illustrated in Figure 3.2. This cross-section remains invariable in the longitudinal direction of the track, however the loading is 3D and the track-ground response is calculated in 3D.

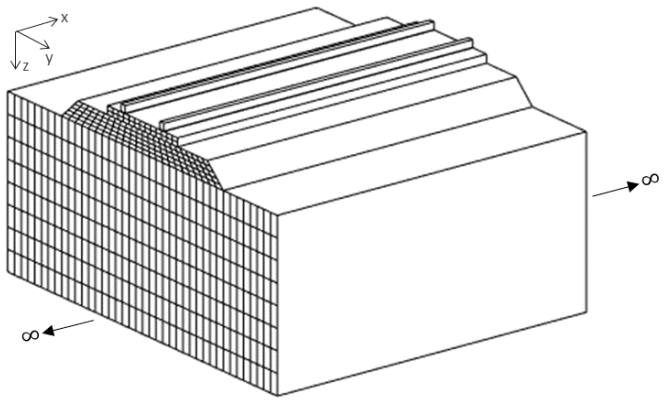

Figure 3.2 Infinite and invariant structure in the train passage (x) direction

Assuming the structure is linear and elastic, the equations of motion can be solved in the wavenumber-frequency domain. A double Fourier transform is

used to transform all variables into the wavenumber-frequency domain in terms of the moving direction of the train (x direction) and time (t).

Following a general finite element formulation (Smith et al., 2013), the following equilibrium equation represents any point in the 3D domain:

$$\int_V \delta\varepsilon\sigma \, dV + \int_V \delta u \rho \frac{\partial^2 u_{\mathrm{i}}(x,t)}{\partial t^2} dV = \int_S \delta u p \, dS \qquad \textbf{(3-1)}$$

where $\delta\varepsilon$ is the virtual strain field; σ is the stress field; δu is the virtual displacement field; u is the displacement field; ρ is the mass density; and p is the applied load.

Eq. (3-1) can be rewritten in terms of nodal variables because the untransformed domain cross-section is discretised into finite elements. Then, considering Parseval's theorem (Hardy and Littlewood, n.d.) , the concept of virtual work is applied to the transform domain. The functions of the Fourier images of x and t are defined as wavenumber and frequency denoted by k_x and ω, respectively. Therefore, in the transformed domain, the virtual work of the internal stresses and inertial forces is:

$$\int_V \delta\varepsilon\sigma \, dV = \int_{k_x} \delta u_n^T(-k_x,\omega) \int_z \int_y B^T(-k_x) D B(k_x) \, dy \, dz u_n(k_x,\omega) \, dk_x \qquad \textbf{(3-2)}$$

$$\int_V \delta u \rho \frac{\partial^2 u(x,t)}{\partial t^2} dV = -\omega^2 \int_{k_x} \delta u_n^T(-k_x,\omega) \int_z \int_y N^T \rho N \, dy \, dz u_n(k_x,\omega) \, dk_x \qquad \textbf{(3-3)}$$

where B is the matrix containing the derivatives of the finite element shape functions; D is the elasticity matrix; N is the shape function matrix; and u_n is the nodal displacement vector in the transformed domain.

Taking advantage of the finite element discretisation on the YZ plane and considering a coordinate 'S' parallel to the edge the element where traction is applied, the virtual work induced by the load is:

$$\int_S \delta u p \, dS = \int_{k_x} \delta u_n^T(-k_x,\omega) \int_s N^T p(k_x,\omega) \, ds \, dk_x = \int_{k_x} \delta u_n^T(-k_x) p_n(k_x,\omega) \, dk_x \qquad \textbf{(3-4)}$$

Then, substituting Eqs. (3-2)-(3-4) into Eq. (3-1), the equilibrium of each finite element in the YZ plane is:

$$\left(\int_z\int_y B^T(-k_x)DB(k_x)\,dy\,dz - \omega^2\int_z\int_y N^T\rho N\,dy\,dz\right)u_n(k_x,\omega) = p_n(k_x,\omega) \tag{3-5}$$

Considering classic finite element notation (Smith et al., 2013), the stiffness $[K]$ and mass $[M]$ matrices are:

$$[K] = \int_z\int_y B^T(-k_x)DB(k_x)\,dy\,dz \tag{3-6}$$

$$[M] = \int_z\int_y N^T\rho N\,dy\,dz \tag{3-7}$$

The matrix $[B]$ is derived from the differential operator matrix $[L]$ and the shape function matrix $[N]$. The longitudinal direction x is transformed into the wavenumber domain, meaning the derivatives in direction x, represented by k_x, are computed analytically. It should be noted that i represents the imaginary unit, which is equal to the square root of negative one.

$$[L] = \begin{bmatrix} ik_x & 0 & 0 & \frac{\partial}{\partial y} & 0 & \frac{\partial}{\partial z} \\ 0 & \frac{\partial}{\partial y} & 0 & ik_x & \frac{\partial}{\partial z} & 0 \\ 0 & 0 & \frac{\partial}{\partial z} & 0 & \frac{\partial}{\partial y} & ik_x \end{bmatrix}^T \tag{3-8}$$

$$[N] = \begin{bmatrix} N_1 & 0 & 0 & \cdots & N_{ne} & 0 & 0 \\ 0 & N_1 & 0 & \cdots & 0 & N_{ne} & 0 \\ 0 & 0 & N_1 & \cdots & 0 & 0 & N_{ne} \end{bmatrix} \tag{3-9}$$

$$[B] = [L][N] \tag{3-10}$$

The 8-node element is used for the model due to its capability to accurately represent the behaviour of complex structures while maintaining computational efficiency. This element consists of eight nodes, each with two degrees of

freedom, as illustrated in Figure 3.3. Like any other model based on the finite element method, variables within each element are integrated using local coordinates. Subsequently, the transformation from the local reference to the global reference is executed. Table 3.1 presents the shape functions, defined within the local frame for the 8-node elements (Alves Costa, 2010).

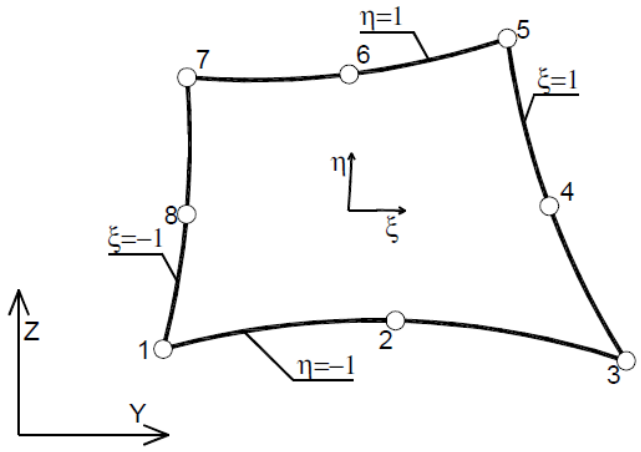

Figure 3.3 8-node element **(Alves Costa, 2010)**

Table 3.1 Shape functions of 8-node elements **(Alves Costa, 2010)**

Shape function	Node i
$\boldsymbol{N_i = \frac{1}{2}(1+\xi\xi_i)(1-\eta^2)}$	i = 4 and 8
$\boldsymbol{N_i = \frac{1}{2}(1+\eta\eta_i)(1-\xi^2)}$	i = 2 and 6
$\boldsymbol{N_i = \frac{1}{4}(1+\xi\xi_i)(1+\eta\eta_i)(\xi\xi_i+\eta\eta_i-1)}$	i = 1, 3, 5 and 7

In terms of damping, a hysteretic damping model is implemented in the frequency domain method via a complex stiffness. The Young's modulus is represented in complex form as $E^* = E(1+iD_h)$, where D_h is the hysteretic damping of the material. The stiffness matrix $[K]$ can be divided into several sub-matrices, independent of the wavenumber (k_x) and frequency (ω) to improve the computation effort. After separating the numerical and analytical derivatives, Eq. (3-5) is defined as:

$$([K_1] + ik_x[K_2] + k_x^2[K_3] - \omega^2[M])\{u_n\} = \{p_n\} \quad \textbf{(3-11)}$$

Assuming the system is symmetrical along its centreline, discretisation can be implemented considering only half of the domain. After solving the global system of equations, the displacements in the transformed domain require a double inverse Fourier transform in order to obtain a solution in the space-time domain.

Considering the displacements as the base variable, the displacement-strain and strain-stress relationships can be established as follows:

$$\{\varepsilon\} = \begin{Bmatrix} \varepsilon_x \\ \varepsilon_y \\ \varepsilon_z \\ \gamma_{xy} \\ \gamma_{yz} \\ \gamma_{xz} \end{Bmatrix} = \begin{Bmatrix} \dfrac{\partial u_x}{\partial x} \\ \dfrac{\partial u_y}{\partial y} \\ \dfrac{\partial u_z}{\partial z} \\ \dfrac{\partial u_x}{\partial y} + \dfrac{\partial u_y}{\partial x} \\ \dfrac{\partial u_y}{\partial z} + \dfrac{\partial u_z}{\partial y} \\ \dfrac{\partial u_x}{\partial z} + \dfrac{\partial u_z}{\partial x} \end{Bmatrix} = [L]\{u\} \quad \textbf{(3-12)}$$

$$\{\sigma\} = [D]\{\varepsilon\} = [D][L]\{u\} \quad \textbf{(3-13)}$$

Where u_x, u_y, u_z are the displacement in the x, y, and z directions, respectively; ε is the strain tensor; ε_x, ε_y, ε_z are the normal strains in the x, y, and z directions, respectively; γ_{xy}, γ_{yz}, γ_{xz} are the shear strains on the xy, yz, and xz planes, respectively; σ is the stress; and D is the material constitutive matrix.

3.3.2 Sleeper elements

The 2.5D method assumes invariant geometry in the direction of train passage (direction x). Although the approximation of discrete sleepers using an equivalent continuous formulation gives acceptable results for the frequency range of study (Knothe and Wu, 1998), to maximise accuracy an anisotropic constitutive material model is used to account for discrepancies in bending stiffness.

To do so, the approach proposed by Alves Costa et al. (Alves Costa et al., 2010) and Karlstrom and Bostrom (Karlström and Boström, 2006) is used. The sleepers are modelled as continuous and orthotropic elements, where the physical properties of the sleepers are used in the cross-section. In the longitudinal plane, the stiffness is set to zero. Therefore, the elasticity matrix $[D]^{-1}_{sleeper}$ used to simulate the sleeper elements is:

$$[D]^{-1}_{sleeper} = \begin{bmatrix} \frac{1}{E_x} & -\frac{\nu_{xk}}{E_k} & -\frac{\nu_{xk}}{E_k} & 0 & 0 & 0 \\ -\frac{\nu_{xk}}{E_x} & \frac{1}{E_x} & -\frac{\nu_{kk}}{E_k} & 0 & 0 & 0 \\ -\frac{\nu_{xk}}{E_x} & -\frac{\nu_{kk}}{E_k} & \frac{1}{E_x} & 0 & 0 & 0 \\ 0 & 0 & 0 & \frac{1}{G_{xk}} & 0 & 0 \\ 0 & 0 & 0 & 0 & \frac{1}{G_{kk}} & 0 \\ 0 & 0 & 0 & 0 & 0 & \frac{1}{G_{xk}} \end{bmatrix} \quad \textbf{(3-14)}$$

$$G_{kk} = \frac{E_k}{2(1+\nu_{kk})} \quad \textbf{(3-15)}$$

where E_k is the Young's modulus of the sleepers in the isotropic YZ plane; ν_{kk} is Poisson's ratio of the sleeper in the isotropic YZ plane; G_{kk} is the shear modulus in the isotropic YZ plane; E_x is Young's modulus of the sleepers in the track direction; ν_{xk} is Poisson's ratio of the sleeper in the track direction; and G_{xk} is the shear modulus in the track direction.

One advantage of this approach is its simplicity. By setting the stiffness to zero in the longitudinal plane, the model becomes less complex and easier to analyse. This simplification can save computational resources and reduce the time required for analysis. In many practical scenarios, the longitudinal stiffness of the sleeper is relatively low compared to its vertical stiffness. This is because the primary function of the sleeper is to provide vertical support to the rails and distribute loads evenly across the ballast. Allowing longitudinal movement of the sleeper reflects its real behaviour under dynamic loading conditions. However, its limitations should be carefully considered when applying this approach in specific analyses.

3.3.3 Rail and rail pad elements

The rails are Euler-Bernoulli beams supported by rail pads which are modelled as springs and dampers continuously connected to the sleeper, as illustrated in Figure 3.4. Since the beam is defined in the longitudinal direction of the track, the system of equations can be analytically computed in the frequency-wavenumber domain without numerical discretisation and integration, using:

$$\left(\left[K_1^{railpad}\right] + k_x^4\left[K_2^{rail}\right] - \omega^2\left[M^{rail}\right]\right)\{u_n\} = \{p_n\} \quad \textbf{(3-16)}$$

$$\left[K_1^{railpad}\right] = \begin{bmatrix} k_p^* & -k_p^* \\ -k_p^* & k_p^* \end{bmatrix} \quad \textbf{(3-17)}$$

$$\left[K_2^{rail}\right] = \begin{bmatrix} EI_r & 0 \\ 0 & 0 \end{bmatrix} \quad \textbf{(3-18)}$$

$$\left[M^{rail}\right] = \begin{bmatrix} m_r & 0 \\ 0 & 0 \end{bmatrix} \quad \textbf{(3-19)}$$

where EI_r is the bending stiffness of the rail; m_r is the mass per unit length of the rail; and k_p^* is the complex stiffness of the rail pad taking rail pad's damping into account. In this case, $k_p^* = k_p + i\omega c_p$, where k_p is the stiffness of the rail pad and c_p is the viscous damping factor of the rail pad; $\{u_n\}$ is the vectors that collect the vertical displacements of the rail and rail pad or sleeper components.

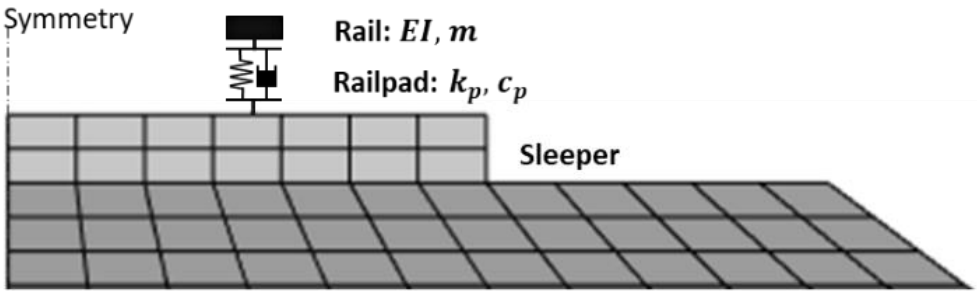

Figure 3.4 Rail-sleeper connection

As the rail is discretely supported by railpads at sleeper spacing, the equivalent continuous railpad stiffness is calculated from its discrete nature using eq. (3-20):

$$K_{continuous} = \frac{K_{discrete}}{Sleeper\ spacing} \quad \textbf{(3-20)}$$

Taking into account the global system of equations, the rail pad stiffness in $\left[K_1^{railpad}\right]$ and the rail mass per unit length in $\left[M^{rail}\right]$ can be assembled with the matrices $[K_1]$ and $[M]$ in Eq. (3-11) respectively. The imaginary part of the matrix $\left[K_1^{railpad}\right]$ is collected in order to form a damping matrix defined as $[C]$. After assembling the element stiffness matrices, the generalised 2.5D finite element equilibrium equation is given by:

$$([K_1] + ik_x[K_2] + k_x^2[K_3] + k_x^4[K_4] + i\omega[C] - \omega^2[M])\{u_n(k_x, \omega)\} = \{p_n(k_x, \omega)\} \quad \textbf{(3-21)}$$

3.3.4 Interfaces between layers

The interactions between different interfaces/layers are modelled accounting for the continuity of displacements and equilibrium of stresses along each subdomain interface (François et al., 2010). Within each layer, the process of coupling nodes requires the replication of nodes in contact, with one belonging to the upper layer and the other to the lower layer. A constraint is established between corresponding nodes. This constraint is enforced on the master node, while the corresponding slave node adheres to the conditions set by the master. This terminology of finite element analysis refers to the method by which contact constraints are practically implemented during the computational process.

To illustrate this concept, Figure 3.5 provides an example of a nodal interface between the upper and lower layers, with the upper layer defined as the slave nodes and the lower layer as the master nodes. Each node is assumed to have three degrees of freedom: X, Y, and Z. Node 1 is assumed to belong to the upper layer, which has positional values X_1, Y_1, and Z_1 located at indices 1 to 3 in the nodal vector. Node 2 belongs to the lower layer and is associated with positional values X_2, Y_2, and Z_2 located at indices 4 to 6 in the nodal vector. The constraints for each node are summarised in Table 3.2.

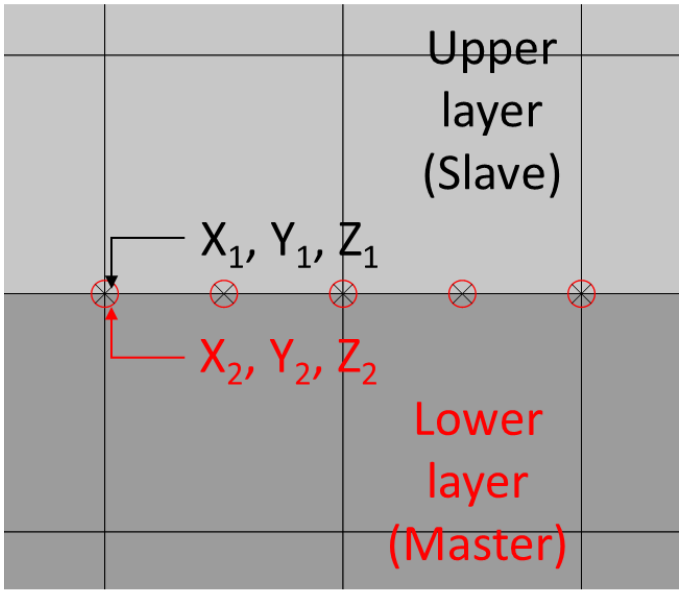

Figure 3.5 Contacts between the upper and lower layers

Table 3.2 Constraints for the interface between nodes 1 and 2

No	Upper layer	Constraint	No	Lower node	Constraint
1	X_1	-1	4	X_2	1
2	Y_1	-1	5	Y_2	1
3	Z_1	-1	6	Z_2	1

Focusing solely on these two nodes, the constraint matrices T1 and t1 are defined as follows:

$$T_1 = \begin{bmatrix} 0 & 0 & 0 & 0 & 0 & 0 \\ 0 & 0 & 0 & 0 & 0 & 0 \\ 0 & 0 & 0 & 0 & 0 & 0 \\ 1 & 0 & 0 & 1 & 0 & 0 \\ 0 & 1 & 0 & 0 & 1 & 0 \\ 0 & 0 & 1 & 0 & 0 & 1 \end{bmatrix} \quad \textbf{(3-22)}$$

$$t_1 = \begin{bmatrix} 1 & 0 & 0 & -1 & 0 & 0 \\ 0 & 1 & 0 & 0 & -1 & 0 \\ 0 & 0 & 1 & 0 & 0 & -1 \\ 0 & 0 & 0 & 0 & 0 & 0 \\ 0 & 0 & 0 & 0 & 0 & 0 \\ 0 & 0 & 0 & 0 & 0 & 0 \end{bmatrix} \quad \textbf{(3-23)}$$

Prior to calculating the corresponding results in finite element analysis, these constraint matrices are incorporated with the stiffness matrix and the applied load vector in the following manner:

$$[T_1][K] + [t_1] \quad \textbf{(3-24)}$$

$$[T_1][p] \quad \textbf{(3-25)}$$

To simulate the unbounded extent of the soil layer, special absorbing layers have been incorporated. These layers serve a crucial function: they actively prevent reflections at the domain boundaries, ensuring more accurate and stable computational results. A comprehensive discussion detailing the mechanics and significance of these absorbing layers is provided in the subsequent section.

3.3.5 Perfectly matched layers

The excitation induced by the passage of the train can be decomposed into two main components: (i) quasi-static load, resulting from the weight of the train; (ii) dynamic load, due to the dynamic interaction between the wheel and the rail. In comparison to the quasi-static load (at speeds below critical velocity), dynamic loading generates propagating waves in the ground and thus high performance absorbing boundaries are needed to prevent domain boundary reflections. Perfectly matched layers consist of layers of elements with identical material properties to the region of the domain they bound. Each sub-layer within the PML domain acts to dampen outgoing waves, and therefore the combined effect of multiple sub-layers is an efficient way to maximise performance. An example setup is shown in Figure 3.6, where the cross section of the 2.5D model is discretised into finite elements and bounded by adding external layers

that are formed by PMLs. The waves impinging the boundary between each domain are described by the 2.5D FEM and the 2.5D PML. It is recommended that the PML mesh is always generated with a thickness of 1 meter and divided into 5 or 6 sub-layers (Lopes et al., 2013). The automatic expansion of the reference domain is achieved by the stretching functions.

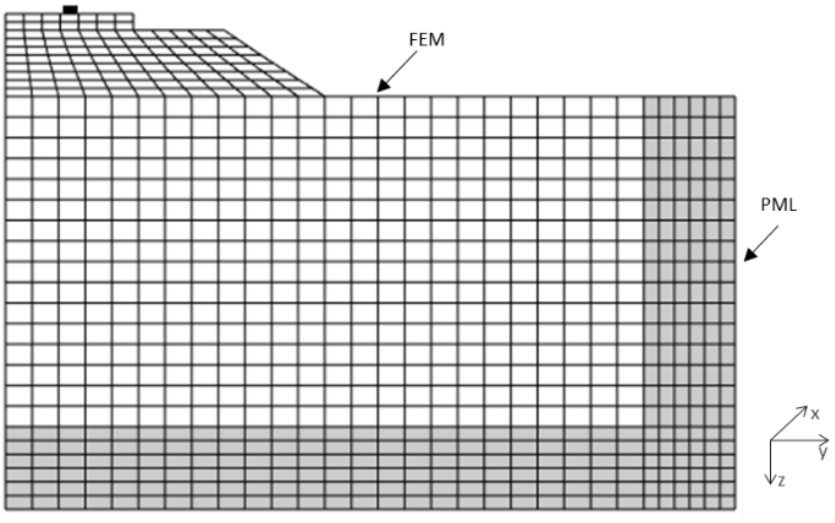

Figure 3.6 Representative half-track model with PML

The x coordinate is transformed to the wavenumber domain, and thus only the coordinates y and z are stretched by the PML in the complex domain. To allow for the absorption of waves inside the PML domain, the same differential equations used in the FEM domain are modified by considering stretched coordinates $\tilde{y}$ and $\tilde{z}$:

$$\tilde{y} = \int_0^y \lambda_y(y)\, dy \qquad \textbf{(3-26)}$$

$$\tilde{z} = \int_0^z \lambda_z(z)\, dz \qquad \textbf{(3-27)}$$

The non-zero complex valued stretching functions in the y direction (λ_y) and in the z direction (λ_z) are defined using functions:

$$\lambda_y(y) = \frac{2\pi}{|k|}\frac{y}{H_y} - i\frac{k_0}{k}\left(\frac{y}{H_y}\right)^2 \quad \textbf{(3-28)}$$

$$\lambda_z(z) = \frac{2\pi}{|k|}\frac{z}{H_z} - i\frac{k_0}{k}\left(\frac{y}{H_z}\right)^2 \quad \textbf{(3-29)}$$

where k_0 is a constant (e.g. Lopes et al. (Lopes et al., 2014) recommend $k_0 = 20$); H_y is the thickness of the PML in the y direction; H_z is the thickness of the PML in z direction; and k is the effective wavenumber for waves propagating along the cross-section, which is given by:

$$k = \sqrt{\left(\frac{\omega}{C_s}\right)^2 - k_x^2} \quad \textbf{(3-30)}$$

where C_s is the velocity of shear wave.

The coordinates y and z in the equilibrium equation are replaced by $\tilde{y}$ and $\tilde{z}$ respectively. The partial derivatives with respect to $\tilde{y}$ and $\tilde{z}$ are expressed using the following relationships:

$$\frac{\partial}{\partial \tilde{y}} = \frac{1}{\lambda_y(y)}\frac{\partial}{\partial y} \quad \textbf{(3-31)}$$

$$\frac{\partial}{\partial \tilde{z}} = \frac{1}{\lambda_z(z)}\frac{\partial}{\partial z} \quad \textbf{(3-32)}$$

Since the solution within the PML domain satisfies the same differential equation as in the 2.5D domain, the stiffness and mass matrices for the PML region can be derived from Eq. (3-6) and Eq. (3-7) respectively. The differential operator $[L^*]$ is given by:

$$[L^*] = \begin{bmatrix} ik_x & 0 & 0 & \frac{1}{\lambda_y(y)}\frac{\partial}{\partial y} & 0 & \frac{1}{\lambda_z(z)}\frac{\partial}{\partial z} \\ 0 & \frac{1}{\lambda_y(y)}\frac{\partial}{\partial y} & 0 & ik_x & \frac{1}{\lambda_z(z)}\frac{\partial}{\partial z} & 0 \\ 0 & 0 & \frac{1}{\lambda_z(z)}\frac{\partial}{\partial z} & 0 & \frac{1}{\lambda_y(y)}\frac{\partial}{\partial y} & ik_x \end{bmatrix}^T \quad \textbf{(3-33)}$$

Due to the frequency dependence of the stretching functions inside the PML domain, the equilibrium condition after assembling the equations of each individual element is:

$$\left(\left[K_{FEM}^{global}(k_x)\right] + \left[K_{PML}^{global}(k_x,\omega)\right] - \omega^2\left(\left[M_{FEM}^{global}\right] + \left[M_{PML}^{global}(k_x,\omega)\right]\right)\right)\{u_n(k_x,\omega)\} = \{p_n(k_x,\omega)\} \quad \textbf{(3-34)}$$

where $\left[K_{FEM}^{global}\right]$ and $\left[K_{PML}^{global}\right]$ are the global stiffness matrices of the FEM and PML domains, respectively, and $\left[M_{FEM}^{global}\right]$ and $\left[M_{PML}^{global}\right]$ are the mass matrices of the FEM and PML domains, respectively.

To demonstrate the wave attenuation inside the PML domain, a simple example taken from (Lopes et al., 2013) was simulated. Figure 3.7 shows the geometry of the 2.5D finite element mesh. It should be highlighted that the PML region can absorb the propagating waves in both directions corresponding to $\lambda_y \neq 1$ $\lambda_z \neq 1$ or in one direction corresponding to $\lambda_y \neq 1$ $\lambda_z = 1$ or $\lambda_y = 1$ $\lambda_z \neq 1$.

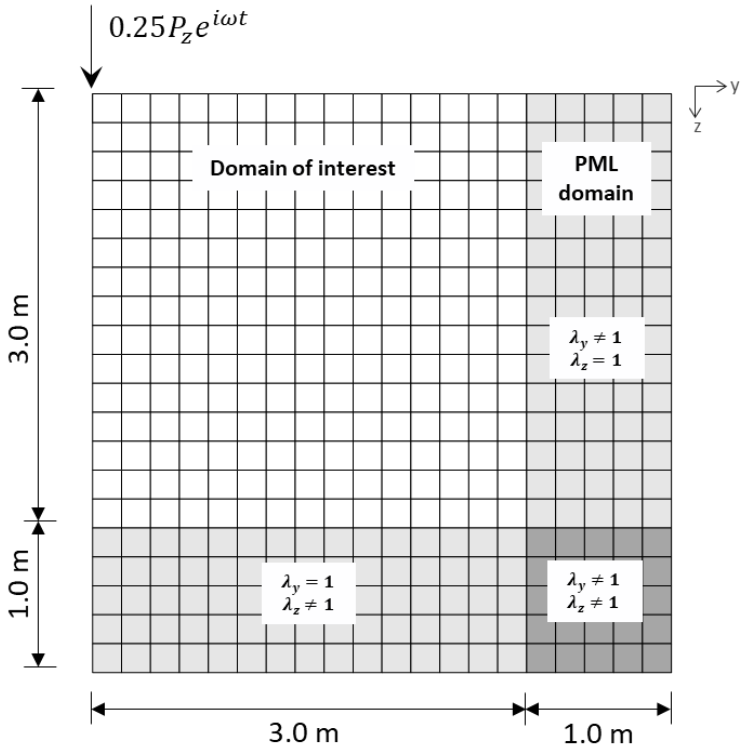

Figure 3.7 2.5D finite element mesh

Figure 3.8 shows the vertical displacements along the y axis monitored at the surface for the dimension less wavenumber $\overline{k_x} = 0.5$ (defined as $\overline{k_x} = k_x C_s/\omega$) and frequency of 75 Hz. The results were compared with the closed-form solution conducted by Tadeu and Kausel (Tadeu and Kausel, 2000). The propagation of waves inside the PML zone (between y = 3-4m) is also demonstrated in Figure 3.8.

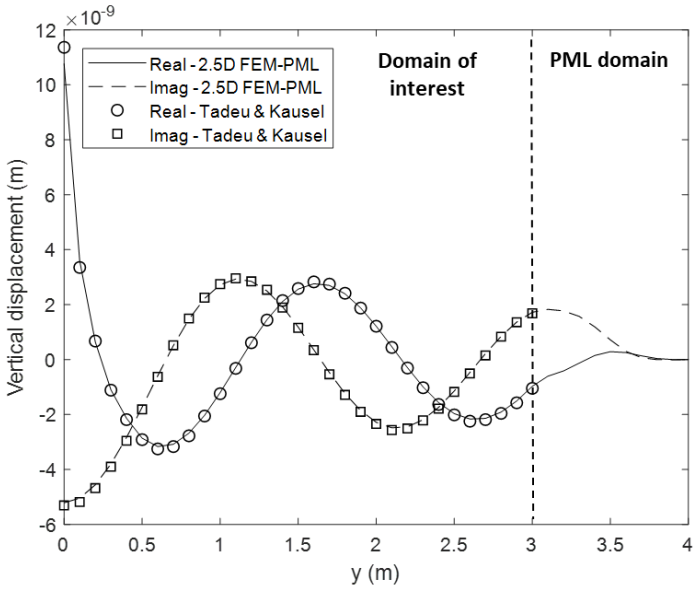

Figure 3.8 Real and imaginary parts of the vertical displacement along y-axis of the full space

Figure 3.9 shows the vertical displacements along the y axis for the following cases:

1. Case (a): Dimensionless wavenumber=0.5,frequency=10Hz
2. Case (b): Dimensionless wavenumber=1.0,frequency=10Hz
3. Case (c): Dimensionless wavenumber=1.5,frequency=10Hz
4. Case (d): Dimensionless wavenumber=0.5,frequency=75Hz
5. Case (e): Dimensionless wavenumber=1.0,frequency=75Hz
6. Case (f): Dimensionless wavenumber=1.5,frequency=75Hz

The wavenumber, k_x can be defined by $\text{Demensionless wavenumber} \times \frac{\omega}{C_s}$, where $\omega = 2\pi \times \text{frequency}$. It is seen that the results are a good match, thus validating the PML implementation.

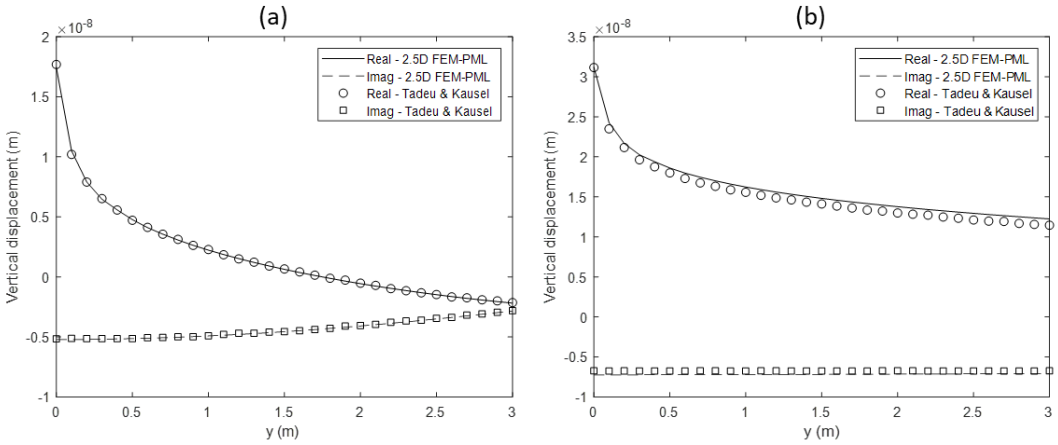

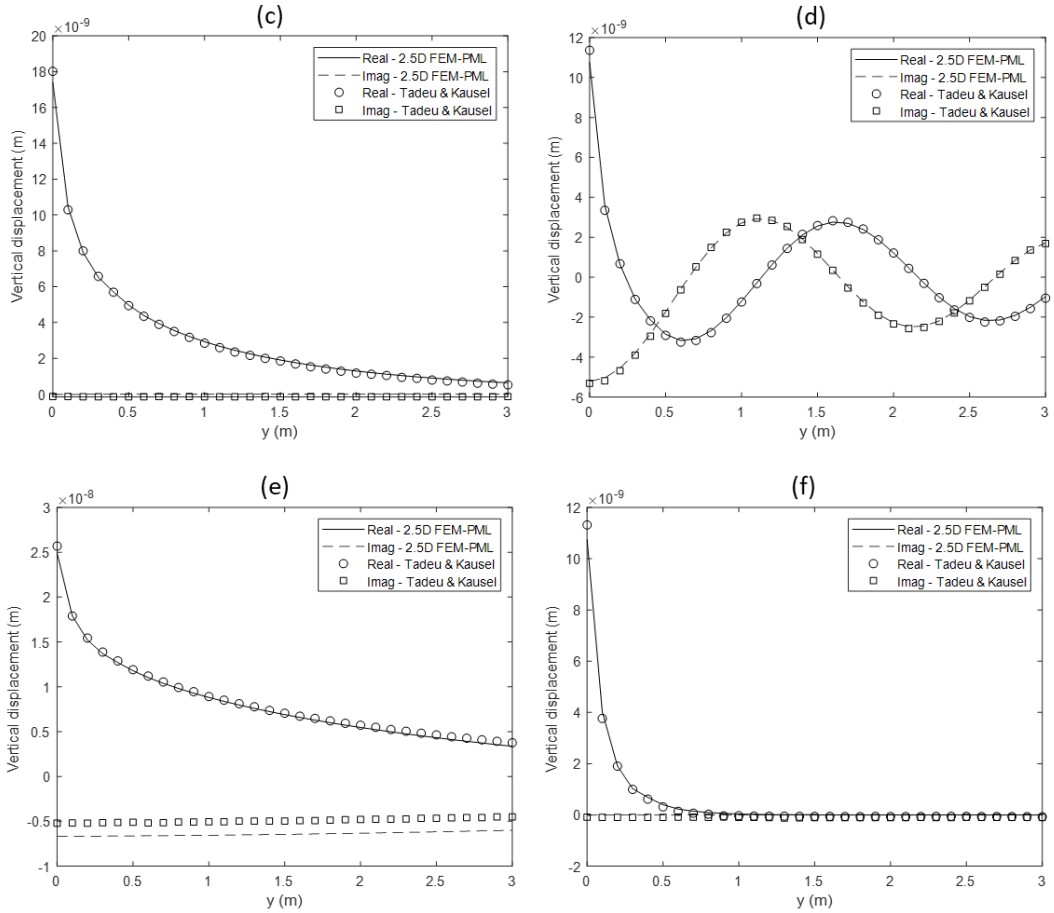

Figure 3.9 Real and imaginary parts of the vertical displacements along y-axis

3.3.6 Soil stiffness non-linearity

When train speed is high and/or axle loads are heavy, large strains can be induced in the soil, and thus the probability of non-linear stiffness behaviour increases (Dong et al., 2019; Shih et al., 2017). This behaviour affects stress wave generation and propagation, and thus settlement, meaning it is important to capture.

The typical stress-strain behaviour of track and ground during cyclic loading can be described by a nonlinear hysteretic loop (Hardin and Drnevich, 1972). This causes the soil stiffness to decrease and the damping ratio to increase as strain increases. To assess non-linear behaviour in the frequency domain while minimising computational demand, an equivalent linear approach is used. The shear modulus reduction curve and the damping ratio are based on an empirical equation proposed by (Ishibashi and Zhang, 1993) which requires cyclic shear strain amplitude (γ_{eff} in this case), mean effective confining pressure and the soil's plasticity index as inputs. Regarding the embankment material, the relationship proposed by (Rollins et al., 2020) is used.

An iterative procedure based on the effective octahedral shear strain is used to update the properties of each element until agreement between the material properties and strain-adjusted properties is achieved. This implementation can be summarised in the following steps:

1. Start calculation assuming low strain properties for all elements
2. Use Eq. (3-35) to compute the effective octahedral shear strain from strain time histories and select the maximum value for each element
3. Use the maximum values of the effective octahedral shear strain with stiffness-strain relationship and damping-strain relationship curves (e.g. Figure 3.10) to compute new equivalent linear values, and update the stiffness and the damping of each element in anticipation of the next iteration. Note that for unbounded soil regions, PML elements are updated using the properties from the closest elements within the intersecting FE domain
4. Repeat steps 2-3 until the differences between both the shear modulus and damping in successive iterations fall below 3% for all elements (Alves Costa et al., 2010)

As the model is used to calculate 3D stress fields, the effective octahedral shear strain is computed as:

$$\gamma_{eff} = \alpha \frac{1}{3} \sqrt{\left(\varepsilon_x - \varepsilon_y\right)^2 + (\varepsilon_x - \varepsilon_z)^2 + \left(\varepsilon_y - \varepsilon_z\right)^2 + 6\left(\gamma_{xy}^2 + \gamma_{xz}^2 + \gamma_{yz}^2\right)} \quad \textbf{(3-35)}$$

where α is 0.65 (as typically used in seismic analysis). The non-linear calculation procedure is performed during Step A and the strain-adjusted material properties are passed to Step B for settlement calculation.

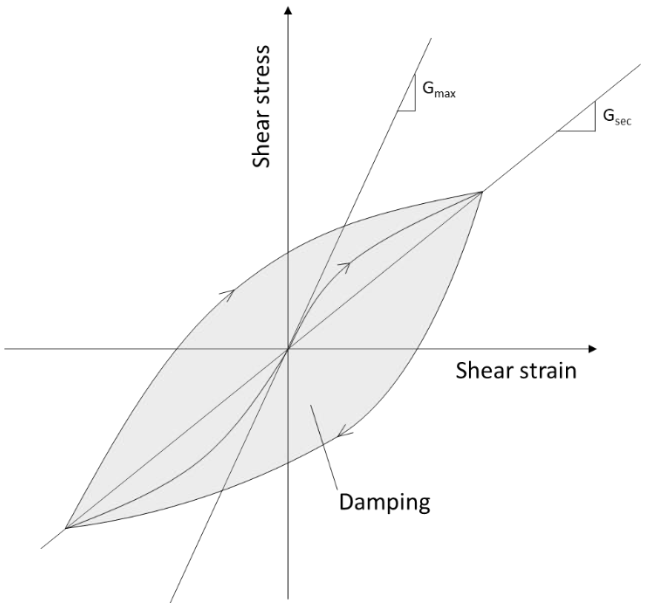

Figure 3.10 Strain-strain path during cyclic loading

3.3.7 Poroelasticity

In modelling the dynamic responses of a saturated porous medium, Biot (Biot, 1962) was the first to introduce a theory outlining three types of coupling (viscous, inertial, and mechanical) between the porous solid skeleton and the pore fluid. Fundamental to Biot's theory are two variables: the displacement of the solid skeleton (u) and the average displacement of the pore fluid relative to that skeleton (w).

When taking into account the $u - w$ formulation and implementing a wavenumber expansion in the x-direction, the 2.5FEM equations in the wavenumber-frequency domain can be articulated as:

$$([K_s] - [M_{B1}])\{u_n(k_x, \omega)\} + ([L_B] - [M_{B2}])\{w_n(k_x, \omega)\} = \{p_s(k_x, \omega)\} \quad \textbf{(3-36)}$$

$$([K_{B1}] - [H_{B1}])\{u_n(k_x, \omega)\} + ([H_{B2}] + [L_B])\{w_n(k_x, \omega)\} = \{p_f(k_x, \omega)\} \quad \textbf{(3-37)}$$

in which K_s, K_{B1} and L_B are stiffness matrices; M_{B1}, M_{B2}, H_{B1} and H_{B2} are mass matrices; u and w are vectors of the solid displacement and the displacement of the pore fluid, respectively at nodal positions; and p_s and p_f are equivalent nodal load vectors. Their detailed expressions are as follows:

$$K_s = ([K_1] + [K_{B1}]) + ik_x[K_2] + k_x^2[K_3] + k_x^4[K_4] + i\omega[C] \tag{3-38}$$

$$[K_{B1}] = \frac{K_f(1-n)}{n}\int_z\int_y B^T(-k_x)mm^TB(k_x)\,\mathrm{d}y\,\mathrm{d}z \tag{3-39}$$

$$[M_{B1}] = \omega^2\rho_s(1-n)\int_z\int_y N^TN\,\mathrm{d}y\,\mathrm{d}z \tag{3-40}$$

$$[L_B] = K_f\int_z\int_y B^T(-k_x)mm^TB(k_x)\,\mathrm{d}y\,\mathrm{d}z \tag{3-41}$$

$$[M_{B2}] = \omega^2\rho_f n\int_z\int_y N^TN\,\mathrm{d}y\,\mathrm{d}z \tag{3-42}$$

$$[H_{B1}] = \frac{i\omega\rho_f gn}{k_D}\int_z\int_y N^TN\,\mathrm{d}y\,\mathrm{d}z \tag{3-43}$$

$$[H_{B2}] = \left(\frac{i\omega\rho_f gn}{k_D} - \omega^2\rho_f\right)\int_z\int_y N^TN\,\mathrm{d}y\,\mathrm{d}z \tag{3-44}$$

$$m = \begin{bmatrix}1\\1\\1\\0\\0\\0\end{bmatrix} \tag{3-45}$$

where is K_f the bulk modulus of pore fluid; n is the porosity of the porous medium; k_D is the permeability of the porous medium; ρ_s is the density of the solid skeleton; and ρ_f is the density of the pore fluid.

By assembling Eqs. (3-36) and (3-37), the following governing equations can be derived:

$$KU = R \tag{3-46}$$

in which

$$K = \begin{bmatrix} K_s - M_{B1} & L_B - M_{B2} \\ K_{B1} - H_{B1} & H_{B2} + L_B \end{bmatrix} \quad \textbf{(3-47)}$$

$$U = \begin{bmatrix} u_n \\ w_n \end{bmatrix} \quad \textbf{(3-48)}$$

$$R = \begin{bmatrix} p_s \\ p_f \end{bmatrix} \quad \textbf{(3-49)}$$

3.4 Train-track interaction

Accurately simulating vehicle dynamics and train-track interaction is vital for differential settlement prediction. This is because it is the interaction between wheel and rail that induces differing dynamic forces along the track, that create track-ground stresses, which in turn govern settlement. To simulate railway vehicle dynamics, a variety of vehicle modelling approaches, each with different levels of complexity have been proposed in the literature (Zhai, 2020), often with the goal of minimising computational requirements for their application. This goal is particularly relevant when simulating large numbers of axle passages for the purpose of differential settlement analysis. Therefore to investigate the validity of simplifying rolling stock models for the purpose of settlement calculations, a variety of common simplifications are compared. Three approaches for passenger vehicle modelling are analysed, followed by two approaches for freight. Their dynamic responses are compared because this is dominant in differential track settlement.

3.4.1 Vehicle model

To simulate the interaction between the vehicle and the track, vehicle-track interaction is solved using a compliance procedure formulated in a moving frame of reference, subject to a moving train (Colaço et al., 2016; Costa et al., 2012). As vertical differential settlement is the parameter under investigation, only vertical dynamics are considered. The equilibrium equations for the vehicle and the track are formulated separately. Then the interaction forces between these two structural systems are calculated respecting equilibrium conditions and displacement compatibility at the connecting points. Assuming perfect contact between train and track, any temporal instant for all connection points between the wheel and the rail is fulfilled by:

$$u_{c,i} = u_r\left(t = \frac{x-a_i}{v_0}\right) + u_{irr}\left(t + \frac{a_i}{v_0}\right) + \frac{P_{dyn,i}(t)}{k_H} \quad \textbf{(3-50)}$$

where u_r is the vertical displacement of the rail; $u_{c,i}$is the vertical displacement at the contact point i; a_i is the location of the contact point i; v_0 is the moving speed of the vehicle; t is the time; u_{irr} is the vertical track irregularity; $P_{dyn,i}$ is the dynamic interaction load at the contact point i; and k_H is the Hertzian stiffness.

For the vehicle part, the standard techniques for rigid multi-body analysis are applied to the system to obtain the following differential equations governing the system dynamics:

$$m_v\ddot{u}_m(t) + k_H\big(u_m(t) - u_r(t)\big) = 0 \quad \textbf{(3-51)}$$

$$k_H\big(u_r(t) - u_m(t)\big) = -F_{dyn}(t) \quad \textbf{(3-52)}$$

where m_v is the mass of the vehicle; u_m is the vertical displacement of the mass; and F_{dyn} is the dynamic interaction force.

As described the irregularity of track by a harmonic wavelength, Eqs (3-51) and (3-52) can be expressed in term of frequency domain as follows:

$$-\Omega^2 m_v u_m(\Omega) + k_H\big(u_m(\Omega) - u_r(\Omega)\big) = 0 \quad \textbf{(3-53)}$$

$$k_H\big(u_r(\Omega) - u_m(\Omega)\big) = -F_{dyn}(\Omega) \quad \textbf{(3-54)}$$

For the track part, the Green's function of the vertical displacement at the contact point (u_c^G) is created corresponding to the moving speed (v_0) where the radian frequency, $\omega = \Omega - k_x v_0$. Then, the displacements at the contact points can be computed from the Green's function and the load function ($\tilde{P}$) in the transformed domain as follows:

$$u_c(x,\Omega) = \frac{1}{2\pi}\int_{-\infty}^{+\infty} u_c^G(k_x,\omega)\tilde{P}(k_x,\Omega)e^{ik_x x}dk_x \quad \textbf{(3-55)}$$

where the load function ($\tilde{P}$) is given by:

$$\tilde{P}(k_x,\Omega) = e^{-ik_x x}F_{dyn}(\Omega) \quad \textbf{(3-56)}$$

Since the analysis is performed in the frequency domain, Eq. (3-50) can be formed in the frequency domain using the transformation of the unevenness track for that domain. Therefore, the dynamic interaction forces in the frequency domain are:

$$\{F_{dyn}(\Omega)\} = -([V] + [V^H] + [T])^{-1}\{\Delta u(\Omega)\} \quad \textbf{(3-57)}$$

$$\{\Delta u(\Omega)\} = \delta u\{b(\Omega)\} \quad \textbf{(3-58)}$$

$$b(\Omega)_i = e^{i\frac{2\pi}{\lambda}a_i} \quad \textbf{(3-59)}$$

$$T(\Omega) = \frac{1}{2\pi}\int_{-\infty}^{+\infty} u_c^G(k_x,\omega)dk_x \quad \textbf{(3-60)}$$

$$V^H = \frac{1}{k_H} \quad \textbf{(3-61)}$$

$$V(\Omega) = [Z]([K^v] - \Omega^2[M^v])^{-1}[Z]^T \quad \textbf{(3-62)}$$

where Ω is the driving frequency, defined by $\Omega = \frac{2\pi}{\lambda}v_0$; T is the flexibility term of the track compliance; V is the flexibility term of the vehicle compliance; V^H is the contact flexibility matrix; Z is a constant matrix, M^v is the vehicle mass matrix and K^v is the vehicle stiffness.

Three common simplifications for modelling a passenger train are illustrated in Figure 3.11. The first option, as shown in Figure 3.11(a), is a complete vehicle model which takes into account the main structural aspects of the train dynamics. In contrast, Figure 3.11(b) ignores the car box, instead only considering the dynamic motion of the bogies (semi-sprung masses) and the wheelsets (unsprung masses). Further, Figure 3.11(c) only considers the presence of the wheelsets (unsprung masses) for dynamic computation.

Freight vehicles typically contain only one level of suspension, meaning only two modelling options are considered. The first option shown in Figure 3.12(a) is a complete vehicle model with one level of suspension. The simplified option shown in Figure 3.12(b) is where only the bogies and the wheelsets are considered.

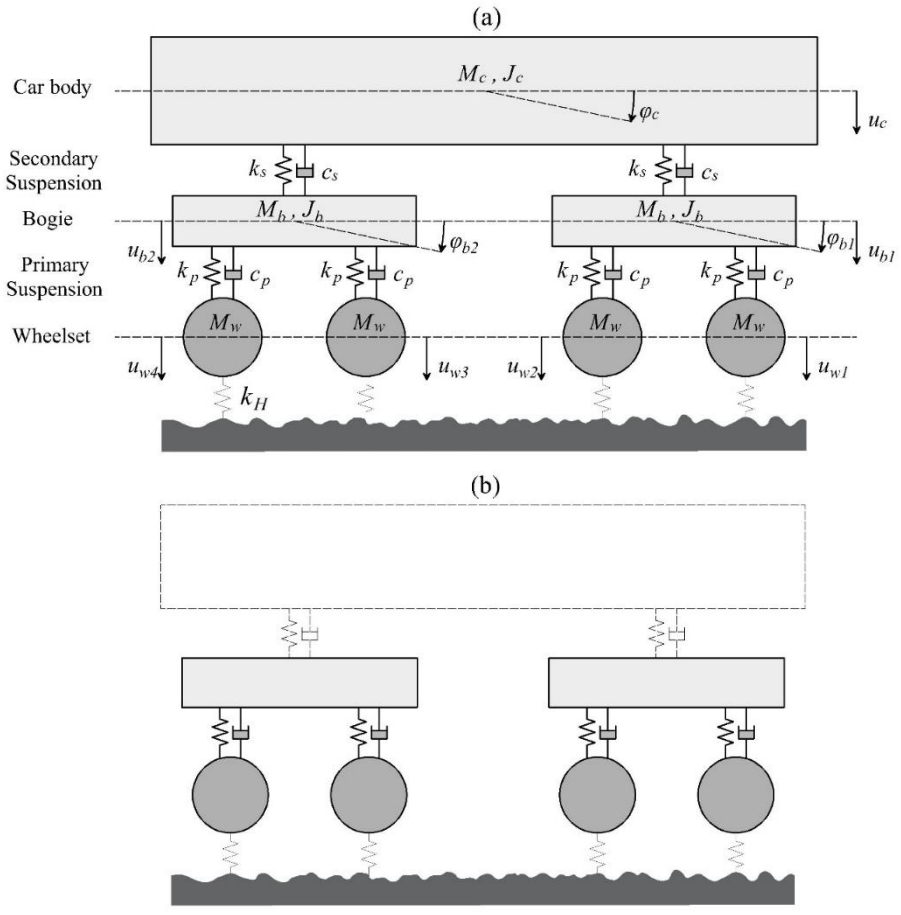

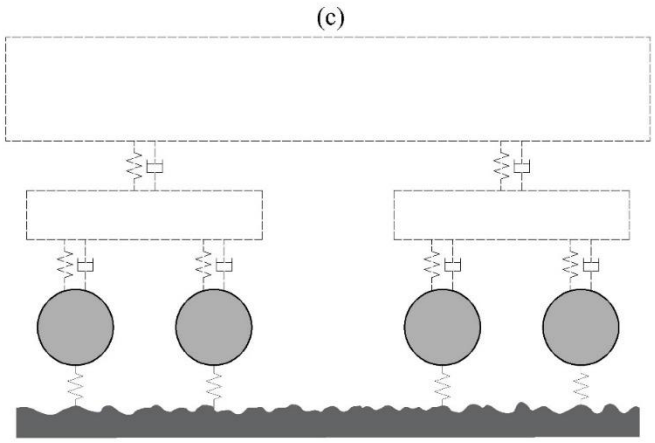

Figure 3.11 Passenger vehicle modelling approaches: (a) complete vehicle model, (b) simplified model containing bogies and wheelsets, (c) simplified model containing only wheelsets

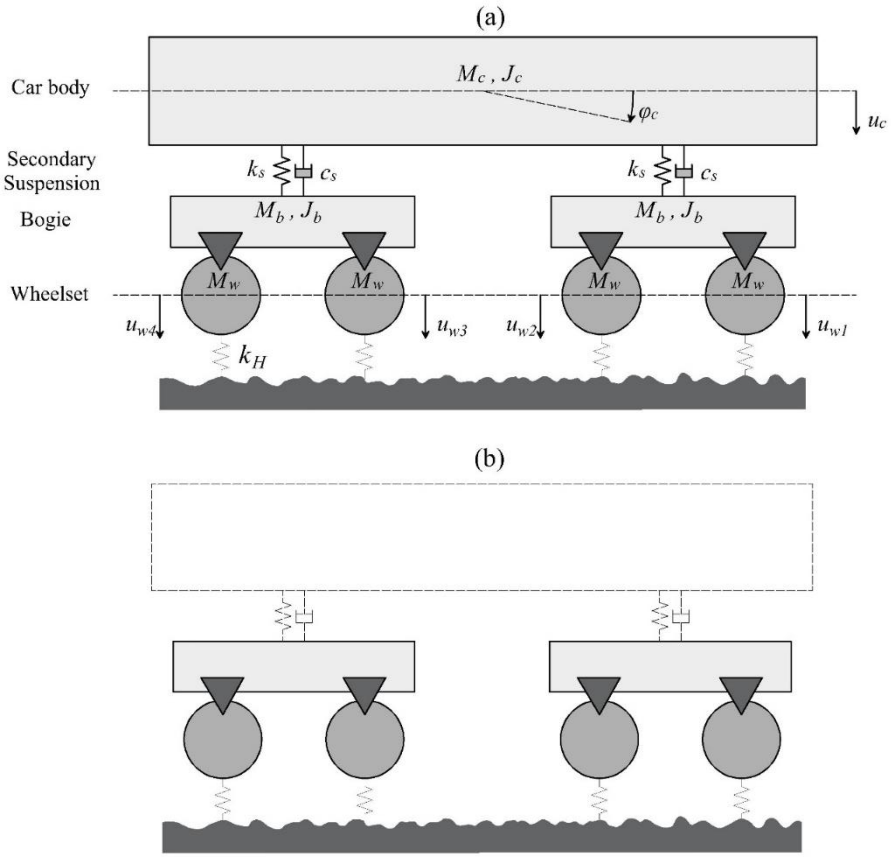

Figure 3.12 Freight vehicle modelling approaches: (a) complete vehicle model, (b) simplified model of bogies and wheelsets

Mass and stiffness matrices of the passenger vehicle which contains primary and secondary suspensions:

$$[Z] = \begin{bmatrix} 0 & 0 & 0 & 0 & 0 & 0 & 1 & 0 & 0 & 0 \\ 0 & 0 & 0 & 0 & 0 & 0 & 0 & 1 & 0 & 0 \\ 0 & 0 & 0 & 0 & 0 & 0 & 0 & 0 & 1 & 0 \\ 0 & 0 & 0 & 0 & 0 & 0 & 0 & 0 & 0 & 1 \end{bmatrix} \quad \textbf{(3-63)}$$

$$[M^v] = \begin{bmatrix} Mc & 0 & 0 & 0 & 0 & 0 & 0 & 0 & 0 & 0 \\ 0 & Jc & 0 & 0 & 0 & 0 & 0 & 0 & 0 & 0 \\ 0 & 0 & Mb & 0 & 0 & 0 & 0 & 0 & 0 & 0 \\ 0 & 0 & 0 & Jb & 0 & 0 & 0 & 0 & 0 & 0 \\ 0 & 0 & 0 & 0 & Mb & 0 & 0 & 0 & 0 & 0 \\ 0 & 0 & 0 & 0 & 0 & Jb & 0 & 0 & 0 & 0 \\ 0 & 0 & 0 & 0 & 0 & 0 & Mw & 0 & 0 & 0 \\ 0 & 0 & 0 & 0 & 0 & 0 & 0 & Mw & 0 & 0 \\ 0 & 0 & 0 & 0 & 0 & 0 & 0 & 0 & Mw & 0 \\ 0 & 0 & 0 & 0 & 0 & 0 & 0 & 0 & 0 & Mw \end{bmatrix} \quad \textbf{(3-64)}$$

$$[K^v] = \begin{bmatrix} 2Ks & 0 & -Ks & 0 & -Ks & 0 & 0 & 0 & 0 & 0 \\ 0 & 2Ks \cdot lb^2 & -Ks \cdot lb & 0 & Ks \cdot lb & 0 & 0 & 0 & 0 & 0 \\ -Ks & -Ks \cdot lb & Ks + 2Kp & 0 & 0 & 0 & -Kp & -Kp & 0 & 0 \\ 0 & 0 & 0 & 2Kp \cdot lw^2 & 0 & 0 & -Kp \cdot lw & Kp \cdot lw & 0 & 0 \\ -Ks & Ks \cdot lb & 0 & 0 & Ks + 2Kp & 0 & 0 & 0 & -Kp & -Kp \\ 0 & 0 & 0 & 0 & 0 & 2Kp \cdot lw^2 & 0 & 0 & -Kp \cdot lw & Kp \cdot lw \\ 0 & 0 & -Kp & -Kp \cdot lw & 0 & 0 & Kp & 0 & 0 & 0 \\ 0 & 0 & -Kp & Kp \cdot lw & 0 & 0 & 0 & Kp & 0 & 0 \\ 0 & 0 & 0 & 0 & -Kp & -Kp \cdot lw & 0 & 0 & Kp & 0 \\ 0 & 0 & 0 & 0 & -Kp & Kp \cdot lw & 0 & 0 & 0 & Kp \end{bmatrix} \quad \textbf{(3-65)}$$

Mass and stiffness matrices of the freight vehicle which contains only one set of suspension:

$$[Z] = \begin{bmatrix} 0 & 0 & 1 & lw & 0 & 0 \\ 0 & 0 & 1 & -lw & 0 & 0 \\ 0 & 0 & 0 & 0 & 1 & lw \\ 0 & 0 & 1 & 0 & 1 & -lw \end{bmatrix} \quad \textbf{(3-66)}$$

$$[M^v] = \begin{bmatrix} Mc & 0 & 0 & 0 & 0 & 0 \\ 0 & Jc & 0 & 0 & 0 & 0 \\ 0 & 0 & Mb + 2Mw & 0 & 0 & 0 \\ 0 & 0 & 0 & Jb + 2Mw \cdot lw^2 & 0 & 0 \\ 0 & 0 & 0 & 0 & Mb + 2Mw & 0 \\ 0 & 0 & 0 & 0 & 0 & Jb + 2Mw \cdot lw^2 \end{bmatrix} \quad \textbf{(3-67)}$$

$$[K^v] = \begin{bmatrix} 2Ks & 0 & -Ks & 0 & -Ks & 0 \\ 0 & 2Ks \cdot lb^2 & -Ks \cdot lb & 0 & Ks \cdot lb & 0 \\ -Ks & -Ks \cdot lb & Ks & 0 & 0 & 0 \\ 0 & 0 & 0 & 0 & 0 & 0 \\ -Ks & Ks \cdot lb & 0 & 0 & Ks & 0 \\ 0 & 0 & 0 & 0 & 0 & 0 \end{bmatrix} \quad \textbf{(3-68)}$$

where Mc is mass of the car box; Mb is mass of the bogie; Mw is mass of the wheelset; Jb is the rotational inertia of the car body; Kp is the complex stiffness of the primary suspension; Ks is the complex stiffness of the secondary suspension; lb is half the distance between the bogie's centre of gravity; and lw is half the wheelbase that shares the same bogie. Kp and Ks are defined as:

$$Kp = k_{pri} + i\omega c_{pri} \quad \textbf{(3-69)}$$

$$Ks = k_{sec} + i\omega c_{sec} \quad \textbf{(3-70)}$$

where k_{pri} is the spring stiffness of the primary suspension; k_{sec} is the spring stiffness of the secondary suspension; c_{pri} is the viscous damping of the primary suspension; and k_{sec} is the viscous damping of the secondary suspension.

In a more complex application, the response in terms of displacements or any other magnitude results from the superimposition of effects of dynamic actions. These are induced by the different harmonics needed to represent the track irregularities, added to the quasi-static excitation, whose interaction forces are known in advance. This overlap of effects is carried out in a particularly interesting manner, taking into account the linearity of the system and the concept of Green's function. This can be expressed as follows:

$$u(x - v_0 t, y, z, t) = \sum_{j=1}^{N} \frac{1}{2\pi} \int_{-\infty}^{+\infty} u_j^G \left(k_x, y, z, \Omega_j - k_x v_0\right) \tilde{P}_j(k_x, \Omega_j) e^{ik_x(x - v_0 t)} dk_x e^{i\Omega_j t} \quad \textbf{(3-71)}$$

where $u(x - v_0 t, y, z, t)$ is the displacement in a generic direction of any point in the domain; and $u_j^G\left(k_x, y, z, \Omega_j - k_x v_0\right)$ is the Green's function in the semi-transformed domain of the displacement in the direction considered relative to the vertical load that moves with speed v_0 along the rail and with oscillation frequency Ω_j. In a quasi-static excitation scenario, it is logical to consider $\Omega = 0$. The load function $\tilde{P}(k_x, \Omega = 0)$ derived based on prior understanding of the respective action. In this case, it corresponds to the inherent weight of the oscillator or, in a more realistic situation, to the distribution of the vehicle's weight across different axles.

A simplified 2D model based on beam on elastic foundation theory (Lamprea-Pineda et al., 2022) is used to calculate the response due to train-track dynamic interaction. An infinite Euler-Bernoulli beam is used to represent the rail which is supported by a single continuous elastic layer. It has the following material properties (single rail): Young's modulus $E = 2.1 \times 10^{11}\ N/m^2$; second moment of area $I = 30.55 \times 10^{-6}\ m^4$; cross section area $A = 0.00763\ m^2$; density $\rho = 7850\ kg/m^3$; and support stiffness $s = 100 \times 10^6\ N/m^2$. An artificial track irregularity profile for wavelengths in the range $3 < \lambda \leq 35\ m$ is generated using the PSD (Power Spectral Density) function defined by FRA (Federal Railroad Administration, 1980) but the constants is modified to generate specific SD

profiles at higher speeds (>177km/h). The properties of passenger and freight vehicles are summarised in Table 3.3, where the properties of passenger vehicle are taken from (Kouroussis et al., 2014) and freight vehicle adapted from (Sheng, 2001). The speeds of passenger and freight vehicles are 200 and 97km/h respectively.

Table 3.3 Parameters of passenger and freight vehicles

Parameter	Passenger	Freight
Number of cars	11	40
Number of axles	44	160
Axle spacing (m)	2.9	1.7
Bogie spacing (m)	19	9.7
Car body mass (kg)	$329x10^2$	$864 x10^2$
Car body pitching moment of inertia ($kg.m^2$)	$208x10^4$	$102x10^4$
Bogie mass (kg)	4932	2800
Wheelset mass (kg)	1538	2000
Bogie pitching moment of inertia ($kg.m^2$)	5150	2020
Primary suspension stiffness (kNm^{-1})	3420	-
Primary suspension viscous damping (Nsm^{-1})	$360 x10^2$	-
Secondary suspension stiffness (kNm^{-1})	1320	2660
Secondary suspension viscous damping (Nsm^{-1})	$360x10^2$	$25x10^2$

Figure 3.13 compares the peak displacements due to dynamic loading along the track length, for the complete vehicle and simplified vehicle models. As shown in Figure 3.13(a), the displacements due to the different vehicle assumptions show significant differences, however are in a similar range in terms of magnitude. In contrast, the freight vehicle shows a large discrepancy in magnitude, comparing the full and simplified vehicles - Figure 3.13(b). This large difference is justified by the higher stiffness of the primary suspension and suspensions. Considering the errors associated with using simplified passenger and freight vehicles, for the purpose of differential settlement modelling, this shows it is important to use full vehicle models (i.e. avoid reducing the number of degrees of freedom).

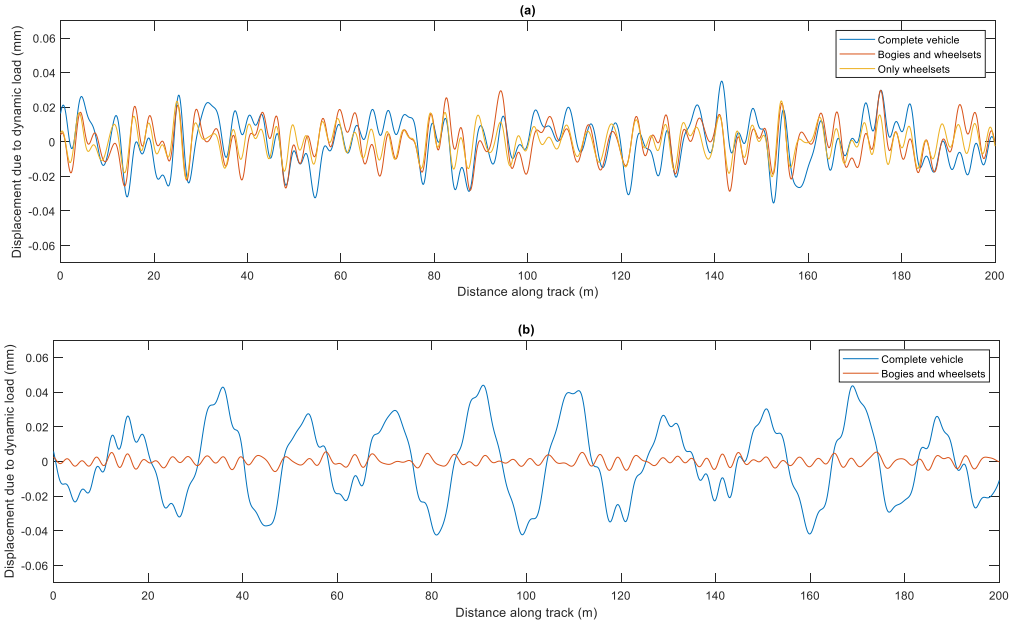

Figure 3.13 Maximum rail deflection along track (dynamic excitation only): (a) passenger vehicle models (b) freight vehicle models

It is shown that the dynamic train-track response and track settlements are most accurately replicated when full-car rolling-stock models are simulated. However, as common with many high speed rolling stock, the ICE trainset is comprised of cars with 3 differing sets of properties (Figure 3.14). To simplify the trainset the 'side' car properties are changed to be equal to the 'central' cars, due to their high similarity (Kouroussis et al., 2014).

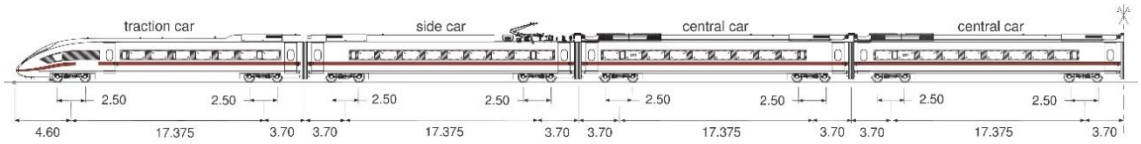

Figure 3.14 ICE train wheelset layout dimensions (adapted from **(Kouroussis et al., 2014)**)

Figure 3.15 shows the relationship between the track response due to both central and traction cars. An artificial track irregularity profile for wavelengths in the range $3 < \lambda \leq 25$ m is generated using the PSD (Power Spectral Density) function defined by FRA but the constants is modified to generate specific SD profiles at speed of 200km/h. The properties of vehicles are based upon the ICE (Kouroussis et al., 2014) as shown in Table 3.4.

Table 3.4 ICE vehicle parameters

Parameter	Symbol	Traction cars	Side and central cars
Axle spacing (m)	-	2.5	2.5
Bogie spacing (m)	-	17.375	17.375
Car body mass (kg)	M_c	50000	35000
Car body pitching moment of inertia (kg.m^2)	J_c	1.03x10^6	2.16x10^3
Bogie mass (kg)	M_b	2840	5154
Wheelset mass (kg)	M_w	1600	1750
Bogie pitching moment of inertia (kg.m^2)	J_b	3.22x10^3	2.46x10^3
Primary suspension stiffness (Nm^{-1})	k_p	4.30x10^6	1.40x10^6
Primary suspension viscous damping (Nsm^{-1})	c_p	24x10^3	120x10^3
Secondary suspension stiffness (Nm^{-1})	k_s	1.43x10^6	0.45x10^6
Secondary suspension viscous damping (Nsm^{-1})	c_s	70x10^3	40x10^3

Figure 3.15(a) shows track displacements due to dynamic excitation between a traction car and a central car. The central car model results in a higher dynamic response, however the traction car model results in higher overall displacement (considering both quasi-static and dynamic loads) as shown in Figure 3.15(b). Therefore, both traction and side/central models are taken into account in the 2.5D train-track interaction and settlement simulation. This is done by running the model in the order of train cars: Traction*2; Central*6; Traction*2; Central*6…etc.

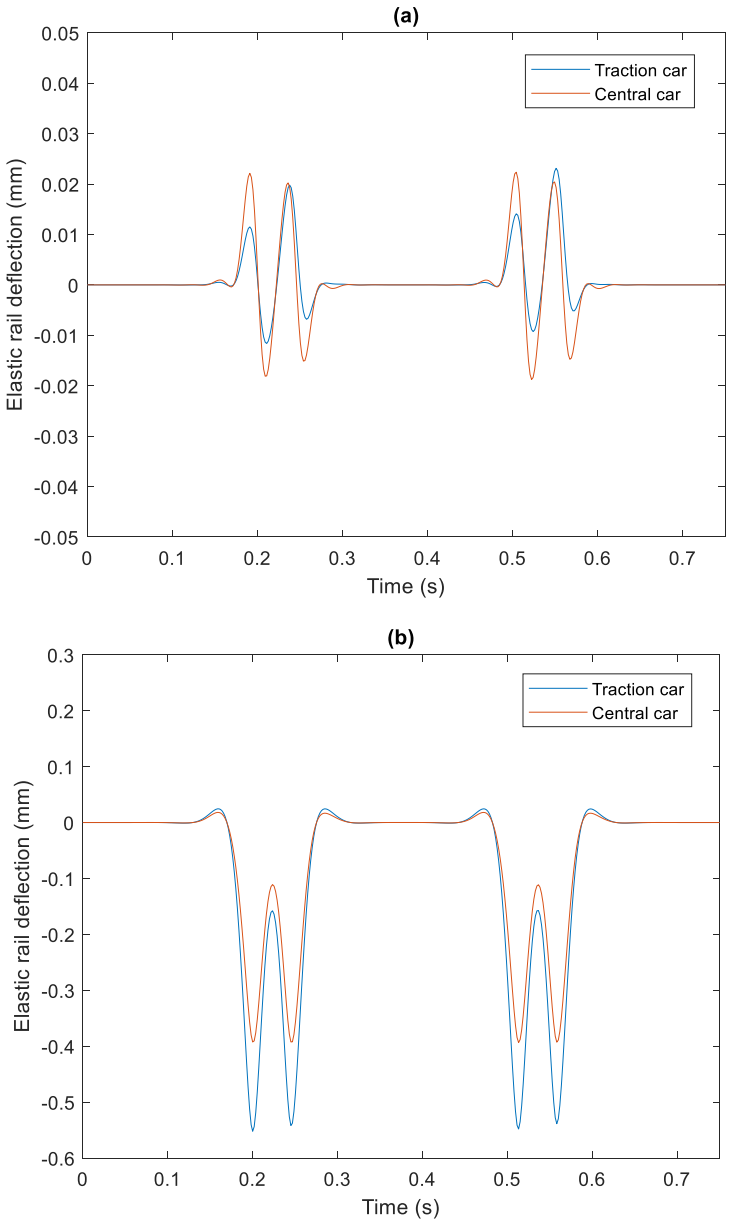

Figure 3.15 Rail deflection, traction car Vs central car: (a) dynamic excitation, (b) combined quasi-static and dynamic excitation.

3.4.2 Hertzian contact stiffness

Since the dynamic portion of the contact force is typically substantially less than the static action (weight of the train per wheel), the contact stiffness can be linearised considering only the portion of the force P corresponding to the distribution of the weight of the train per wheel (Sheng et al., 2003; Wu and Thompson, 2001). Therefore, a linearization procedure can be adopted, in which only the dead load transmitted by the wheelset is taken into account (Kouroussis et al., 2014). The linearised (Hertzian) contact stiffness is defined as:

$$k_H = \frac{3}{2G} P_0^{\,1/3} \quad \textbf{(3-72)}$$

where P_0 is the static load transmitted by the wheel to the rail; and G is the contact constant depending on the radius and geometry of the wheel, and rail bearing surface. For wheels with a tapered bearing surface and a flat bearing surface, the contact constants are approximated as Eqs. (3-73) and (3-74) respectively:

$$G = 4.57R^{-0.149} \times 10^{-8}\ (m/N^{2/3}) \quad \textbf{(3-73)}$$

$$G = 3.86R^{-0.115} \times 10^{-8}\ (m/N^{2/3}) \quad \textbf{(3-74)}$$

where R is the wheel radius.

3.4.3 Generation of track irregularity

The geometric irregularity of the track can be defined using either a synthetic profile or from data gathered by an in-service measurement vehicle. Track irregularities can be described using power spectral density (PSD) as a function of spatial frequency, of which there are various formulations. The formulation used in this work is based on the Federal Railway Administration (FRA) which divides the track into different classes for the quantification of track unevenness (Federal Railroad Administration, 1980). The formulation based on FRA has Eqs. (3-75) to (3-77):

$$S_n(k_x) = \frac{Ak_3^2(k_x^2 + k_2^2)}{k_x^4(k_x^2 + k_3^2)} \quad \textbf{(3-75)}$$

where the spatial frequency is $k_x = \frac{2\pi}{\lambda_{irr}}$, λ_{irr} is the wavelength of the irregularity, A is a roughness constant, and $k_2\ and\ k_3$ are spatial frequency constants. The values of each parameters are shown in Table 3.5. According to (Kouroussis et al., 2014), this representation should be limited to a wavelength range from 1.5m to 300m. Note that the values of parameters in Table 3.5 are taken from (Federal Railroad Administration, 1980) which are originally expressed as in^2-cy/ft for parameter A and cy/ft for parameter $k_2\ and\ k_3$.

Table 3.5 FRA parameters

Parameters		Track Classes							
Symbols	**Units**	**1**	**2**	**3**	**4**	**5**	**6**	**7**	**8**
A	10^{-6} m^2-rad/m	10.5053	5.9840	3.3245	1.8617	1.0505	0.5984	0.2394	0.0798
k_2	10^{-2} rad/m	14.639	14.639	14.639	14.639	14.639	14.639	18.350	23.092
k_3	10^{-2} rad/m	82.474	82.474	82.474	82.474	82.474	82.474	82.474	82.474
Operating speed limits	km/h	24.1	48.2	96.5	128.7	144.8	177.0	201.1	257.4

After computing the PSD, the amplitude of unevenness in terms of the spatial frequency is:

$$\delta u_j = \left(\sqrt{2 S_n \left(k_{x_j} \right) \Delta k_x} \right) e^{-i\theta_j} \quad \textbf{(3-76)}$$

where Δk_x is the resolution retained for the spatial frequency, and θ is phase angle, taken as a random variable with uniform distribution in the range 0-2π. The metric considered for threshold exceedance is the standard deviation over a 200m track length. Therefore the initial track profile in terms of position x is obtained using:

$$u_{irr}(x) = \sum_{j=1}^{N} \delta u_j e^{ik_{x_j} x} \quad \textbf{(3-77)}$$

In contrast to artificial track irregularities, measured irregularity profiles can also be used for simulating dynamic excitation. The raw signals from measurement are band-pass filtered to obtain signal wavelengths within the interested range. In addition, the signals are proceeded using a transformation from the space domain into the spatial frequency domain, since the analysis is conducted in the frequency domain. Instead of using the Fourier Transform, it is necessary to take into account the discrete nature of the digital signals. Therefore, a Discrete Fourier Transform is applied (Cooley and Tukey, 1965) to deal with the domain transformation process of the measured track irregularity profile.

3.4.4 Quasi-static versus dynamic excitation

Rolling stock moving at constant speed on a plain line induces both quasi-static and dynamic excitation. The track's quasi-static deflections, stresses and strains are not influenced by track irregularities meaning they move uniformly with the load (Connolly and Costa, 2020). Considering the well established relationships between stress and settlement, such loading therefore also induces uniform settlement along the track. In contrast, dynamic excitation is influenced by track irregularities and is thus the source of differential settlement evolution.

To illustrate this concept more clearly, Figure 3.16 shows the quasi-static and dynamic deviatoric stresses measured on the track centreline, 0.1m below the sleeper, for an entire 200m track length. Excitation is from the full freight train model interacting with a track irregularity of FRA's class 4 (suitable for maximum speed at 130km/h). The corresponding ballast settlement is shown in Figure 3.17. It is seen that the quasi-static excitation induces uniform settlement along the track, whereas the dynamic excitation induces non-uniform settlement along the track. This illustrates the concept that dynamic excitation is the primary driver of differential railway track settlement.

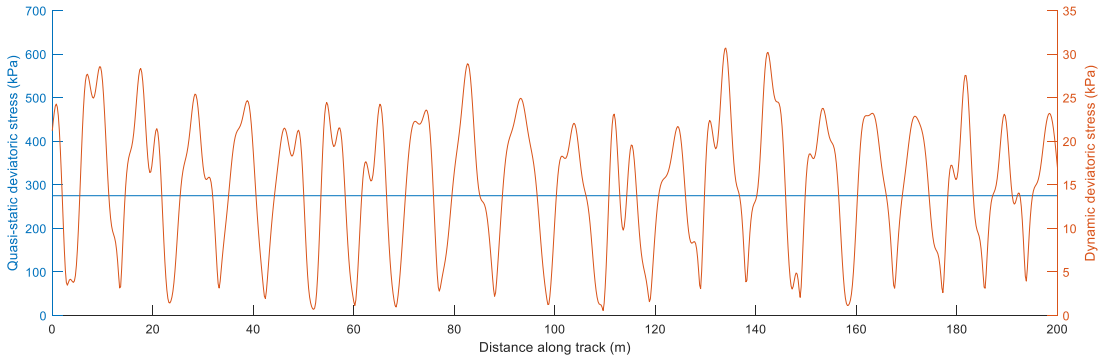

Figure 3.16 Track-bed deviatoric stress due to quasi-static and dynamic excitation

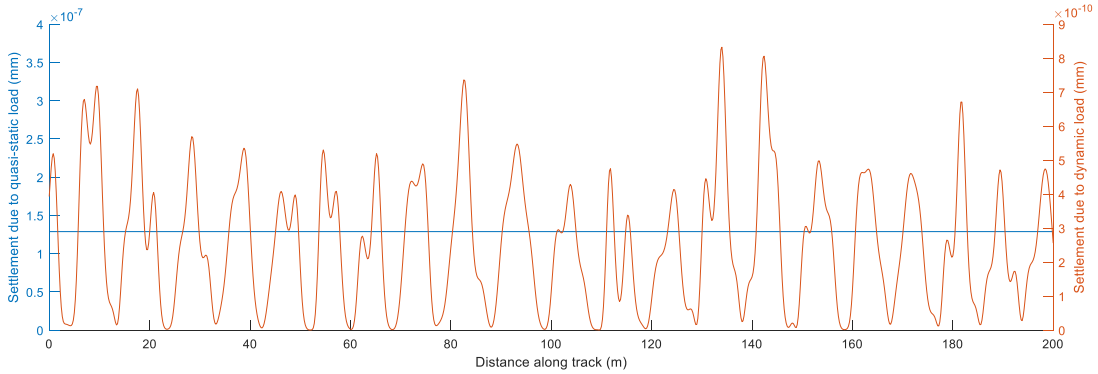

Figure 3.17 Track-bed settlement due to a single axle passage. Quasi-static and dynamic components

3.4.5 Dynamic stresses along the track

When calculating differential settlement, stresses along the track in the direction of the train's movement are determined. The total stress includes geostatic stress, quasi-static stress, and dynamic stress. Both geostatic and quasi-static stresses are assumed to be constant along the track and can thus be computed in advance before the iterative process. However, dynamic stresses vary based on irregularities in track geometry and are updated with every iteration when the track geometry profile changes. To compute dynamic stresses along the railway track considering the full vehicle model, the subsequent steps are undertaken:

1. Pre-calculate the unit load stresses $\sigma_{unit\_load}(\Omega, k_x)$ in the frequency Ω and wavenumber k_x domain. In this study, stresses are calculated every 0.2m along track length and at vertical depth intervals of 0.25m.
2. To minimise the run time during the calculation of dynamic stresses along the track within the iterative process, the unit load stresses $\sigma_{unit\_load}(\Omega, k_x)$ in the frequency Ω and wavenumber k_x domain are converted to the unit load stresses $\sigma_{unit\_load}(\Omega)$ in the frequency domain prior to the iterative process, using the following equation:

$$\sigma_{unit\_load}(\Omega) = \frac{1}{2\pi} \int_{-\infty}^{+\infty} \sigma_{unit\_load}(\Omega, k_x)\, dk_x \qquad \textbf{(3-78)}$$

3. Pre-calculate the variables $[V]$, $[V^H]$, $[T]$ and $b(\Omega)$ in Equation (3-57) based on the chosen vehicle model

4. Use Eq.(3-57) to calculate $F_{dyn\_1}(\Omega)$, $F_{dyn\_2}(\Omega)$, $F_{dyn\_3}(\Omega)$ and $F_{dyn\_4}(\Omega)$. These represent dynamic forces from the four wheels, with $\Delta u(\Omega)$ denoting the amplitudes of the updated track irregularity profile.
5. Calculate dynamic stresses in the frequency domain based on the dynamic forces from the four wheels:

$$\begin{aligned}\sigma_{dyn\_1}(\Omega) &= \sigma_{unit\_load}(\Omega) \times F_{dyn\_1}(\Omega)\\ \sigma_{dyn\_2}(\Omega) &= \sigma_{unit\_load}(\Omega) \times F_{dyn\_2}(\Omega)\\ \sigma_{dyn\_3}(\Omega) &= \sigma_{unit\_load}(\Omega) \times F_{dyn\_3}(\Omega)\\ \sigma_{dyn\_4}(\Omega) &= \sigma_{unit\_load}(\Omega) \times F_{dyn\_4}(\Omega)\end{aligned} \quad \textbf{(3-79)}$$

6. Before using the stresses to calculate settlement along the track, the four dynamic stresses in the frequency domain are transformed into the time-space domain using the following equation:

$$\begin{aligned}\sigma_{dyn\_1}(t) &= \sum_{j=1}^{N} \sigma_{dyn\_1}(\Omega_j) i\Omega_j t\\ \sigma_{dyn\_2}(t) &= \sum_{j=1}^{N} \sigma_{dyn\_2}(\Omega_j) i\Omega_j t\\ \sigma_{dyn\_3}(t) &= \sum_{j=1}^{N} \sigma_{dyn\_3}(\Omega_j) i\Omega_j t\\ \sigma_{dyn\_4}(t) &= \sum_{j=1}^{N} \sigma_{dyn\_4}(\Omega_j) i\Omega_j t\end{aligned} \quad \textbf{(3-80)}$$

3.5 Geostatic stress

In addition to the stresses induced by quasi-static and dynamic loads, the stress field due to geostatic loading is also included in the settlement calculation. In the context of moving loads on the railway track, stress calculations are focused solely on the track centreline, presuming it to be the critical location. This approach leads to the simplification of equations. The vertical stress at a given location is calculated from the mass of the overlying material:

$$\sigma_V = \rho g h_z \tag{3-81}$$

where σ_V is the vertical stress; ρ is the density of the overlying material; g is gravity; and h_z is the vertical distance from the monitored point to the free surface.

Considering an unsaturated soil, the total stress is equal to the effective stress due to the absence of pore water pressure. The effective horizontal stress is approximated as a proportion of the effective vertical stress:

$$\sigma'_H = K'_0 \sigma'_V \tag{3-82}$$

$$\frac{\sigma'_H}{\sigma'_V} = K'_o = \frac{\upsilon}{1-\upsilon} \tag{3-83}$$

where K'_0 is the coefficient of lateral stress (varying between 0 and 1.0).

To check the accuracy of the geostatic stress calculation in the 2.5D model, geostatic stresses were calculated in the track, at the location of settlement computation. The results are compared with results from a 3D model, simulated using commercial FE software ABAQUS (Figure 3.18). The result is a strong fit.

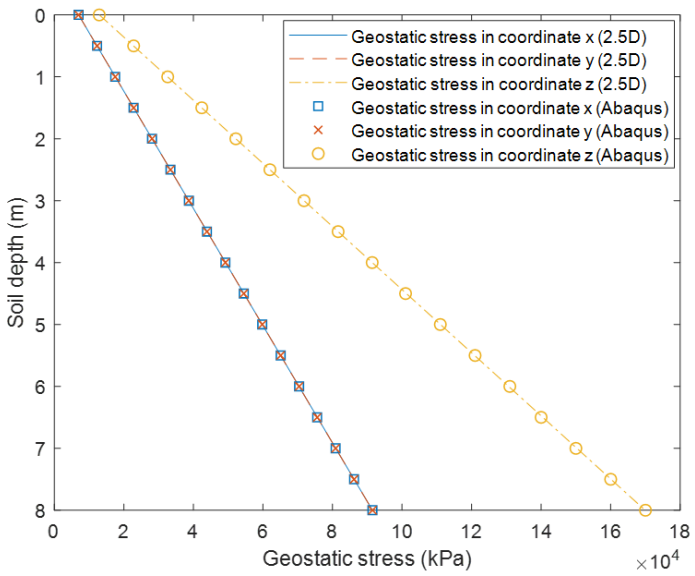

Figure 3.18 Geostatic stresses at the track centre

In case of saturated soil, a hydrostatic pressure is also presented in the pore water because of the presence of the water table. This pore pressure (u_w) is zero at the water table and increases linearly with increasing depth. Therefore, the hydrostatic pore water pressure at a depth of h_w below the water table is:

$$u_w = \rho_w g h_w \tag{3-84}$$

where u_w is the hydrostatic pore water pressure; ρ_w is the density of the water; and h_w is the vertical distance below the water table.

The difference between the total stress (σ) and the pore pressure (u_w) in a saturated soil is defined as the effective stress (σ'):

$$\sigma' = \sigma - u_w \tag{3-85}$$

Considering the stress field in 3D, the deviatoric stress is dependent on the sum of squares of the differences of the principal stresses:

$$\sigma_d = \sqrt{\frac{1}{2}} \times \sqrt{(\sigma_1 - \sigma_2)^2 + (\sigma_2 - \sigma_3)^2 + (\sigma_3 - \sigma_1)^2} \tag{3-86}$$

where σ_1, σ_2 and σ_3 are the components of the principal stresses. Note that the total deviatoric stress includes the geo-static, quasi-static and dynamic stress components.

3.6 Permanent strain and settlement models

3.6.1 Ballast settlement

Full-scale laboratory tests were performed using the apparatus described in (Esen et al., 2021; Marolt Čebašek et al., 2018; Ramos et al., 2021) and shown in Figure 3.19. A single sleeper was cyclically loaded with the equivalent of 20t and 32t axle loads. A 20t axle load represents a fully loaded passenger train, while a 32t axle load represents a heavy freight train (Kouroussis et al., 2014). A G44 concrete sleeper was tested, supported by a 0.4m depth of ballast and a 0.18m depth of well-compacted granular material. To replicate train loading, a sinusoidal loading function was applied at a frequency of 2Hz. Deformation was measured using linear variable differential transformers, placed on the sleeper and sampled at 200Hz.

Figure 3.19 Full scale ballast testing

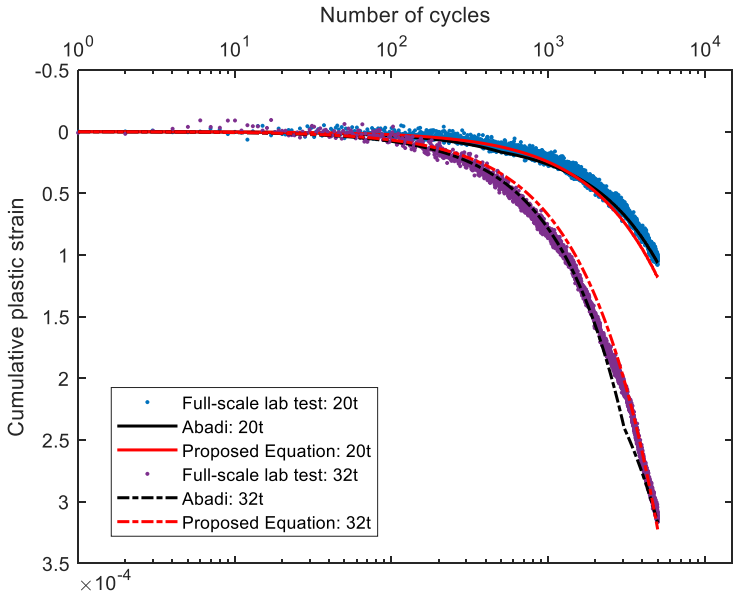

Figure 3.20 Comparison of experimental lab data against published datasets

The ballast settlement model is inspired by the ORE-type formulation (ORE, 1970) which depends upon the number of loading cycles, deviator stress and ballast porosity. The empirical constants are adjusted to improve the fit with the experimental data. Figure 3.20 compares the proposed equation against the experimental data and the data in the literature (Abadi et al., 2016). It should be noted that the permanent strain during the first cycles is removed to avoid any effects due to the initial rapid rearrangement of ballast particles during lab testing. The proposed equation shows a strong fit with the experimental data and the data in the literature for both 20 and 32 tonne tests..

A key advantage of using an iterative modelling approach is that the differential settlement and track profile can be updated after every load passage. However, this requires that the deviatoric stress must also be recalculated after every passage. Further, the equation must be able to compute settlement for varying scenarios, including:

1. The case of newly constructed or renewed/tamped track, where the ballast has only experienced minimal loading
2. The case of existing ballast, where the ballast has previously been compacted under a large volume of traffic

Considering these factors and the need to regularly update the track profile, an alternative form of the ORE settlement equation is required, that is able to account for the settlement of previous axle passages in its calculation. Therefore a modified permanent strain equation, computed at every iterative step is proposed:

$$\Delta\varepsilon_{p\_b,i} = 0.375\left(\sigma_{d\_b,i}\right)^2 \times \left[\left(1 + 0.4\,log_{10}\left((dN \cdot i) + N_{lb}\right)\right) - \left(1 + 0.4\,log_{10}\left((dN \cdot (i-1)) + N_{lb}\right)\right)\right] \quad \textbf{(3-87)}$$

The corresponding settlement is then:

$$\Delta S_{b,i} = \sum_{j=1}^{k} \Delta\varepsilon_{p\_b,i_j} \cdot h_j \quad \textbf{(3-88)}$$

where $\Delta\varepsilon_{p\_b,i}$ is ballast permanent strain increment; i is iterative step; $\sigma_{d\_b,i}$ is ballast dynamic deviatoric stress relevant to traffic load (in MPa); N_{lb} is the number of load cycles after the last ballast renewal/tamping; $\Delta S_{b,i}$ is ballast settlement increment; h_j is the thickness of each layer; k is number of sublayers. dN is the frequency of load application, for example where $dN = 1$ indicates every load passage is simulated, and $dN = 1000$ indicates every 1000th load passage is simulated.

The derived settlement equations are then modified to account for the differences in ballast compaction achievable in a laboratory setting versus a full-scale railway construction (Guo et al., 2022). An important difference between these compacted states is the application of Dynamic Track Stabilisation, commonly used on new lines particularly at higher speeds (Shi et al., 2022). Dynamic Track Stabilisation is often considered to provide the equivalent compactive effort as 100,000 tonnes. Therefore Figure 3.21 shows the unmodified ballast settlement curve and the modified settlement curve assuming the ballast has already received these loading cycles before experiencing live traffic.

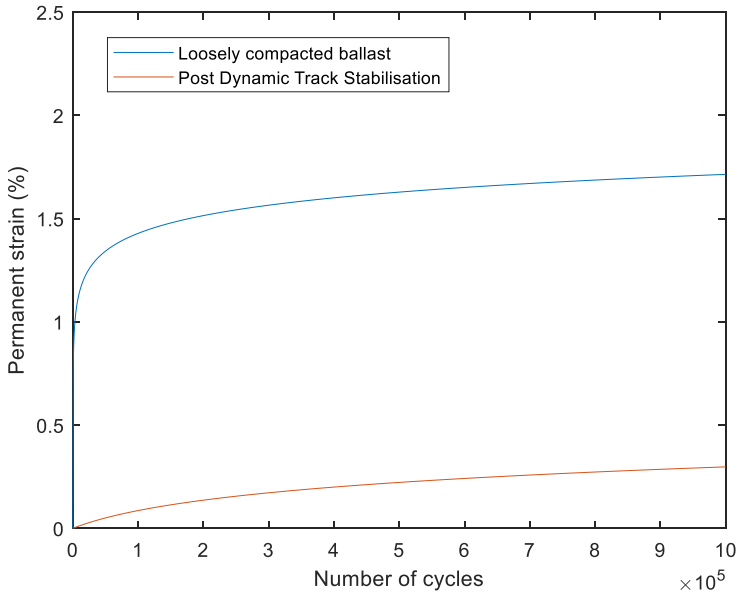

Figure 3.21 Typical ballast settlement curves

3.6.2 Subgrade settlement

The subgrade settlement equation is a modified version of that proposed by Li and Selig (Li and Selig, 1996). Similar to the approach for calculating ballast settlement, it is modified to take into account the evolution of dynamic stress and to allow for the simulation of both newly constructed track and existing subgrade. The proposed, modified permanent strain increment and settlement increment at each iterative step are:

$$\Delta\varepsilon_{p\_s,i} = \frac{a}{100}\left(\frac{\sigma_{d\_s,i}}{\sigma_s}\right)^m \left[\left((dN \cdot i) + N_{ls}\right)^b - \left((dN \cdot (i-1)) + N_{ls}\right)^b\right] \quad \textbf{(3-89)}$$

$$\Delta S_{s,i} = \sum_{j=1}^{k} \Delta\varepsilon_{p\_s,i_j} \cdot h_j \quad \textbf{(3-90)}$$

where $\Delta\varepsilon_{p\_s,i}$ is subgrade permanent strain increment; $\sigma_{d\_s,i}$ is subgrade dynamic deviatoric stress relevant to traffic load (in Pa); σ_s is soil compressive strength (in Pa); N_{ls} is the number of load cycles after the last subgrade replacement; $\Delta S_{s,i}$ is subgrade settlement increment; and a, m, and b are material parameters given in Table 3.6.

Table 3.6 Settlement material parameters

Soil type	Reference	Settlement material parameter		
		a	b	m
Fat clay, CH	(Li and Selig, 1996)	1.20	0.18	2.40
Lean clay, CL	(Li and Selig, 1996)	1.10	0.16	2.00
Elastic silt, MH	(Li and Selig, 1996)	0.84	0.13	2.00
Sand silt, ML	(Li and Selig, 1996)	0.64	0.10	1.70
Sand gravel	(Shi et al., 2012)	0.52	0.15	1.49

Figure 3.22 illustrates example settlement rates for three different cases. It should be noted that the presented graphs are idealised and replicated from (Li et al., 2015). Figure 3.22(a) is the case of new track construction (newly placed ballast and soft subgrade) where a soft subgrade provides higher settlement than the ballast in the years after construction. Alternatively, Figure 3.22(b) is where the track has been compacted under several years of traffic loading, but the ballast has recently been renewed. In this case the ballast settlement exceeds the subgrade, particularly in the initial period after tamping. The third case, as seen in Figure 3.22(c), shows when the ballast and subgrade have both been in place for many years. The deformation rates of both ballast and subgrade increase slowly with increased load passages.

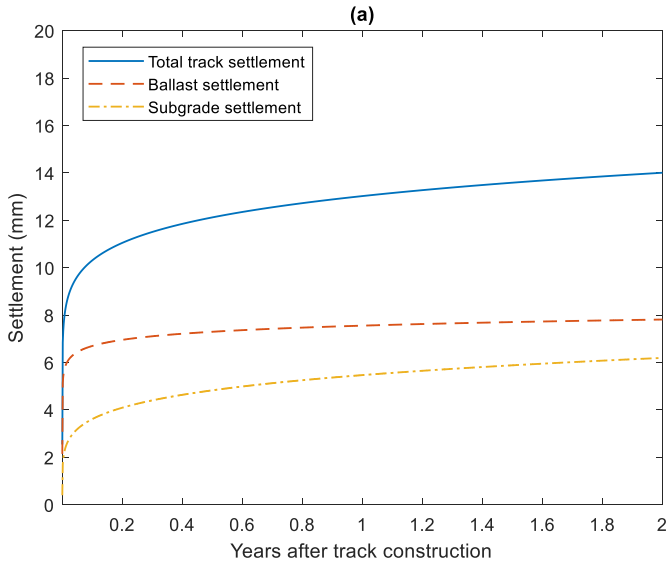

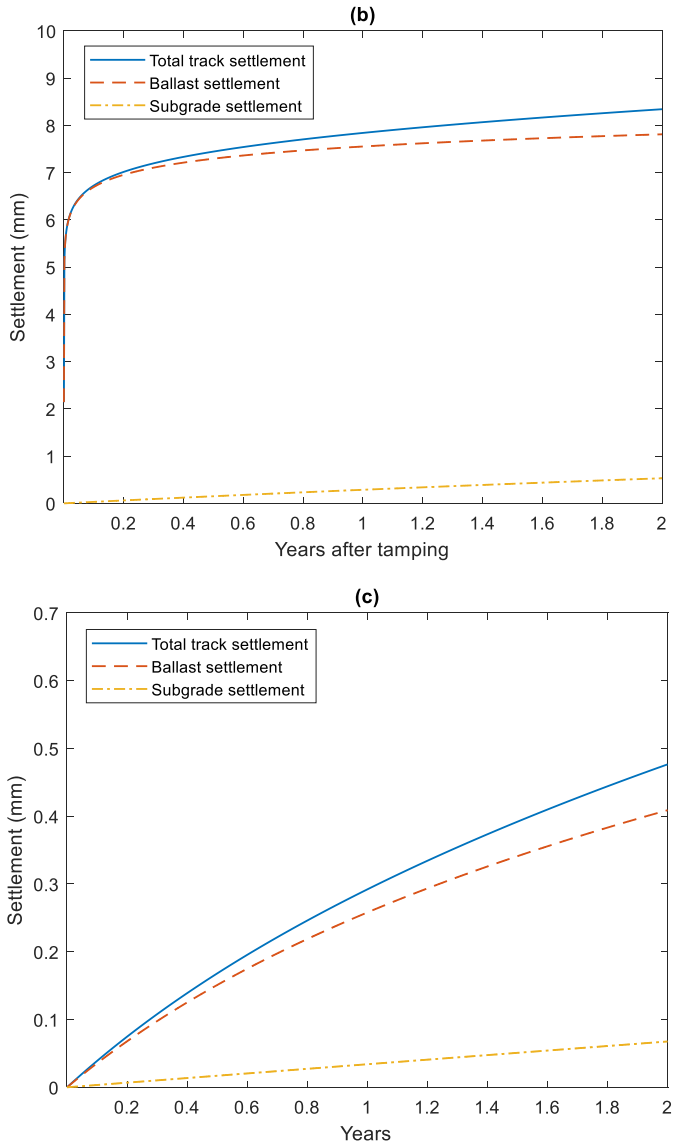

Figure 3.22 Ballast, subgrade, and total track settlement: (a) a newly constructed track (b) an existing track following tamping and (c) an existing track that has not recently been tamped (replicated from **(Li et al., 2015)**)

3.7 Detailed solution procedure

The previous sections outlined the general modelling strategy and key considerations. This section describes how they fit together to form the overall modelling methodology. Considering the modelling diagram of the two-step modelling approach shown in Figure 3.1, the sub-steps for the implementation of Step A are:

1. Calculate the geostatic stresses over the cross-section of the track structure
2. Determine the strain-adjusted material properties, considering non-linear material stiffness, due to quasi-static loading, using the 2.5D FEM-PML method

3. Compute the moving quasi-static and dynamic load transfer functions
4. Calculate the 3D stresses based on a unit load in the wavenumber-frequency domain
5. Compute the matrices of track compliance and train compliance

Step A only requires computation once, and when complete, the sub-steps for Step B are:

1. Calculate the train-track dynamic interaction forces based on the track irregularity profile and multi-body vehicle
2. Calculate the dynamic stresses along the entire track length. The calculation is performed in the wavenumber-frequency domain and then transformed to obtain the 3D dynamic stress fields in the time-space domain
3. Use the quasi-static, geostatic, and dynamic stresses to compute the deviatoric stress (σ_d)
4. Compute the permanent strain increments and the settlement increments in ballast and subgrade
5. Obtain the differential track settlement over the entire track length
6. Update the track geometry irregularity and perform a domain transformation to convert the updated signal into the spatial frequency domain
7. Return to step 1 and repeat the subsequent steps using the updated track geometry irregularity
8. Stop when threshold reached (e.g. total cycles or standard deviation threshold)

Chapter 4
Model validation

4.1 Introduction

This Chapter focuses on model validation, a step in assessing the accuracy and reliability of the developed model. Four validation cases are presented, each addressing different components of the model. In Validation Case 1, the model's short-term prediction capabilities are evaluated for both ballasted and slab tracks. Subsequently, Validation Case 2 examines the model's ability to simulate track-ground dynamics and nonlinear behaviour. Validation Case 3 focuses on validating the model's performance in simulating train-track interaction, while Validation Case 4 assesses its ability to predict differential settlement.

4.2 Validation case 1: Short-term prediction

Case 1 is to validate a short-term prediction for ballast and concrete slab track.

4.2.1 Ballasted track

The ballasted track model is validated against the experimental field data from a railway line near the town of Carregado in Portugal. The rolling stock is an Alfa-Pendular train composed of 6 vehicles, moving at 219km/h (Alves Costa et al., 2012). Regarding the geometric properties of the model, the ballasted track consists of ballast and sub-ballast on top of 9 soil layers supported by bedrock. The Young's modulus of soil layers 1 to 9 are 110.8MPa, 95.8MPa, 163.7MPa, 119,5MPa, 145.5MPa, 226.6MPa, 339MPa, 539.6MPa and 539.6MPa, respectively. The heights of ballast and sub-ballast are 0.57m and 0.55m, respectively. The ballast has the following material properties: Young's modulus $97\mathrm{MPa}$; Poisson's ratio 0.27; and density $1590\ \mathrm{kg/m^3}$. The same parameters but for sub-ballast are $212\mathrm{MPa}$, 0.3, and $1910\ \mathrm{kg/m^3}$.

Figure 4.1 compares the rail displacements in the time domain between the simulation and the field measurement. There is a strong match between the simulated and measured results, in terms of both magnitude and timing of the response.

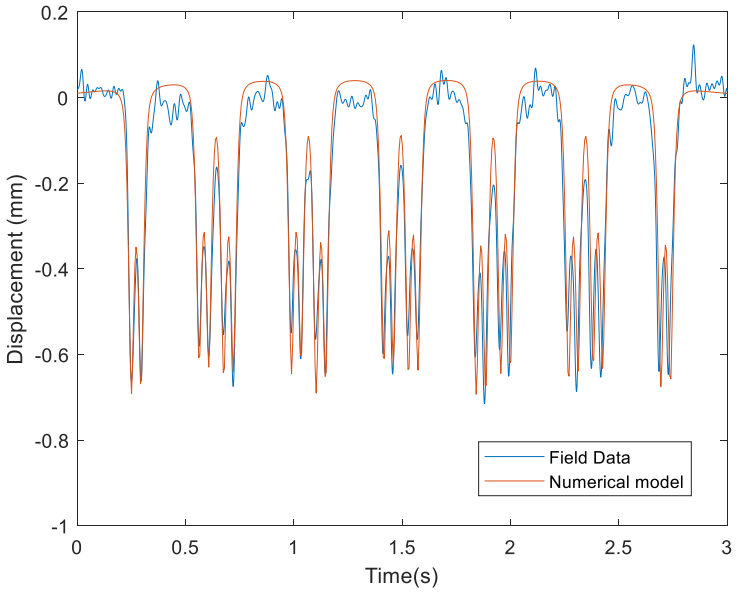

Figure 4.1 Ballast track validation - Rail displacement time histories due to the train passage

4.2.2 Slab track

A slab track model is validated against the measurement data of slab track displacements under train passages (Auersch and Said, 2019). The track consists of sleepers on a concrete track plate, and base layer on top of a soil layer (see Figure 4.2). The soil has a shear wave velocity of $100\mathrm{m/s}$, a density of $2000\mathrm{kg/m^3}$, and a Poisson's ratio of 0.33. The Young's modulus of the track plate and the base layer are 3×10^{10}Pa and 5×10^{9}Pa, respectively (Auersch and Said, 2019, 2017).

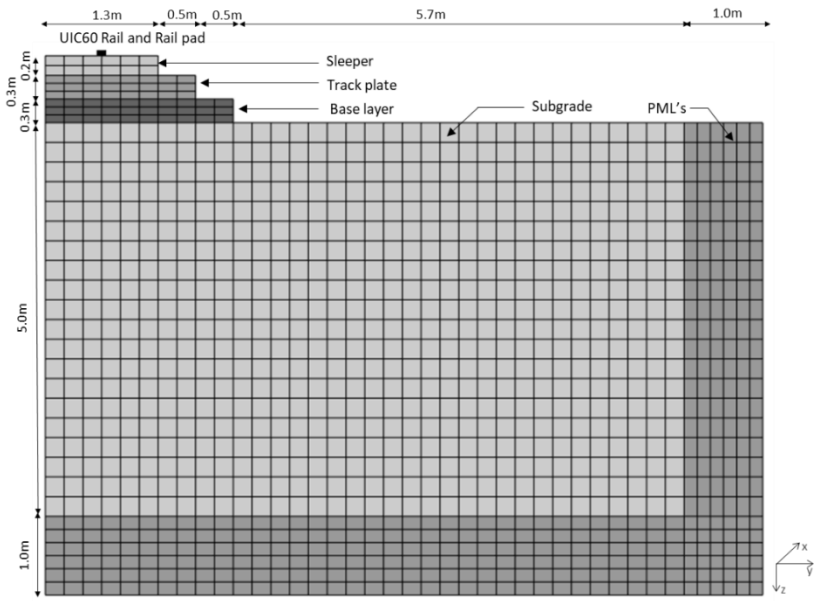

Figure 4.2 Finite element mesh for slab track validation

The displacement time histories measured at middle of track plate from the simulation and the measurement are compared as shown in Figure 4.3. The responses are due to the passage of an ICE train with a locomotive and 6 carriages, moving at 160km/h (Kouroussis et al., 2014). The agreement is strong between the predicted and measured values in terms of magnitude and timing of response. The central carriages provide a closer response than the first cars. This is most likely because the original measurements were recorded using accelerations and double integrating such signals is a longstanding railway challenge, which causes a drift in the measurement datum. In general, numerical integration can introduce numerical drift, where errors accumulate over time, leading to inaccuracies in the displacement estimation. This can be seen in the field data where the data appears to have been shifted upwards despite the track experiencing a heavier axle load.

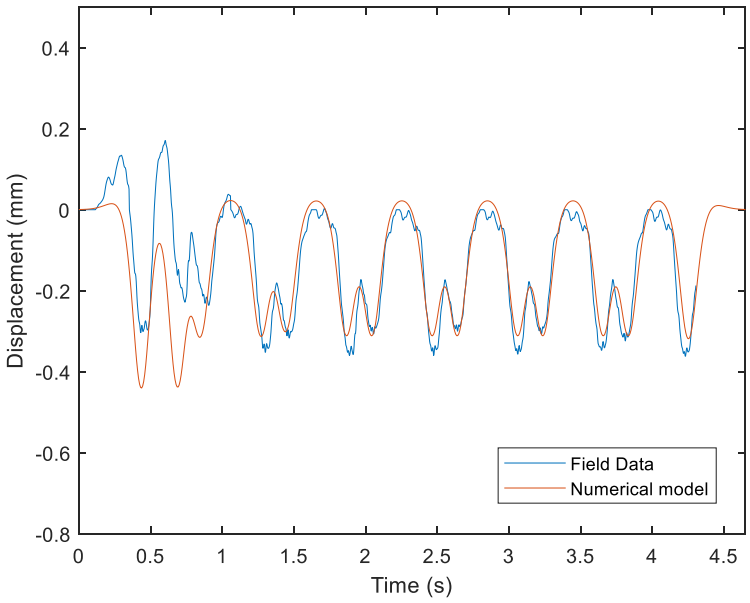

Figure 4.3 Concrete slab track validation - displacement time histories measured at the track plate centre

4.3 Validation case 2: Track-ground dynamics and non-linearity

Case 2 is to validate the model's ability to simulate track-ground dynamics and non-linear behaviour using an iterative linear equivalent procedure. The validation is performed using data from the case of a soft soil site at Ledsgard, Sweden (Madshus and Kaynia, 2000). This site experienced large deflections under the passage of X2000 trains shortly after opening, attributed to critical velocity effects (Connolly et al., 2020; Connolly and Costa, 2020), leading to soil non-linearity.

Regarding the material properties at the site, the UIC60 rail is continuously supported by railpads with a stiffness of 255×10^6 N/m^2 and a damping coefficient of 22.5×10^3 Ns/m^2. The sleepers are simulated using the aforementioned anisotropic constitutive model, with a Young's modulus of 30GPa. The low-strain soil properties are based on field test results and shown in Table 4.1. The experimental data for organic clay is taken from (Alves Costa et al., 2010). Embankment material properties are based on experimental data from (Dyvik and Kaynia, 2018). Figure 4.4(a) and (b) show the shear modulus reduction and damping ratio curves obtained using the empirical equations proposed by (Rollins et al., 2020) for the embankment, and (Ishibashi and Zhang, 1993) for the other soil layers. Train loading information is available in (Dong et al., 2019).

Table 4.1 Small-strain properties at Ledsgard

Layer	Thickness (m)	Density (kg/m3)	P-wave speed (m/s)	S-wave speed (m/s)	Damping ratio
Embankment	1.2	1800	210	340	0.04
Dry crust	1.1	1500	63	500	0.04
Organic clay	3.5	1260	41	500	0.02
Clay 1	4.5	1475	60	1500	0.05
Clay 2	6.0	1475	87	1500	0.05
Clay 3	30.0	1475	100	1500	0.05

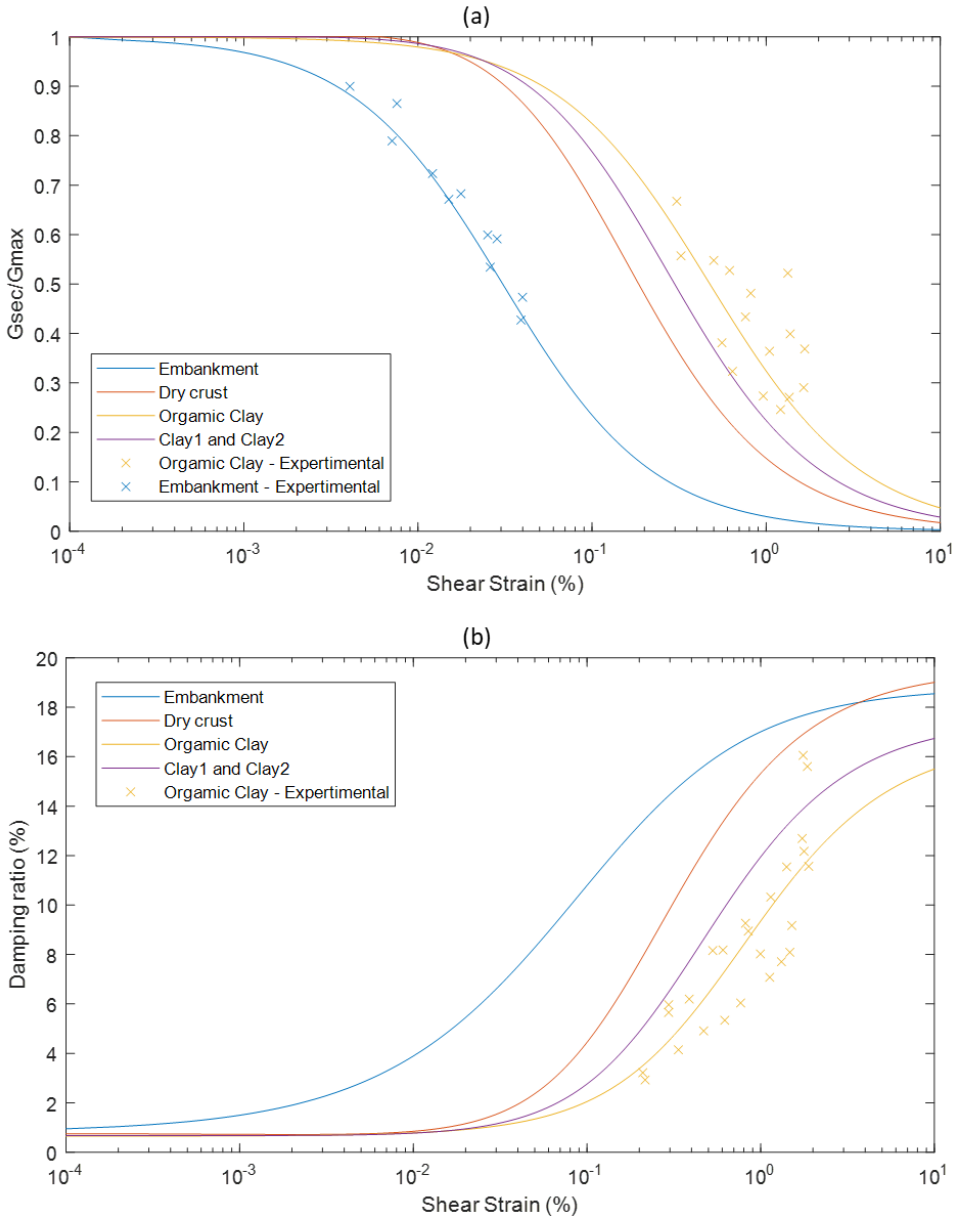

Figure 4.4 Non-linear soil characteristics (a) shear modulus reduction curves (b) damping ratio

The 3D track-ground displacement contour for a 70km/h train is illustrated in Figure 4.5. The deflection contours are visible and show the response propagating from the rail into supporting track-ground structure. Figure 4.6(a) and (b) show the examples of time histories of displacements calculated with and without considering non-linear effects, and compared with the field data for speeds of 70 km/h and 140 km/h, respectively. It can be seen that the results predicted by the non-linear simulation are a significantly better fit than the linear simulation. This is consistent with the works of (Dong et al., 2019) and (Alves Costa et al., 2010), and confirms the model's ability to simulate the non-linear part of the response. Figure 4.6(c) compares the peak upward and downward displacements between the field data, the linear simulation and the non-linear simulation for speeds ranging from 70 to 205 km/h. The comparison reveals that the results from the non-linear formulation are again a closer match with the field data. Therefore, it can be concluded that the model is capable of accurately calculating railway track deflections, regardless of whether the strain levels induce non-linear behaviour or not.

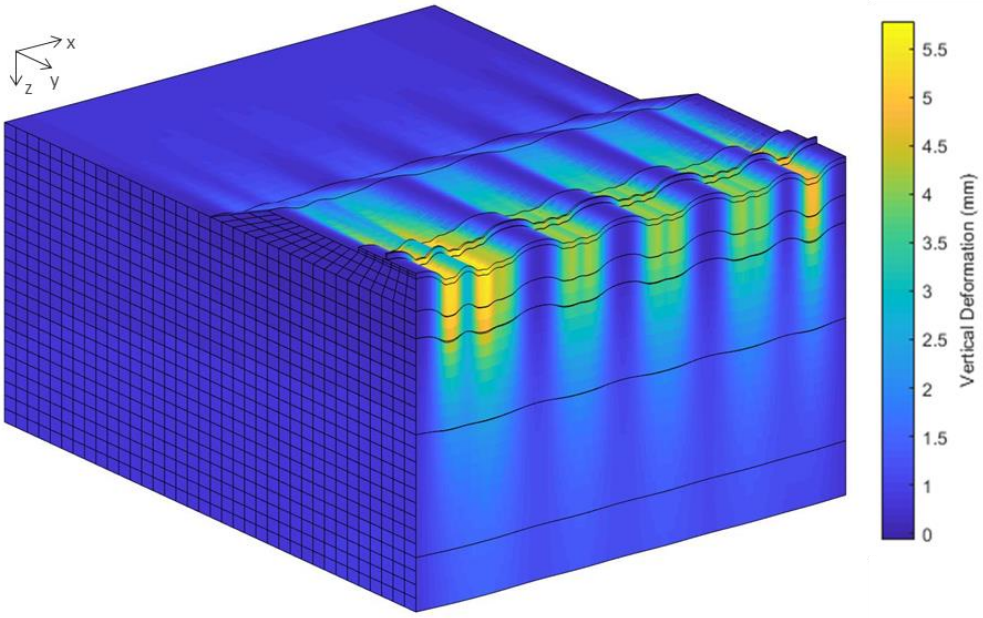

Figure 4.5 3D track-ground deflection profile (slice along track centreline)

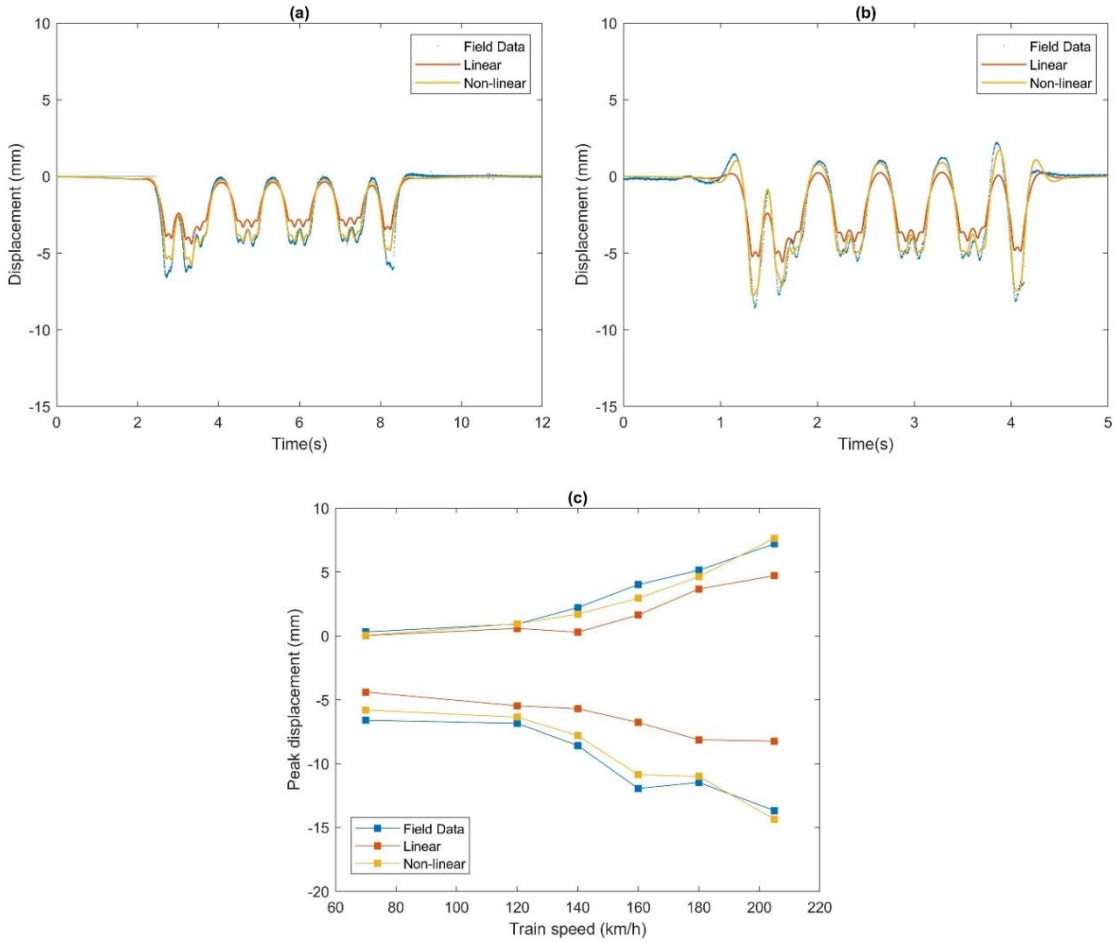

Figure 4.6 Measured and simulated time histories of track displacements for different train speeds (Southbound): (a) speed = 70km/h (b) speed = 140km/h (c) peak displacements versus train speeds

4.4 Validation case 3: Train-track interaction

Case 3 is used to validate the frequency-wavenumber domain solution method for train-track interaction. This is important for accurately calculating the forces that lead to the stresses in the track-subgrade. The validation is performed using an artificial track irregularity profile defined by FRA (Federal Railroad Administration, 1980) Class 5 for wavelengths in the range $3 < \lambda \leq 25\ m$. The model of train-track dynamic interaction in the frequency domain is validated against an equivalent time domain FE model (Thompson, 2008) solved using an implicit integration scheme. The time domain model is governed by:

$$F_{dyn} = \frac{i\omega r Y_r}{Y_r + Y_w + Y_c} \quad \textbf{(4-1)}$$

$$Y_r = \frac{i\omega u_{max}}{F_{sta}} \quad \textbf{(4-2)}$$

$$Y_w = \frac{-i}{\omega M_w} \tag{4-3}$$

$$Y_c = \frac{i\omega}{k_H} \tag{4-4}$$

where $i\omega r$ is the roughness velocity amplitude; Y_r is the vertical rail mobility; Y_w is the wheel mobility; Y_c is the contact spring mobility; u_{max} is the maximum displacement due to static load; F_{sta} is the static load; and M_w is the wheelset mass.

The validation is a simplified 2D model of a railway track as shown in Figure 4.7. The rail is represented using an infinite Euler-Bernoulli beam supported by a single continuous elastic layer. It has the following material properties: Young's modulus $E=2.1\times10^{11}N/m^2$; second moment of area $I=30.55\times10^{-6}m^4$; cross section area $A=0.00763m^2$; density $\rho=7850kg/m^3$ and support stiffness $s=1x10^8N/m^2$. A single axle vehicle travels across the structure at speed of 150 km/h, with wheel mass $M_w=2003kg$. The load on the wheel (from weight of the vehicle) is 195kN.

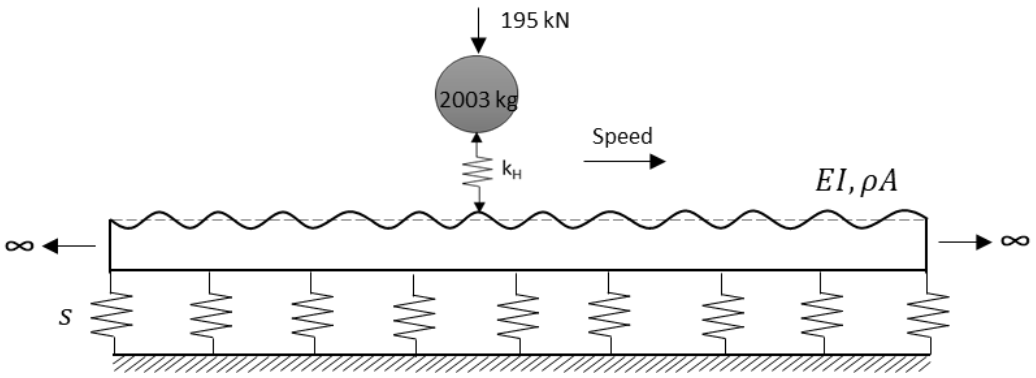

Figure 4.7 Simplified 2D train-track interaction problem

Figure 4.8 shows a comparison of displacement time histories between the time domain model and the frequency domain model. It should be noted that the displacements are only due to the dynamic load and not combined with the quasi-static load. A good match of the results confirms the accuracy of the train-track dynamic interaction model.

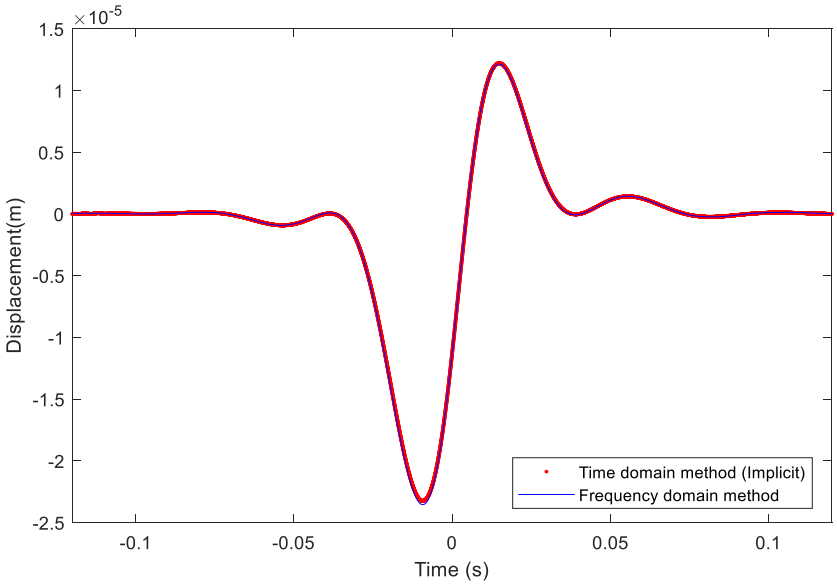

Figure 4.8 A comparison of displacement time histories due to dynamic loading

After computing the wheel-rail dynamic interaction forces in the frequency-wavenumber domain, the rail displacements can be computed using the Green's function. Then, the results of displacement in the wavenumber-frequency domain can be transformed into the time-space domain by means of a double inverse transform. A combination of both results from dynamic load (wheel-rail interaction) and quasi-static load (weight of the train) is the total rail displacement of the system. Five case examples of rail displacement calculation considering train-track interaction are demonstrated.

1) Single sprung mass on a constant irregularity
   The harmonic amplitude of track unevenness and the wavelength are used as Δu=0.001m and λ=2.4m respectively. The result of rail displacements due to the wheel-rail dynamic interaction force and the weight of train is shown in Figure 4.9.

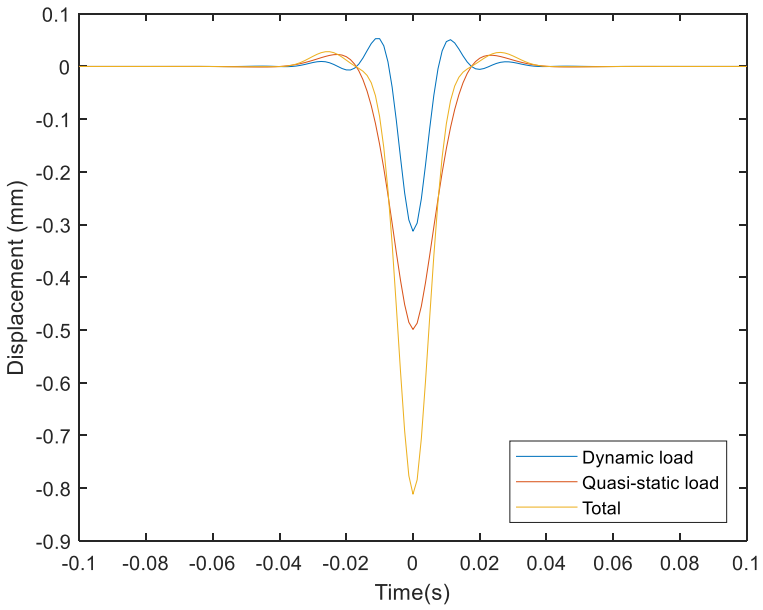

Figure 4.9 Single sprung mass on a constant irregularity

2) Single sprung mass with FRA irregularities

The rail displacements due to a single sprung mass moving on FRA track class 1 and class 6 are compared as shown in Figure 4.10. It is assumed that the loads move at the same speed. This is clear that the displacement due to the dynamic load from track class 1 (poor track quality) is higher than that of track class 6 (good track quality).

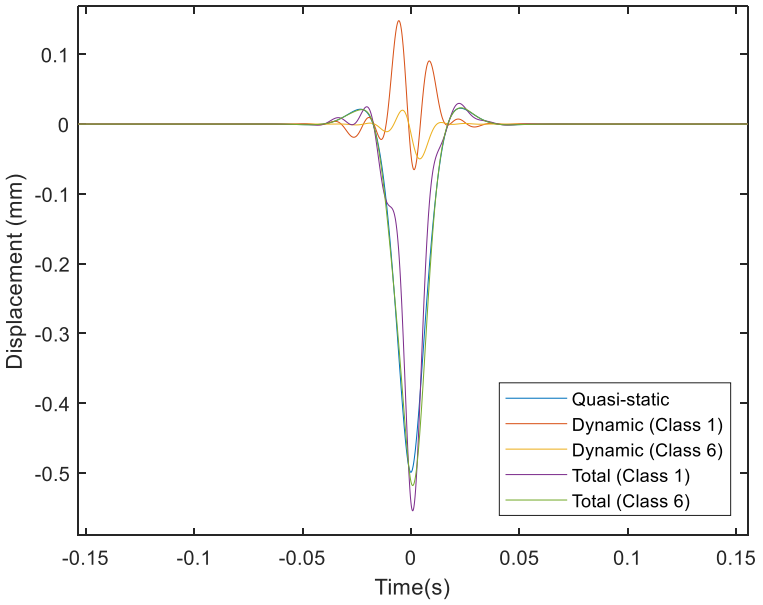

Figure 4.10 Single sprung mass with FRA irregularities

3) Two sprung masses with FRA irregularities

The rail displacement from two sprung masses is computed which the distance of the first mass is 5m before the second mass. The class 6 of

FRA track irregularity is used in this example. As shown in Figure 4.11, the displacement can be calculated by taking an advantage of receptance based on the Green's function.

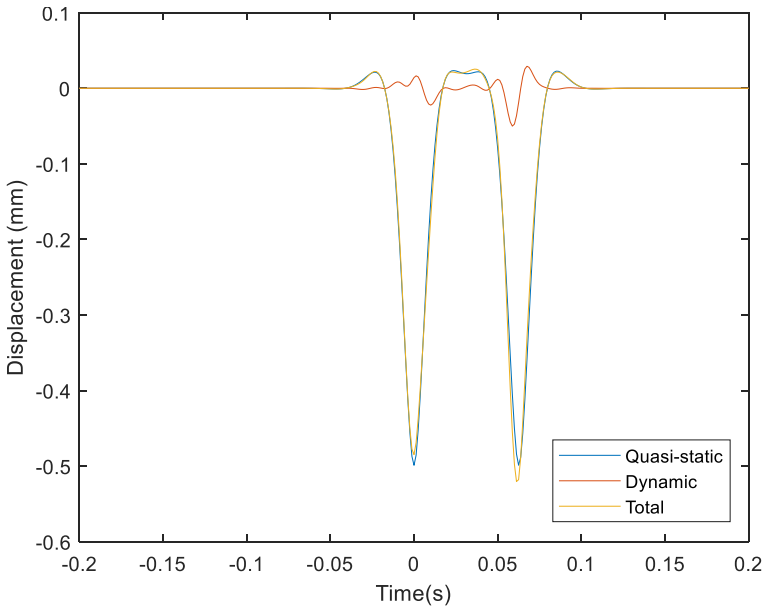

Figure 4.11 Two sprung masses with FRA irregularities

4) Simple vehicle model with FRA irregularities
A general vehicle model with 4 axle loads moving on the class 6 of FRA track irregularity is considered. The detail of vehicle model is explained in the previous Chapter. The results of the displacement are shown in Figure 4.12.

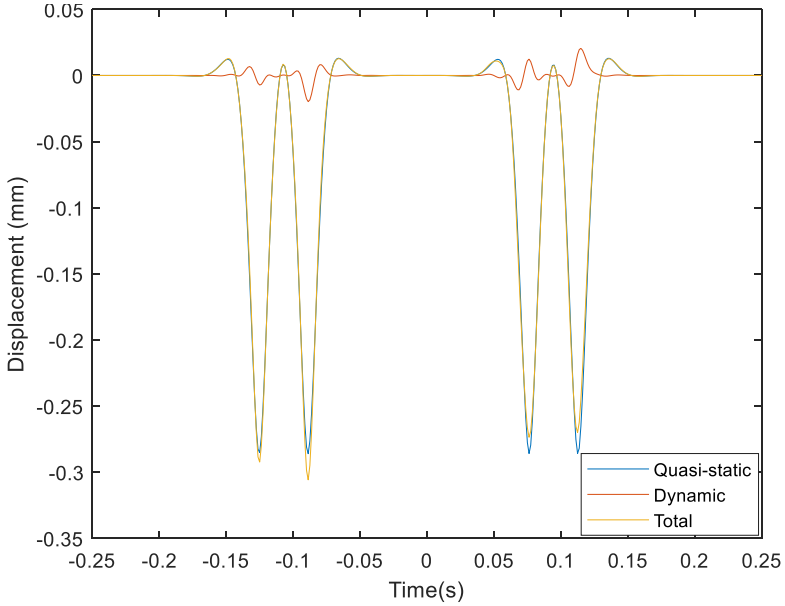

Figure 4.12 Simple vehicle model with FRA irregularities

5) Single sprung mass with real-life irregularity data
In case of considering the real-life irregularity data record, the recording data is processed and transformed into the frequency domain as an input in the train-track interaction model. Based on the recording of the vertical geometric irregularity of the rail in the railway section from the main line from Dagenham Junction to Eurotunnel boundary, the displacement is shown in Figure 4.13.

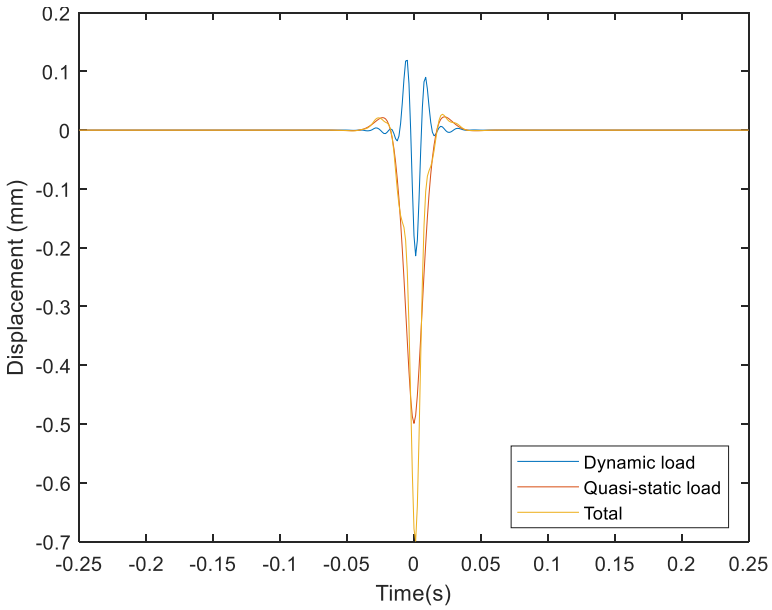

Figure 4.13 Simple sprung mass with real-life irregularity data

4.5 Validation case 4: Differential settlement

Case 4 is to validate the model's ability to compute the evolution of vertical track geometry with increasing axle passages. Historical track geometry data, from two track sections in the UK, are used for comparison. The data were collected using a track recording vehicle, and the standard deviation of the vertical track irregularity profile over a 200m track length is considered. Considering an aim of the model is to predict tamping intervals, only wavelengths in the 3-25m range are considered.

Regarding the first track section, Figure 4.14 shows the finite element mesh and dimensions of the track cross-section. The material properties of the rails, rail pads, sleepers, ballast, sub-ballast and subgrade are described in Table 4.2. The line operates almost exclusively with passenger rolling stock, and thus the vehicle properties are solely based upon the passenger vehicle shown in Chapter 3. The traffic volume per year is 19.58 million gross tonnes (MGT) with

an operational line speed of 125mph. To facilitate validation, track geometry obtained via a Track Recording Vehicle (TRV/TRC) on 5 dates: 10-November-2014, 23-March-2015, 07-March-2016, 20-March-2017 and 19-March-2018, is used. Analysis of maintenance records shows that tamping was not performed between any of these dates.

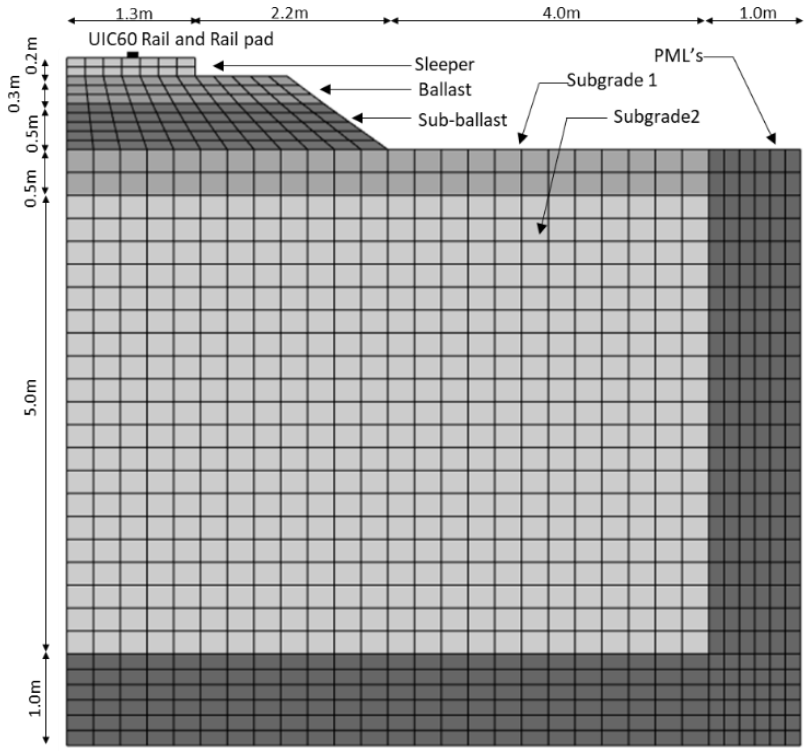

Figure 4.14 Finite element mesh of track section 1 for validation

The geometry data recorded on 10-Nov-2014 is used as the track starting condition. Then the model individually simulates every axle load passage until 19-March-2018. The geometry SD evolution is compared against the TRV data, as shown in Figure 4.15. The rectangular markers represent the geometry SD data recorded in-situ, and the triangle marker is the SD of the initial 2014 track profile. The dashed line represents the predicted geometry SD, evolving after every axle passage. The strong correlation between the predicted geometry SD curve and the real data confirms the model is capable of predicting the evolution of differential track settlement.

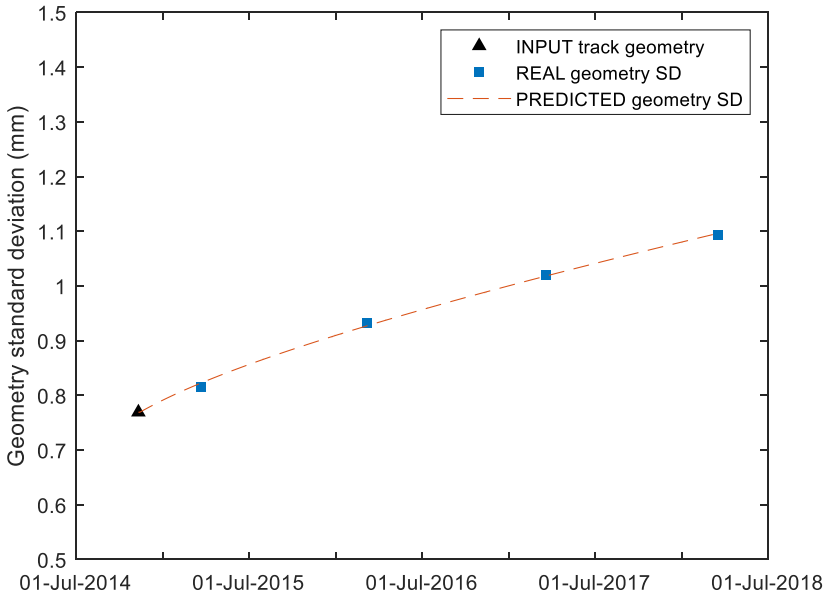

Figure 4.15 Validation of vertical rail profile SD over time: predicted vs field data (Track section 1)

Table 4.2 Ballasted track properties of track section 1

Component	Parameter	Value
UIC 60 Rail (single rail)	Height (m)	0.172
	Length in transversal direction (m)	0.015
	Section area (m^2)	7.677×10^{3}
	Moment of Inertia y-y (m^4)	3.038×10^{-5}
	Moment of Inertia z-z (m^4)	0.512×10^{-5}
	Young's modulus (Pa)	2.11×10^{11}
	Density (kg/m^3)	7850
	Poisson's ratio	0.3
	Hysteretic damping coefficient	0.01
Railpad (spring element)	Continuous stiffness (N/m^2)	255×10^{6}
	Viscous damping (Ns/m^2)	22.5×10^{3}
Sleeper (G44)	Height (m)	0.2
	Length in transversal direction (m)	2.5
	Sleeper spacing (m)	0.65
	Young's modulus (Pa)	3×10^{10}
	Density (kg/m^3)	2500
	Poisson's ratio	0.15
	Hysteretic damping coefficient	0.01
Ballast	Height (m)	0.3
	Length in transversal direction (m)	2.8

Component	Parameter	Value
	Young's modulus (Pa)	$180x10^6$
	Density (kg/m^3)	1600
	Poisson's ratio	0.27
	Hysteretic damping coefficient	0.061
Sub-ballast	Height (m)	0.5
	Length in transversal direction (m)	3.5
	Young's modulus (Pa)	$212x10^6$
	Density (kg/m^3)	1913
	Poisson's ratio	0.3
	Hysteretic damping coefficient	0.054
Subgrade layer 1	Height (m)	0.5
	Young's modulus (Pa)	$30x10^6$
	Density (kg/m^3)	2000
	Poisson's ratio	0.3
	Hysteretic damping coefficient	0.03
	Settlement parameter a	0.64
	Settlement parameter b	0.10
	Settlement parameter m	1.70
	Compressive strength (kPa)	100
Subgrade layer 2	Height (m)	5
	Young's modulus (Pa)	$80x10^6$
	Density (kg/m^3)	2000
	Poisson's ratio	0.3
	Hysteretic damping coefficient	0.03
	Settlement parameter a	0.64
	Settlement parameter b	0.10
	Settlement parameter m	1.70
	Compressive strength (kPa)	220

Regarding track section 2, the site investigation data was collated and the properties of the track are the same as track section 1. The finite element track mesh is also the same as track section 1, however only the thin upper soil layer is removed. The subgrade is ML soil type (silt) with a shear strength of 25 kPa. The subgrade properties and settlement parameters are shown in Table 4.3. The site was specifically selected to have minimal freight traffic, thus reducing the variation in rolling-stock types. Regarding the traffic condition, the line speed is 201 km/h with annual tonnage of 37 million gross tonnes (MGT), 98%

of which is passenger. Over a year period, track geometry was measured on 04-Jan-2017, 26-Mar-2017, 16-Aug-2017, and 16-Dec-2017, and no tamping took place between these dates.

Table 4.3 Subgrade properties of track section 2

Component	Parameter	Value
Subgrade	Young's modulus (Pa)	$60x10^6$
	Density (kg/m^3)	2000
	Poisson's ratio	0.35
	Hysteretic damping coefficient	0.03
	Settlement parameter a	0.64
	Settlement parameter b	0.10
	Settlement parameter m	1.70

The initial vertical track profile, measured on 04-Jan-2017 was used as the starting geometry. The model then simulated and updated the track geometry profile, after every individual load passage, based upon expected MGT. Over the course of almost a year, the evolving track geometry profiles are shown in Figure 4.16. The predicted profile for the final track recording is also shown and compared against the numerical simulation. It is seen that the amplitudes are closely matched in phase and amplitude. There are some discrepancies, however these are most likely due to varying track-ground material properties along the track section, which are difficult to capture from a single-point site investigation, and the fact that the true traffic was not 100% passenger rolling stock.

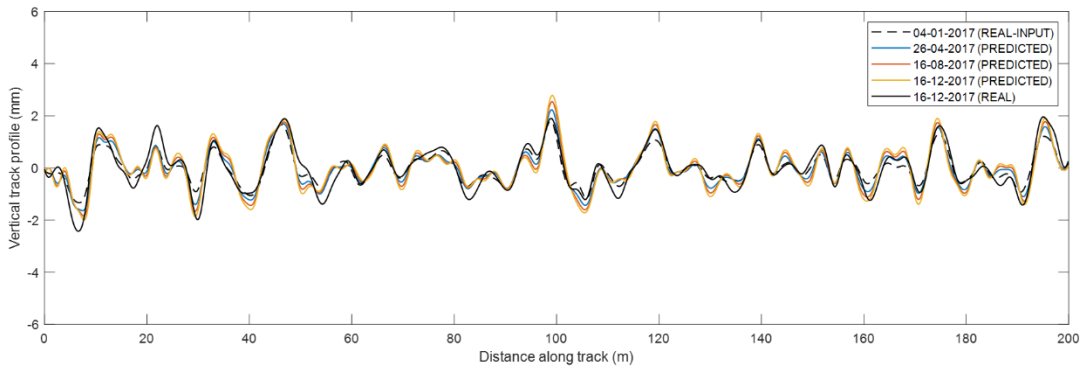

Figure 4.16 Vertical track profile. Predicted profile vs field data

Figure 4.17 compares the recorded and predicted evolution of geometry SD at the site. The rectangular markers are the real geometry SD from the recording car, and the red marker is the SD of the initial vertical track profile. The blue solid line is the predicted geometry SD updated after every load cycle during simulation. Compared to the real data, it is seen that the predicted geometry SD curve is a strong match to the recording data. This result, combined with the results in Figure 4.16, shows the strong ability of the model to accurately predict differential settlement and standard deviation evolution.

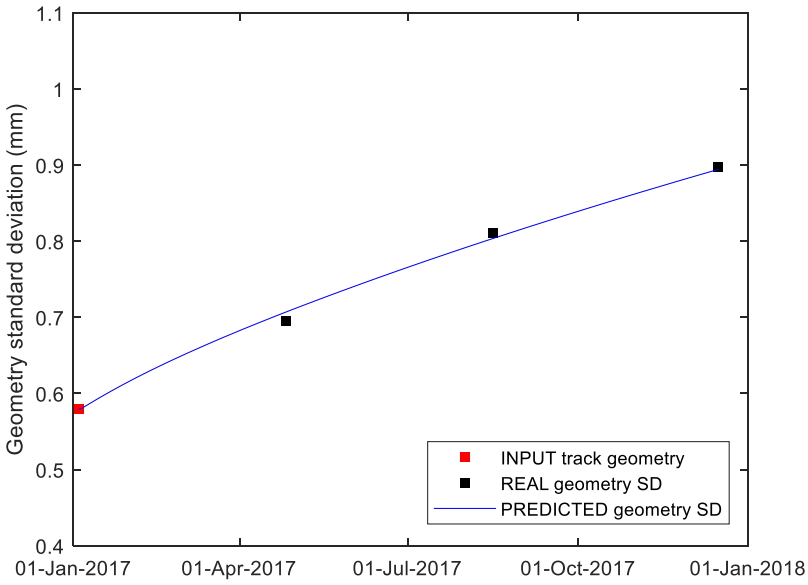

Figure 4.17 Validation of vertical rail profile SD over time: predicted vs field data (Track section 2)

4.6 Summary

In Validation Case 1, the model successfully predicts short-term responses for both ballasted and slab tracks, exhibiting strong agreement with measured results. Validation Case 2 confirms the model's ability to accurately calculate railway track deflections, regardless of whether strain levels induce nonlinear behaviour or not, with results from the non-linear formulation closely matching field data. Furthermore, Validation Case 3 confirms the accuracy of the train-track dynamic interaction model through a good match of results. Finally, in Validation Case 4, the model effectively computes the evolution of vertical track geometry, demonstrating a strong correlation between the predicted and the field data, thereby affirming its ability to predict differential track settlement. Overall, these validation cases underscore the reliability and accuracy of the developed model in representing real-life railway track behaviour.

Chapter 5
Analysis of subgrade material properties

5.1 Introduction

In the previous Chapter, a novel numerical approach, capable of predicting track irregularity evolution for a wide range of situations are validated. This is to confirm its ability to accurately simulate track-ground dynamics and non-linearity, its ability to model train-track interaction, and its ability to predict future changes in vertical track profile.

In this chapter, the validated model is used to investigate the influence of updating the track geometry after each axle load on the differential settlement prediction. Furthermore, the effect of changing the elastodynamic and settlement properties of the subgrade are investigated.

5.2 Effects of subgrade material properties on differential settlement

The subgrade material model is characterised by: 1) elastodynamic properties, that describe the propagation of stress fields, and 2) settlement properties that describe how these stress fields result in settlement. To understand the relation between these properties, a sensitivity analysis is performed by changing the Young's modulus and also the settlement parameters (a, b and m), again considering a new track construction. Figure 5.1 shows the finite element mesh used for the numerical analysis. The characteristics of the rails, rail pads, sleepers, ballast, sub-ballast and subgrade are described in Table 5.1. The two Young's modulus values of subgrade are used to represent a stiff and soft soil. The four settlement parameters are shown in Table 5.2. It should be noted that the sensitivity analysis was performed to understand the relationship between parameters, rather than to attempt to simulate any specific soil types.

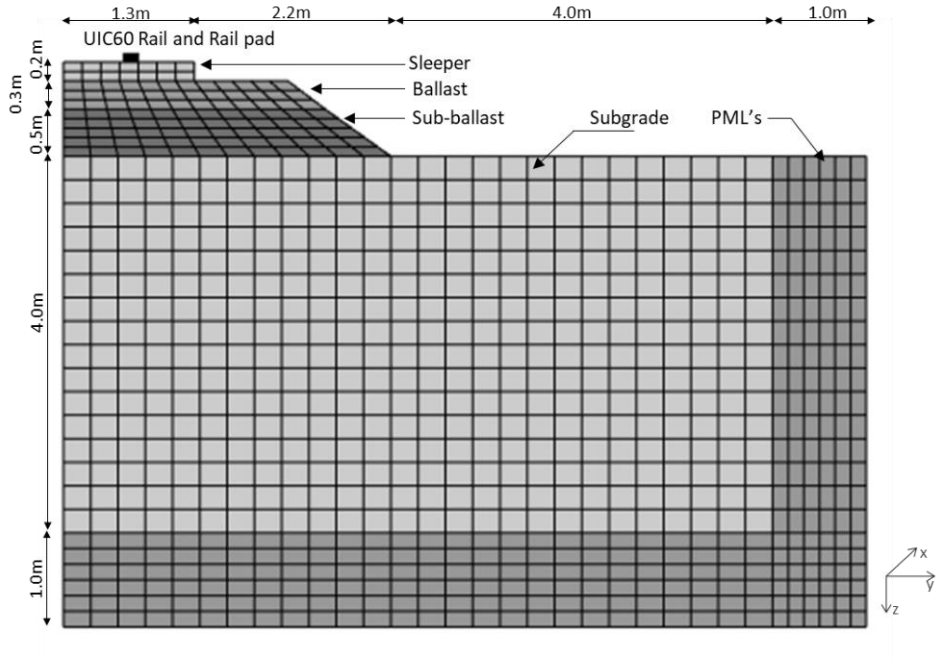

Figure 5.1 Finite element mesh

Table 5.1 Ballasted track properties

Component	Parameter	Value
UIC 60 Rail (single rail)	Height (m)	0.172
	Length in transversal direction (m)	0.015
	Section area (m^2)	7.677×10^{3}
	Moment of Inertia y-y (m^4)	3.038×10^{-5}
	Moment of Inertia z-z (m^4)	0.512×10^{-5}
	Young's modulus (Pa)	2.11×10^{11}
	Density (kg/m^3)	7850
	Poisson's ratio	0.3
	Hysteretic damping coefficient	0.01
Railpad (spring element)	Continuous stiffness (N/m^2)	255×10^{6}
	Viscous damping (Ns/m^2)	22.5×10^{3}
Sleeper (G44)	Height (m)	0.2
	Length in transversal direction (m)	2.5
	Sleeper spacing (m)	0.65
	Young's modulus (Pa)	3×10^{10}
	Density (kg/m^3)	2500
	Poisson's ratio	0.15
	Hysteretic damping coefficient	0.01
Ballast	Height (m)	0.3
	Length in transversal direction (m)	2.8

Component	Parameter	Value
	Young's modulus (Pa)	$180x10^6$
	Density (kg/m^3)	1600
	Poisson's ratio	0.27
	Hysteretic damping coefficient	0.061
Sub-ballast	Height (m)	0.5
	Length in transversal direction (m)	3.5
	Young's modulus (Pa)	$212x10^6$
	Density (kg/m^3)	1913
	Poisson's ratio	0.3
	Hysteretic damping coefficient	0.054
Subgrade case 1	Young's modulus (Pa)	$120x10^6$
	Density (kg/m^3)	2000
	Poisson's ratio	0.3
	Hysteretic damping coefficient	0.03
	Primary wave speed (m/s)	284
	Secondary wave speed (m/s)	152
Subgrade case 2	Young's modulus (Pa)	$60x10^6$
	Density (kg/m^3)	2000
	Poisson's ratio	0.3
	Hysteretic damping coefficient	0.03
	Primary wave speed (m/s)	201
	Secondary wave speed (m/s)	107

Table 5.2 Settlement parameters a, b, and m for various subgrade soil types

Material parameter	High-plasticity clay (CH)	Low-plasticity clay (CL)	High-plasticity silt (MH)	Low-plasticity silt (ML)
a	1.20	1.10	0.84	0.64
b	0.18	0.16	0.13	0.10
m	2.40	2.00	2.00	1.70

Figure 5.2 shows the change in geometry standard deviation versus load cycles, for changing settlement parameters: ML, MH, CL, CH, and for the stiff and soft soils. Considering Soil case 1 (stiff), the standard deviation for ML soil is 0.149mm. For the other soil types, the standard deviation increases by 4.09%, 7.84% and 16.49% for MH, CL and CH respectively. Similar is true for Soil case 2 (soft), where the same soil types cause increases of 4.74%, 8.38%

and 20.66% respectively. Therefore it can be concluded that the higher the clay content in the soil, the larger the settlement. However, although the settlement parameters have a marked difference on track geometry, the difference between the soft and stiff soil is even greater. The soft soil has a significantly higher standard deviation for all settlement parameters, which shows the importance of subgrade stiffness on track performance.

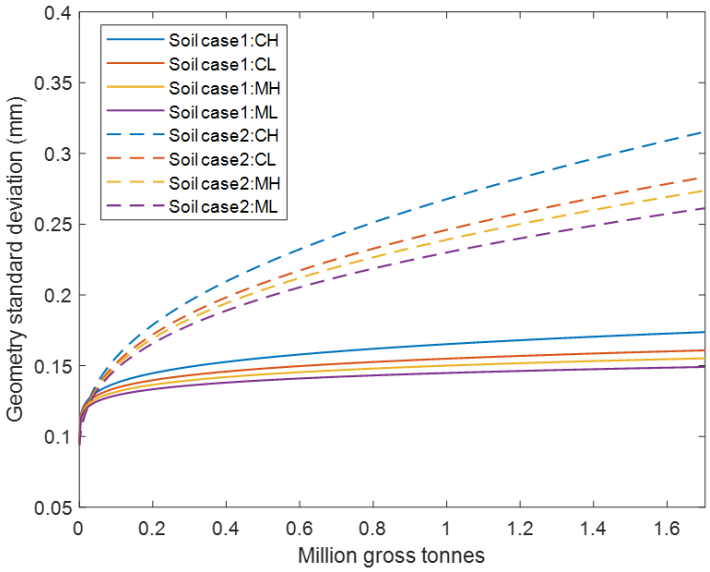

Figure 5.2 Track geometry evolution for varying subgrade properties

It is seen that both elastodynamic and settlement properties significantly influence on the evaluation of track geometry profile and deterioration. These properties are directly relevant to different soil types. However, there is still a number of influential variables that affect the track and the vehicle. Therefore, design charts can possibly be developed after performing more analyses.

5.3 Influence of continually updating track geometry

The validated model is used to analyse the effect of the frequency of updating track geometry on differential settlement. Three cases are simulated: updating it after every axle passage, updating after every 10 passages, and also after every 100 passages. The characteristics of the rails, rail pads, sleepers, ballast, sub-ballast and subgrade are described in Table 5.1. Two different subgrades are chosen to represent a stiff and soft soil. The vehicle is a passenger train travelling at 201 km/h.

To understand how frequently the track geometry profile requires updating between load passage simulations, the two subgrade cases are subject to 100,000 axle loads. The simulations are performed with three different values of: dN=1, 10 and 100. This means the track irregularity profile, train-track dynamic interaction forces, and deviatoric stresses are updated every 1, 10, and 100 load passages until the total number of passages is reached. In practical terms, considering an initial track geometry, dN=100 means that all profile changes due to the next 100 axle loads are not explicitly modelled. Instead, after 100 cycles, the model attempts to update the profile considering the cumulative change due to the previous 100 cycles.

The number of loading applications after the last renewal of ballast and subgrade, N_{lb} and N_{ls}, are equal to zero, representing the case of newly constructed track that has only experienced minimal traffic loading. Both subgrade soils are silty sand, with material parameters (a, m, b) given in Table 3.6.

The initial track irregularity profile is artificially generated using the PSD function defined by FRA, considering 40 frequencies, and is shown in Figure 5.3. In order to represent a new track, constructed to tight tolerances and prior to significant train loading, the value of parameter A is set as 0.29×10^{-8} m^2-rad/m.

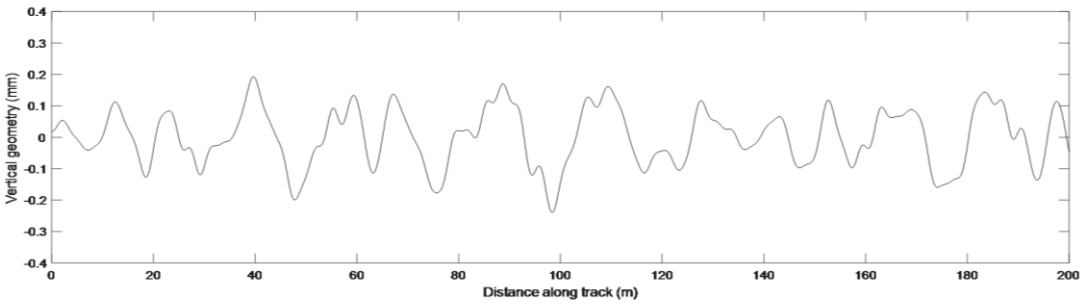

Figure 5.3 Initial track irregularity profile

Considering Soil case 1 (high stiffness soil), Figure 5.4(a) shows the change in geometry standard deviation versus load cycles, for dN=1, dN=10, and dN=100. After 100k cycles, it is seen that dN = 1 results in the highest standard deviation, while dN=100 results in the track geometry with lowest standard deviation. The discrepancy between using dN=10 rather than dN=1 is 2.17%, while the discrepancy between using dN=100 rather than dN=1 is 3.62%.

Similar findings are true for Soil case 2 (lower stiffness soil), however the effect is more pronounced, as shown in Figure 5.4(b). dN=1 results in the highest

standard deviation, while dN=100 results in the lowest. The discrepancy between using dN=10 rather than dN=1 is 32.07%, while the discrepancy between using dN=100 rather than dN=1 is 65.43%.

These findings indicate that it is important to update the track geometry profile as frequently as possible, and ideally after every load passage. Although this implies increased computational effort, if not adhered to, then the full effect of train-track interaction on differential settlement is not captured. This is particularly true for softer soils where the effect is amplified.

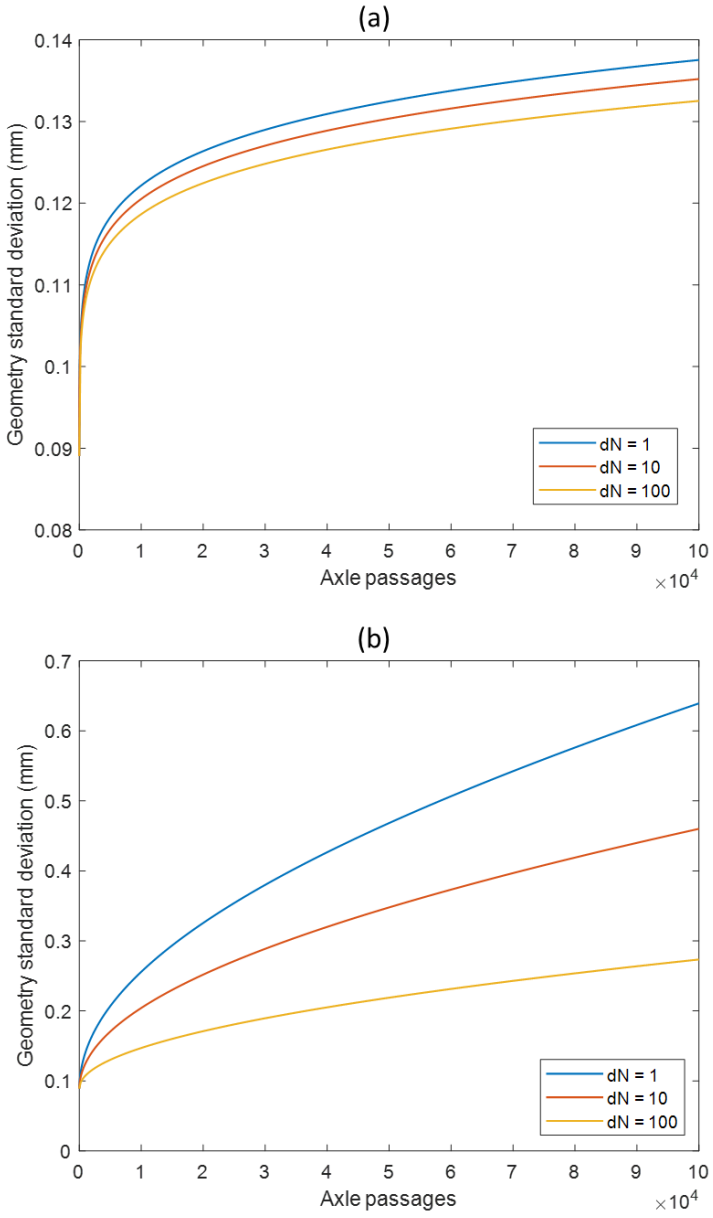

Figure 5.4 Track geometry evolution versus profile update frequency: (a) high stiffness subgrade; (b) low stiffness subgrade

5.4 Discussion

The validated model is used to investigate the influence of updating the track geometry after each axle load on the differential settlement prediction. This confirms the importance of updating the track geometry profile as frequently as possible, particularly for softer soils. However, the frequency of updates also relies on the sensitivities of the case studies and computational resources available. It may be prudent to consider increasing the update frequency (dN) to decrease runtime and computational demands, particularly for stiffer subgrades where sensitivity is lower compared to softer subgrades. In addition, the effect of changing the elastodynamic and settlement properties of the subgrade are investigated. It is shown that stiffer soils give rise to markedly reduced settlement, thus highlighting the need for well-constructed track subgrade.

Chapter 6
Analysis of concrete slab and ballasted track

6.1 Introduction

Slab track systems are commonly regarded as cost-effective if their initial cost does not exceed 30% of the cost of ballasted track systems (Tayabji and Bilow, 2001). Although slab tracks typically require the construction of more highly engineered earthworks, ballasted tracks can be more expensive to maintain due to the need for regular tamping to maintain track geometry within threshold tolerance.

In this chapter, the numerical model is used to compare the train-induced settlement behaviour of both ballasted and slab tracks. The model is used to study the differential settlement of both track structures at two train speeds: intercity (200 km/h) and high speed (300km/h).

6.2 Case studies

6.2.1 Track parameters

6.2.1.1 Ballasted track

The finite element mesh of the ballasted track case study is shown in Figure 6.1. The characteristics of the rails, rail pads, sleepers, ballast, sub-ballast, embankment and subgrade are described in Table 6.1. The track is assumed to be newly constructed using modern compaction techniques, with new, unfouled ballast that has been subject to dynamic track stabilisation.

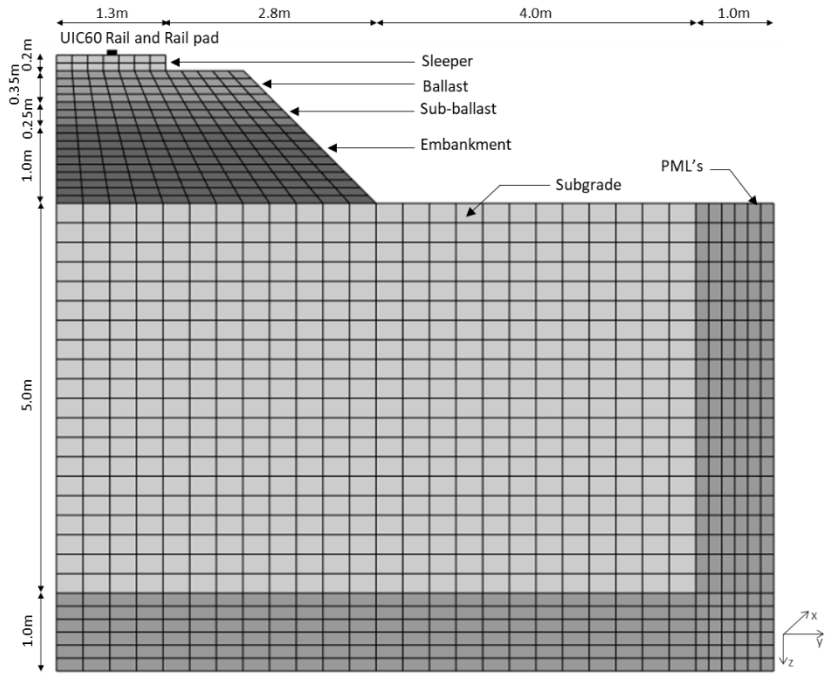

Figure 6.1 Finite element mesh of ballasted track

Table 6.1 Ballasted track properties

Component	Parameter	Value
UIC 60 Rail (single rail)	Height (m)	0.172
	Length in transversal direction (m)	0.015
	Section area (m^2)	7.677×10^{3}
	Moment of Inertia y-y (m^4)	3.038×10^{-5}
	Moment of Inertia z-z (m^4)	0.512×10^{-5}
	Young's modulus (MPa)	2.11×10^{5}
	Density (kg/m^3)	7850
	Poisson's ratio	0.3
	Hysteretic damping coefficient	0.01
Railpad (spring element)	Continuous stiffness (N/m^2)	200×10^{6}
	Viscous damping (Ns/m^2)	22.5×10^{3}
Sleeper (G44)	Height (m)	0.2
	Length in transversal direction (m)	2.5
	Sleeper spacing (m)	0.65
	Young's modulus (MPa)	3×10^{4}
	Density (kg/m^3)	2500
	Poisson's ratio	0.2
	Hysteretic damping coefficient	0.01
Ballast	Height (m)	0.35

Component	Parameter	Value
	Length in transversal direction (m)	2.8
	Young's modulus (MPa)	220
	Density (kg/m^3)	1600
	Poisson's ratio	0.12
	Hysteretic damping coefficient	0.06
Sub-ballast (Sand gravel)	Height (m)	0.25
	Length in transversal direction (m)	3.5
	Young's modulus (MPa)	210
	Density (kg/m^3)	2000
	Poisson's ratio	0.3
	Hysteretic damping coefficient	0.05
	Settlement parameter a	0.52
	Settlement parameter b	0.15
	Settlement parameter m	1.49
	Compressive strength (kPa)	350
Embankment (Sand gravel)	Height (m)	1.0
	Young's modulus (MPa)	200
	Density (kg/m^3)	2000
	Poisson's ratio	0.3
	Hysteretic damping coefficient	0.05
	Shear wave speed (km/h)	706
	Settlement parameter a	0.52
	Settlement parameter b	0.15
	Settlement parameter m	1.49
	Compressive strength (kPa)	320
Subgrade (Silt)	Young's modulus (MPa)	100
	Density (kg/m^3)	2000
	Poisson's ratio	0.35
	Hysteretic damping coefficient	0.03
	Shear wave speed (km/h)	547
	Settlement parameter a	0.64
	Settlement parameter b	0.1
	Settlement parameter m	1.7
	Compressive strength (kPa)	240

6.2.1.2 Slab track

The finite element mesh of slab track is shown in Figure 6.2. The rails, rail pads, embankment and subgrade have the same characteristics as those in the ballasted track, whereas the characteristics of slab and HBL (hydraulically bound layer) are described in Table 6.2.

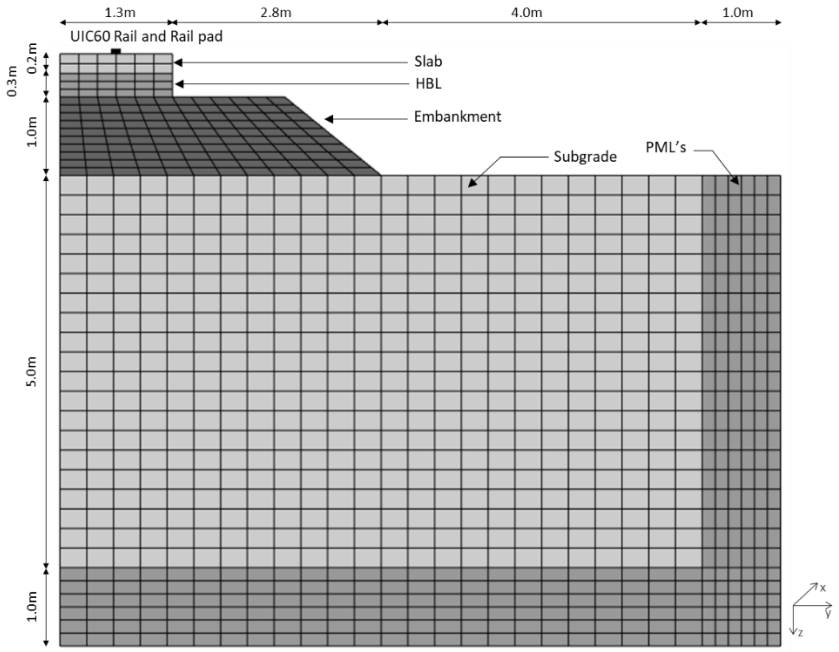

Figure 6.2 Finite element mesh of slab track

Table 6.2 Slab track properties

Component	Parameter	value
Slab	Height (m)	0.25
	Length in transversal direction (m)	2.6
	Young's modulus (MPa)	$3x10^4$
	Density (kg/m^3)	2500
	Poisson's ratio	0.2
	Hysteretic damping coefficient	0.001
HBL	Height (m)	0.3
	Length in transversal direction (m)	2.6
	Young's modulus (MPa)	$10x10^3$
	Density (kg/m^3)	2500
	Poisson's ratio	0.2
	Hysteretic damping coefficient	0.03

6.2.2 Track geometry profile and traffic parameters

The initial track irregularity profile for both tracks is artificially generated using the PSD function, considering 40 frequencies. The values of parameters A, k_2 and k_3 are set as 0.053x10^{-6} m^2·rad/m, 14.639x10^{-2}rad/m and 82.474x10^{-2}rad/m, resulting in a track geometry profile with a starting standard deviation (SD) of 0.4mm. The rolling stock is an 8-car ICE with 2 traction cars and 6 central cars, equating to 32 axles per train. Considering the traffic volume in terms of milling gross tons (MGT), a single ICE train is equal to 0.0005MGT. Therefore, the traffic volume of 1MGT is equivalent to 2000 train passages, or 64k axle passages.

6.3 Track deflection time histories

Considering the full ICE train with both quasi-static and dynamic excitation (described in Chapter 3), Figure 6.3 compares elastic track deflection time histories for ballasted and slab tracks. Figure 6.3(a) and (b) compare elastic track deflection time histories of the ballasted track at moving speeds of 200 and 300km/h. It is seen that the higher speed induces larger elastic deflection. Similar trend is also visible with the slab track when increasing moving speed as shown in Figure 6.3(c) and (d). Comparing the ballasted track and slab track subject to the same moving speeds, the elastic deflections in the ballasted track are marginally higher than in slab track. This is true at both 200 and 300km/h.

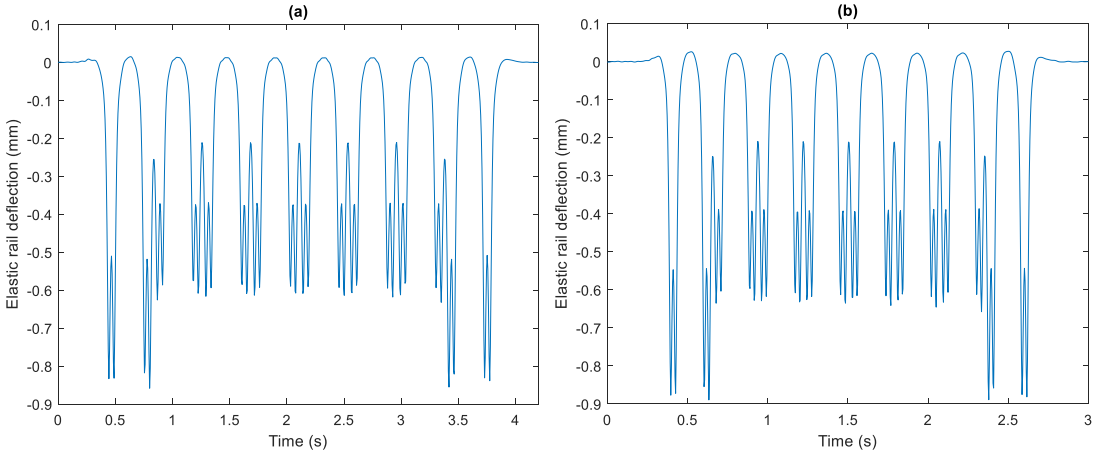

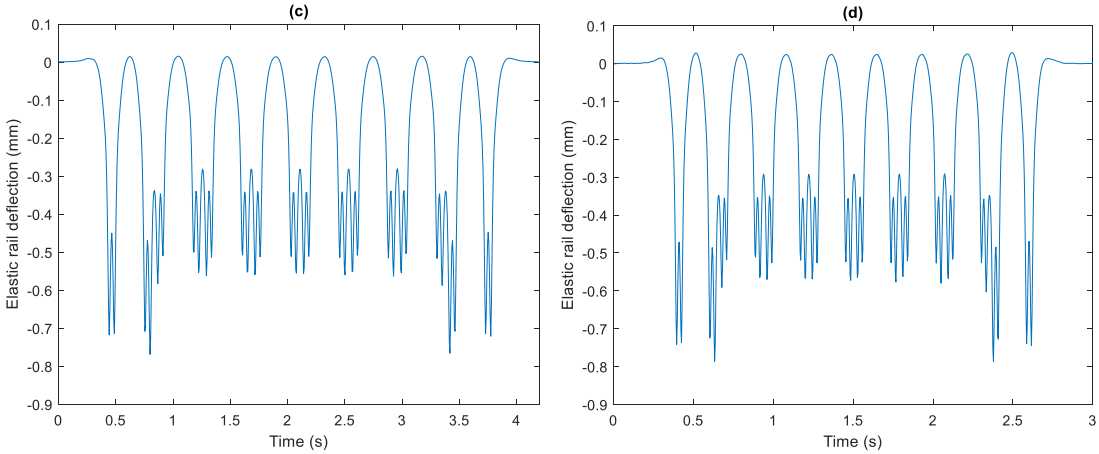

Figure 6.3 Track deflection time histories considering both quasi-static and dynamic excitation: (a) Ballasted track-200km/h (b) Ballasted track-300km/h (c) Slab track-200km/h (d) Slab track-300km/h

Figure 6.4(a) and (b) illustrate the 3D track-ground displacement contours for ballasted and slab tracks at 300km/h and the response propagating from the rail into supporting track-ground structure. Note that although the domain shown is the full 200m track section with a 184.9m long train, to maximise viewability, the x-axis is scaled by a factor of 8 compared to the y and z-axis.

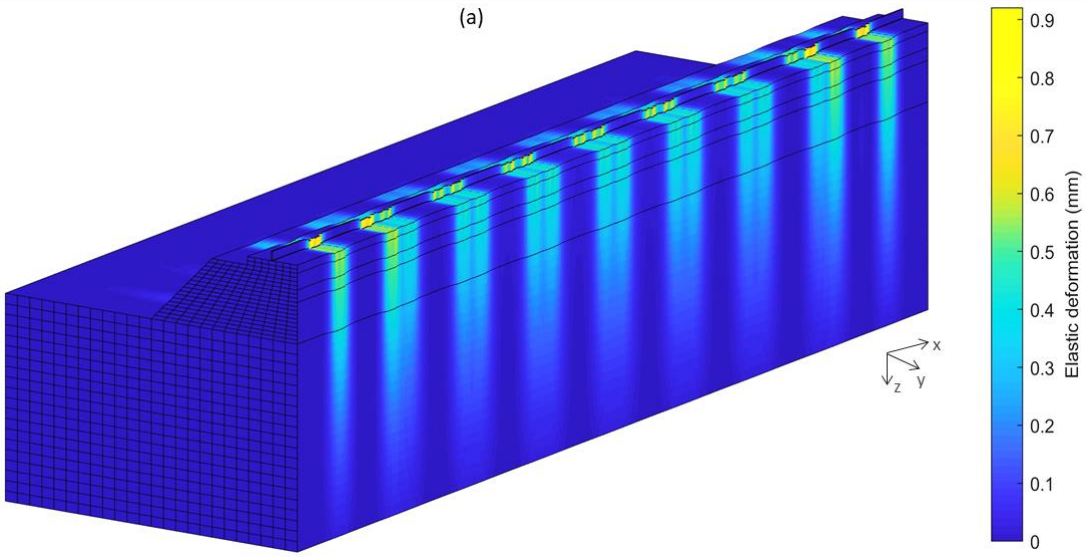

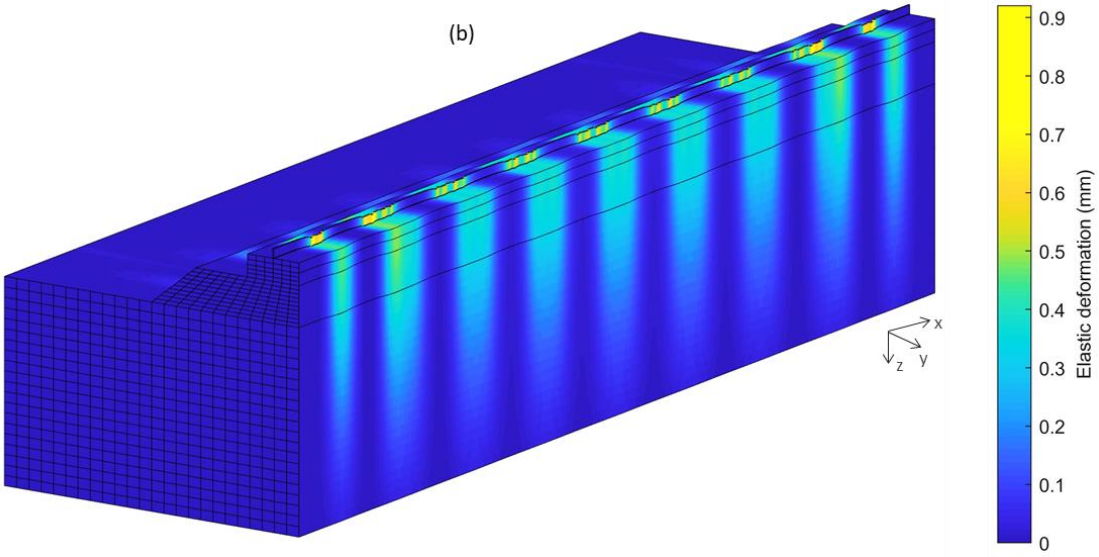

Figure 6.4 3D track-ground deflection profile (slice along track centreline considering both quasi-static and dynamic excitation): (a) ballasted track (b) slab track

6.4 Early life settlement

To investigate early life settlement, the differential settlement evolution over 100k axle passages is shown in Figure 6.5. Figure 6.5(a) and (b) show the vertical track geometry profiles of both ballasted and slab tacks at the instant they reach 100k load cycles for the speeds of 200 and 300km/h, respectively.

Figure 6.6 compares the evolution of geometry SD over number of load cycles from the initial SD value until 100k load passages for four cases: ballasted track at speed of 200km/h, ballasted track at speed of 300km/h, slab track at speed of 200km/h and, slab track at speed of 300km/h. The corresponding SD at 100k axle passages are summarised in Table 6.3. At a speed of 200km/h, the SD of ballasted and slab tracks are 0.463mm and 0.430mm, respectively. This corresponds to a 7.13% decrease for the slab track. At speed of 300km/h, the SD of ballasted and slab tracks increases to 0.471mm and 0.431mm, respectively, corresponding to a marginally higher 8.49% decrease.

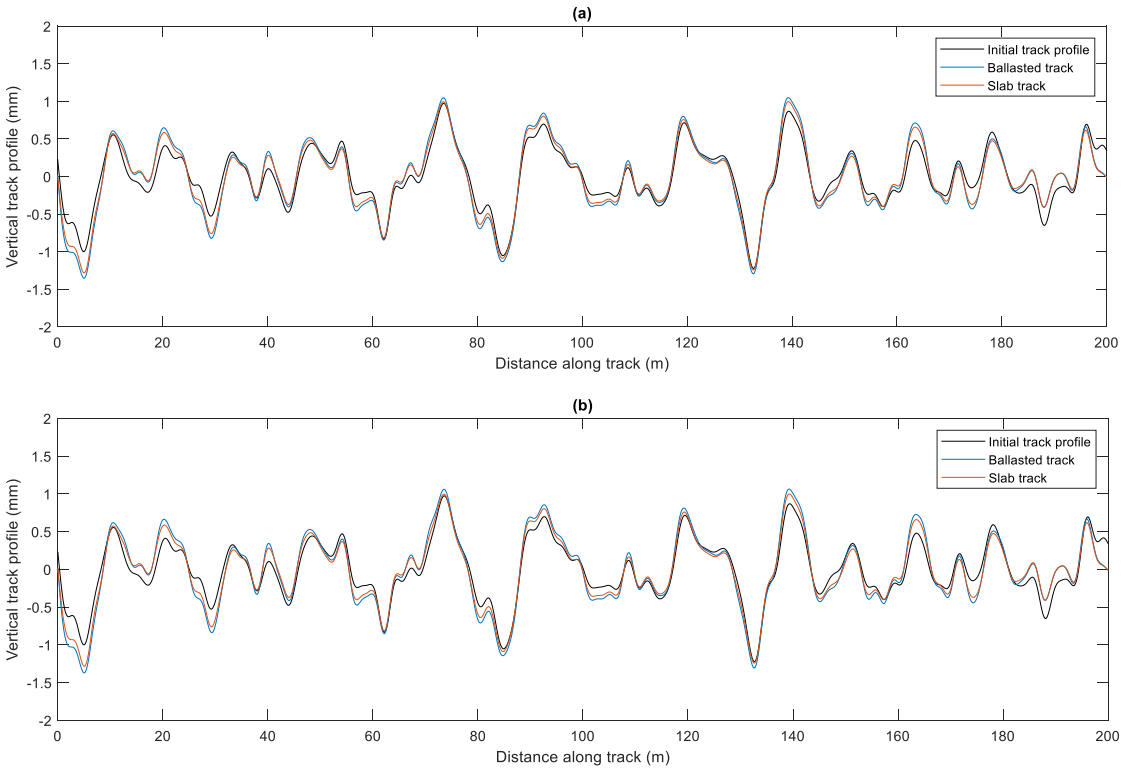

Figure 6.5 Vertical track profiles after 100k axle passages for ballasted track and slab track: (a) 200km/h (b) 300km/h

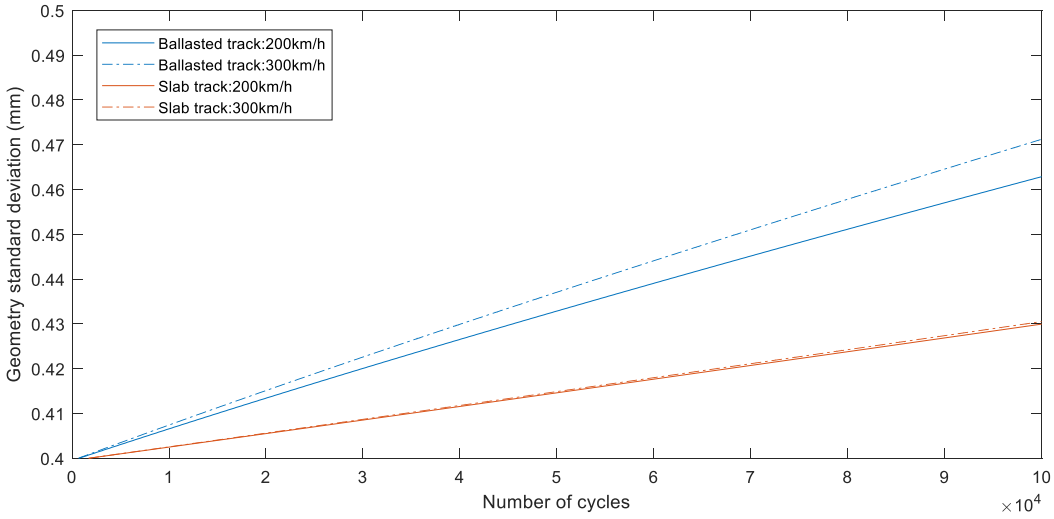

Figure 6.6 Geometry SD curves over 100k load passages for ballasted track and slab track

Table 6.3 Geometry SD after 100k axle passages for ballasted track and slab track

Speed (km/h)	Track type	SD after 100k axle passages (mm)	Percentage decrease
200	Ballasted track	0.463	7.13%
	Slab track	0.430	
300	Ballasted track	0.471	8.49%
	Slab track	0.431	

6.5 Settlement after 30MGT of traffic

To simulate differential settlement evolution over a longer-term, both ballasted and slab tracks are now subjected to 30MGT traffic. Figure 6.7(a) and (b) show the vertical track geometry profiles of both ballasted and slab tacks at the moment of reaching 30MGT for the speeds of 200 and 300km/h, respectively.

Figure 6.8 compares the evolution in geometry SD with MGT from the initial 0.4mm SD value for ballasted and slab tracks, considering both moving speeds. The results are summarised in Table 6.4. The SD of ballasted and slab tracks at 200km/h are 1.272mm and 0.989mm, respectively, which correspond to a 22.25% decrease. At a moving speed of 300km/h, the SD of ballasted and slab tracks increases to 1.525mm and 1.008mm, respectively, corresponding to a 33.90% decrease. Note that at the maximum operational linespeed of 300km/h, the SD threshold limit for ballasted track tamping maintenance is approximately 1.5mm (Whitehead et al., 2021). Therefore the ballasted track at 300km/h linespeed requires tamping prior to 30MGT, while the 200km/h ballast track does not.

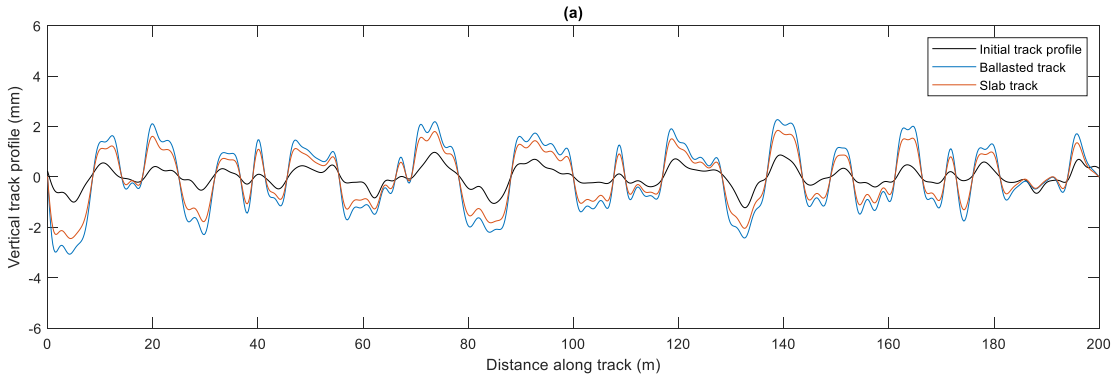

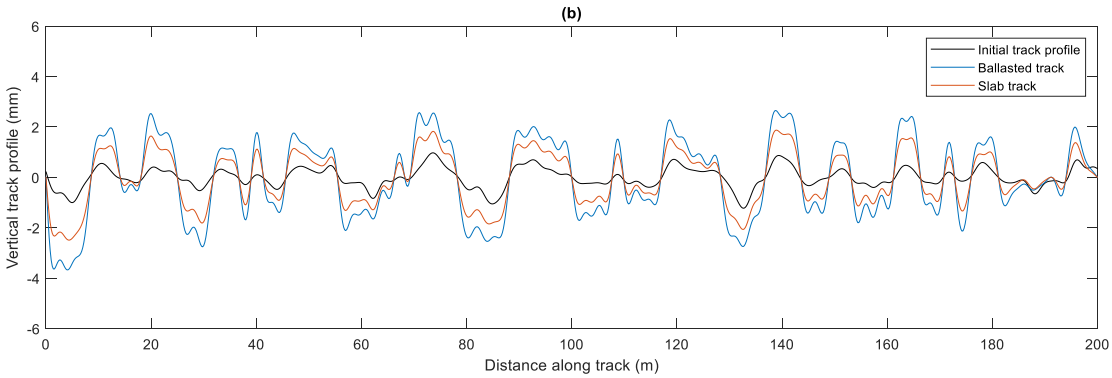

Figure 6.7 Vertical track profiles after 30MGT traffic for ballasted track and slab track: (a) 200km/h (b) 300km/h

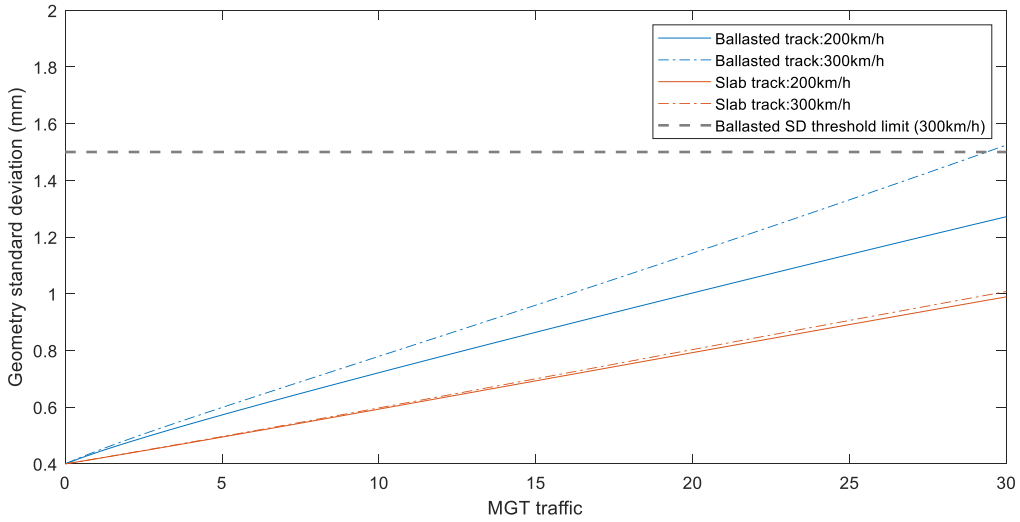

Figure 6.8 Geometry SD curves over 30MGT traffic for ballasted track and slab track

Table 6.4 Geometry SD after 30MGT traffic for ballasted track and slab track

Speed (km/h)	Track type	SD after 30MGT traffic (mm)	Percentage difference
200	Ballasted track	1.272	22.25%
	Slab track	0.989	
300	Ballasted track	1.525	33.90%
	Slab track	1.008	

6.6 Deviatoric stresses within track-bed and subgrade layers

Deviatoric stress is one of the most influential parameters on settlement. Therefore the contribution of deviatoric stresses along the depths of the track-bed and subgrade layers are investigated. The definition of track-bed layers in this work is ballast, subballast and embankment for the ballasted track, and only the embankment for the slab track. The deviatoric stresses due to the vehicle's quasi-static and dynamic loading components are compared. The quantities are calculated at the track centreline considering an ICE central car and selecting the mean deviatoric stresses over the track length.

Considering track-bed layers, the contribution of deviatoric stresses within the ballasted track are shown in Figure 6.9(a) considering quasi-static excitation and Figure 6.9(b) considering dynamic excitation. Similar to the ballasted track, the contribution of deviatoric stresses due to the quasi-static and dynamic excitations within the embankment for the slab track are shown in Figure 6.10(a) and (b), respectively. Considering the subgrade layer of both ballasted and slab tracks, the quasi-static and dynamic deviatoric stresses are shown in Figure 6.11(a) and (b), respectively.

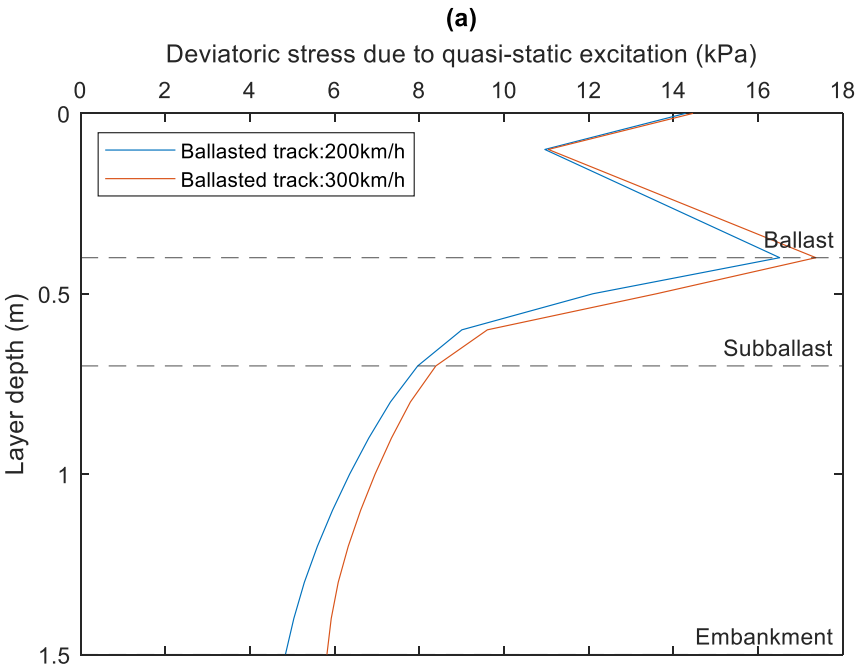

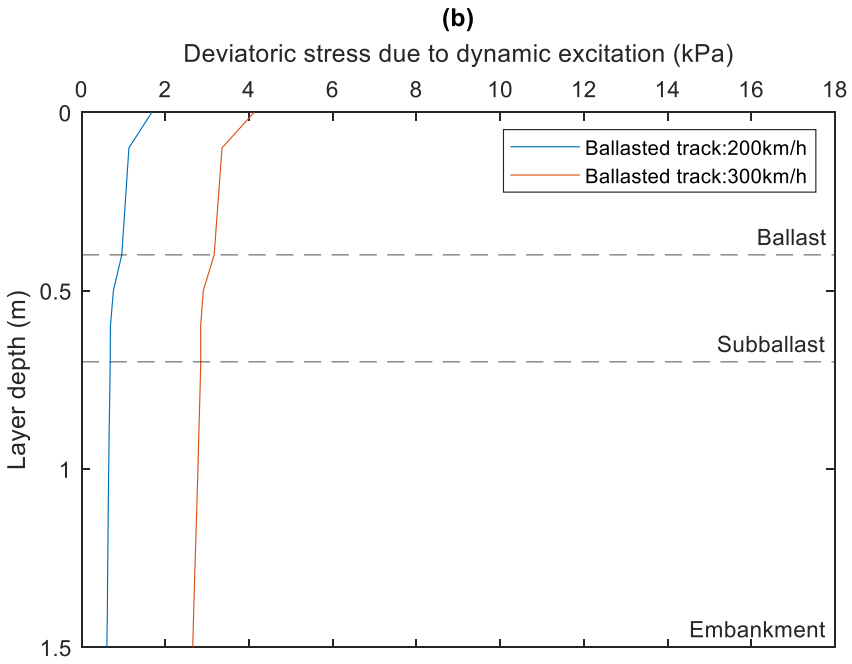

Figure 6.9 Deviatoric stresses within the track-bed of ballasted track: (a) quasi-static excitation (b) dynamic excitation

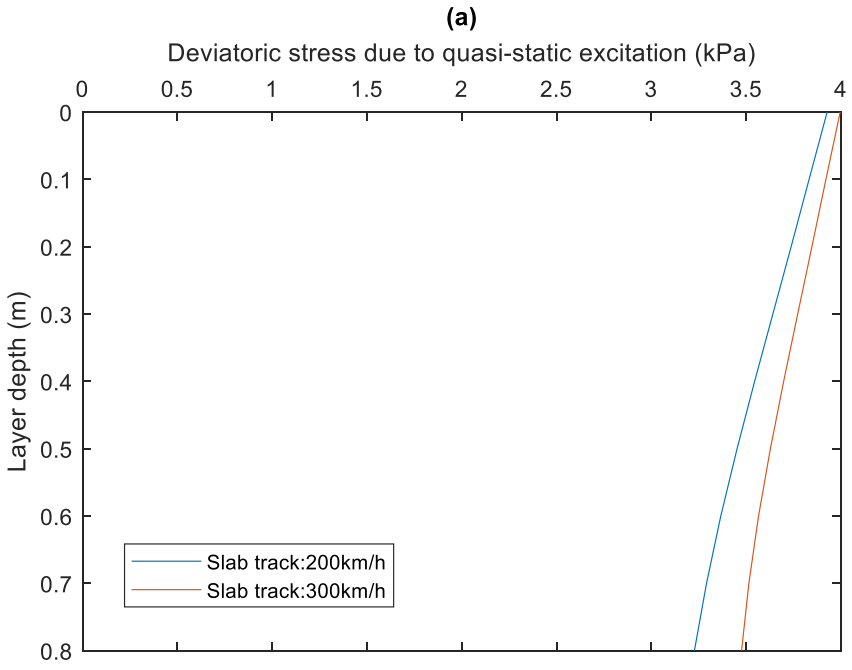

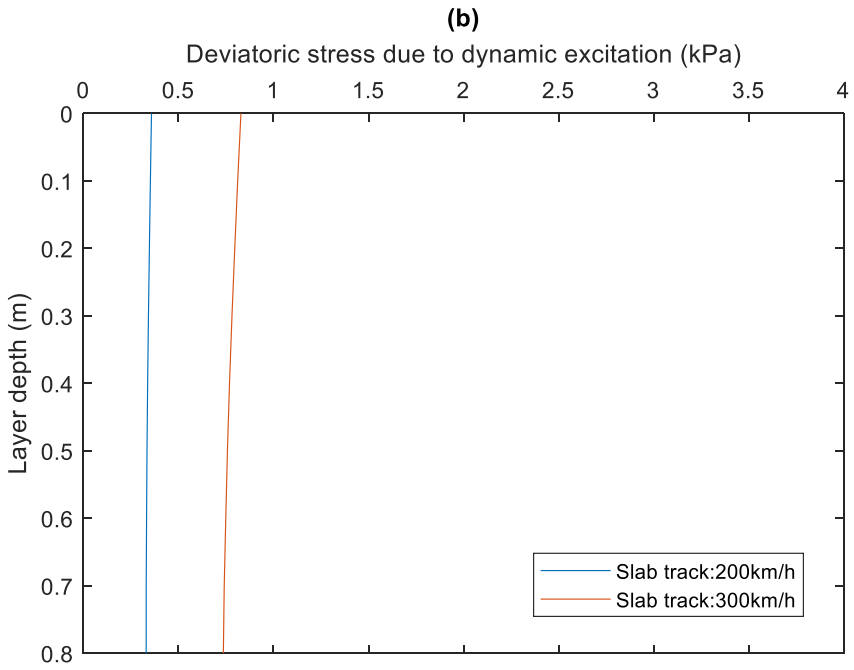

Figure 6.10 Deviatoric stresses within the track-bed of slab track: (a) quasi-static excitation (b) dynamic excitation

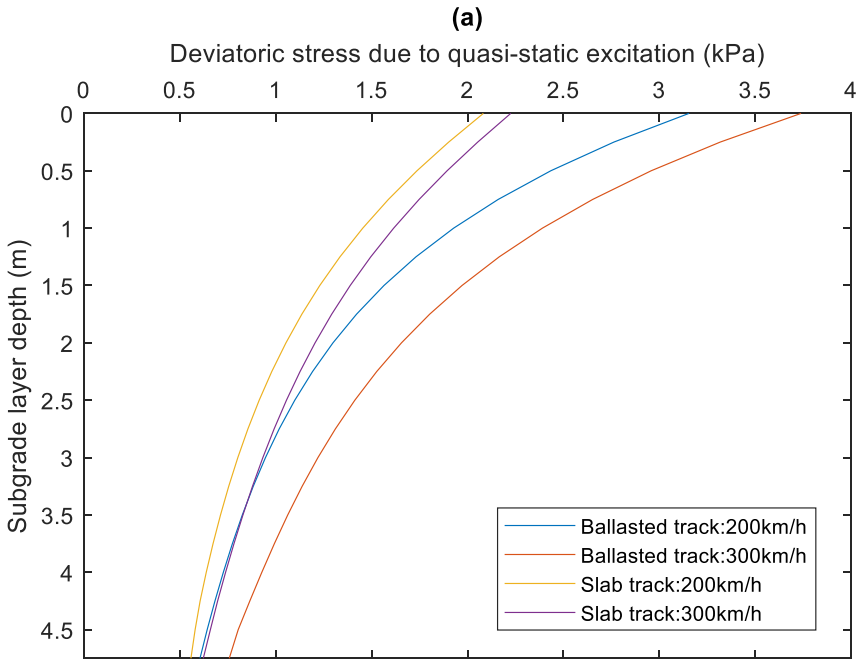

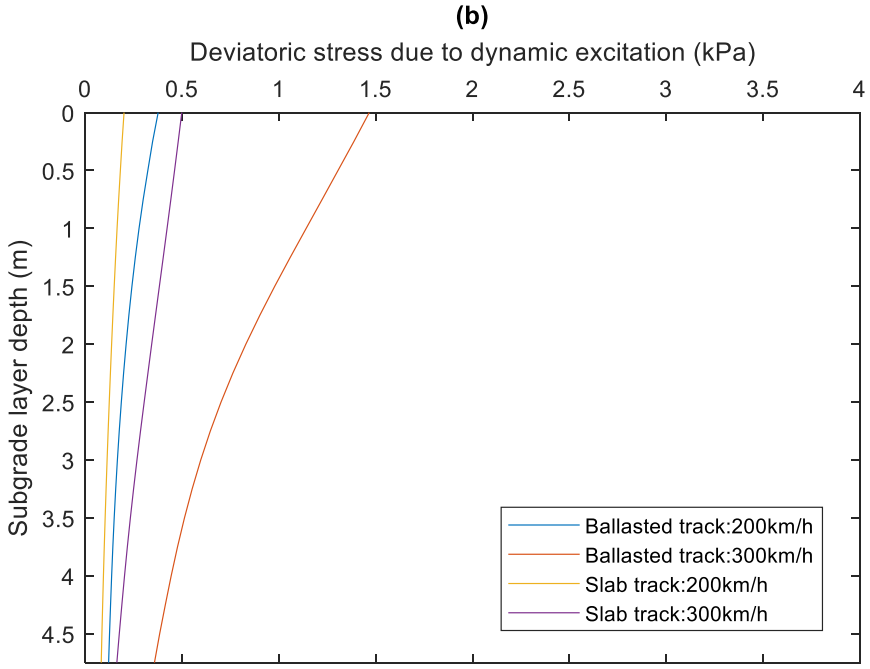

Figure 6.11 Deviatoric stresses within the subgrade layer: (a) quasi-static excitation (b) dynamic excitation

It is seen in Figure 6.9(a), Figure 6.10(a) and Figure 6.11(a) that the quasi-static deviatoric stresses in both the ballasted and slab track increase with moving speed, however the ballasted track yields marginally higher deviatoric stresses than the slab track. The lower stresses in the slab track are mainly due to the HBL which is stiffer compared to the ballast and sub-ballast. Considering the dynamic excitation, it is shown in Figure 6.9(b), Figure 6.10(b) and Figure 6.11(b) that an increase in moving speed induces significantly higher deviatoric stresses, particularly within the ballasted track. Unlike the quasi-static excitation, the deviatoric stresses due to the dynamic excitation slightly decrease with depth in all the track layers, particularly at lower speed. These increases in both quasi-static and dynamic deviatoric stresses with speed contribute towards larger permanent deformation and thus differential settlement.

Figure 6.12(a) and (b) show the cumulative permanent strains over 90MGT traffic for both ballasted and slab tracks. These responses are calculated using the mean deviatoric stresses measured at the top of each layer. However, the iterative process updates the track geometry profile from the settlements calculated every 0.2m along track length (in the train passage direction) and at vertical depth intervals of 0.25m. Comparing the cumulative permanent strains in the track and subgrade layers, it is seen that they are lowest in the subgrade layer for both ballasted track and slab track. This is because the settlement

primarily occurs in the track-bed layers. For the ballasted track this is because the scope for particle rearrangement is greatest within the ballast matrix. Further, comparing the ballasted track and slab track, the cumulative permanent strains in the ballasted track are higher than the slab track, particularly at high moving speed. This is because the bending stiffness of the slab results in a more uniform distribution of stresses into the supporting earthworks. This is corroborated in Figure 6.11(b), where the deviatoric stresses decrease almost linearly with depth below the slab, but non-linearly below the ballasted track. Note that the y-axis in Figure 6.12(b) is scaled 6x larger than in Figure 6.12(a) for improved viewability.

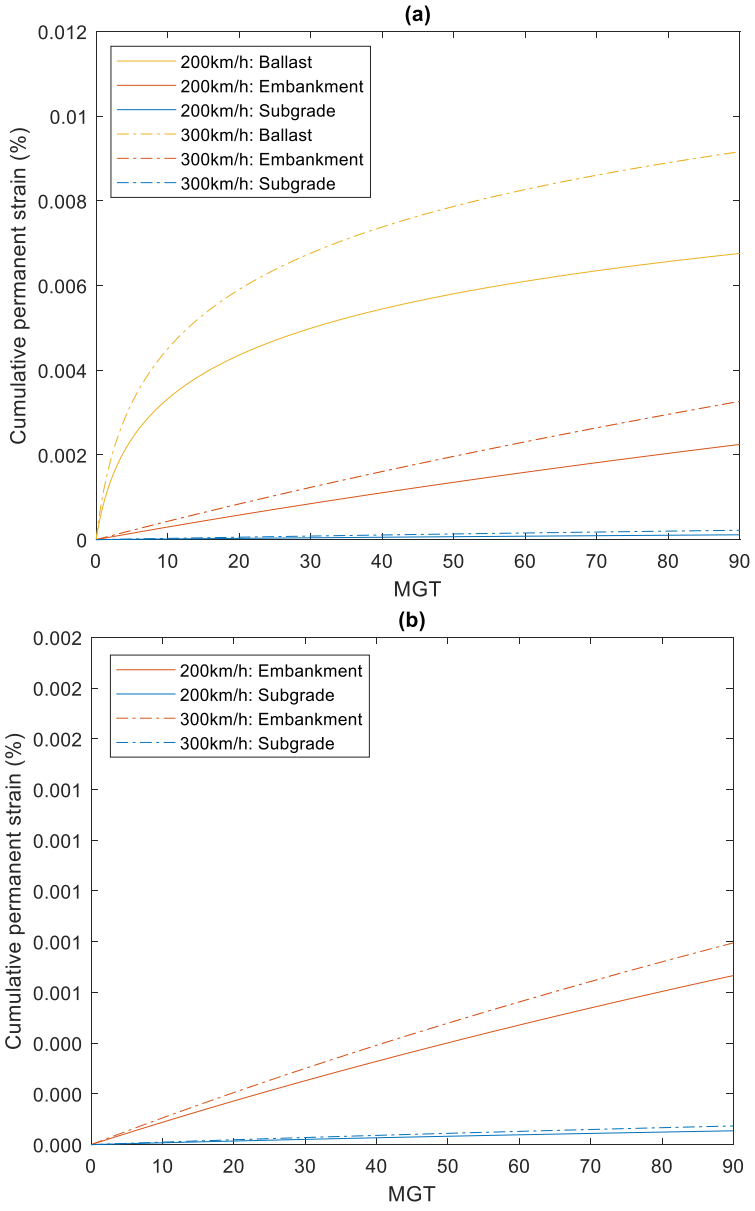

Figure 6.12 Cumulative permanent strains: (a) ballasted track (b) slab track

6.7 Discussion

The numerical results show the rate of geometry degradation is more rapid for ballasted tracks compared to concrete slabs. This is true for speeds of 200 and 300km/h, however the ballasted track shows more rapid degradation at higher speed. This is because the elevated stress fields propagating within the unbound ballast trackbed can induce significant particle rearrangement. In contrast, the stress fields propagating in the slab track induce negligible plastic deformation within the concrete. Therefore ballasted track permanent settlement is a combination of ballast, embankment and subgrade deformation, whereas the concrete slab track settlement is due to the embankment and subgrade deformation. Note however that this study is focused on differential settlements induced solely due to train loading and ignores other sources of long-term earthwork settlements (e.g. consolidation, creep and shrink-swelling). Slab track rail fasteners can be adjusted typically between +26mm and –4mm to restore track geometry. However, this range relates to the total settlement, meaning the train loading induced differential and uniform settlement must also be considered in conjunction with all additional sources of settlement (e.g. earthworks related settlement).

Further, in reality a range of concrete slab track products exist, including precast and those poured in-situ. The 2.5D modelling procedure used in this paper assumes the concrete slab track is infinitely long and is in absence of expansion joints. Therefore it does not account for the additional plastic settlement induced by movements in the vicinity of these joints. Thus, the results are more representative of slab track systems with larger spacing between joints. To study the effect of such discontinuities a 3D model should be considered.

To allow a fair comparison, the analysis has assumed that the track structure and track geometry is the same for both slab and ballasted tracks regardless of linespeed. In reality however, ballasted tracks have less onerous earthworks requirements meaning their formation may be less stiff compared to a slab track constructed at the same site. Similar is true when comparing the lower and higher speed track scenarios. Regarding track geometry, at higher speeds the ballasted track geometry is likely to be maintained to a tighter tolerance compared to the low speed. Further, concrete slab tracks are likely to exhibit a lower standard deviation in track geometry post-construction due to higher precision construction methods.

Chapter 7
Analysis of ballast fouling and moisture of fines

7.1 Introduction

During initial construction and routine maintenance procedures, fresh ballast containing clean, uniformly graded coarse aggregate is incorporated into the track substructure. However, over time, the ballast deteriorates and/or becomes contaminated due to usage and traffic accumulation. This degradation is primarily due to aggregate breakage and reduction in particle size, occasionally caused by mud pumping and external contamination, all referred to as fouling. Ballast fouling can result in track geometry issues, frequently originating from inadequacies in ballast performance, such as inadequate drainage, rapid and excessive substructure settling, and diminished lateral track stability.

One crucial role of the ballast is to facilitate effective drainage. However, as it becomes fouled, it loses its ability to free-drain. Over the past few decades, extensive research has been conducted to explore the performance of unbound aggregate materials under various moisture conditions. Even in the case of clean aggregate materials, moisture can introduce lubrication between particle contacts, resulting in heightened deformation and reduced strength (Thom and Brown, 1987). This effect becomes more pronounced as the moisture of fines (w) rises, particularly as it approaches saturation (Lekarp et al., 2000).

Railway engineers play a vital role in monitoring and investigating the gradual deterioration of in-service ballast over its operational lifespan. This involves assessing the characteristics of degraded ballast to ascertain whether it can continue to fulfil its roles in providing structural support and efficient drainage for maintaining appropriate track geometry and stability. In this context, (Selig and Waters, 1994) proposed the use of a Fouling Index (FI), which is calculated as the sum of the percentage by weight of ballast sample passing the 4.75 mm (No. 4) sieve and the percentage passing the 0.075 mm (No. 200) sieve. This index serves to quantify ballast fouling conditions and estimate the drainage performance of wet fouled ballast.

In this chapter, a novel equation for ballast settlement is presented, derived from laboratory data concerning degraded ballast subjected to both dry and wet conditions (Charoenwong et al., 2024). Four different case studies are examined. The first case investigates the impact of Fouling Index (FI) under dry

subgrade conditions, with FI values ranging from 5 to 40. The second case studies the influence of moisture of fines on fouled ballast, exploring moisture levels of 3%, 6%, and 9% (w) at a constant FI value of 40. The third case examines the effect of a reduced embankment stiffness considering different levels of ballast FI and moisture content. The final case assesses the effect of linespeed under various ballast conditions, considering speeds of 100, 150, and 200 km/h.

7.2 Fouled ballast settlement model

Large-scale triaxial tests were performed by (Qian et al., 2022) using the University of Illinois Triaxial Ballast Tester. The investigation aimed to assess the influence of moisture on the mechanical performance of degraded ballast. It focused on analysing permanent deformation and shear strength attributes under varying moisture conditions, encompassing both dry and wet scenarios. The ballast was varied at FI levels: 0, 10, 20, 30, and 40, while the moisture content of the finer particles was varied at: 3%, 6%, and 9%.

Based upon the test data, a model for ballast settlement is introduced, which takes into consideration both Ballast Fouling Index (FI) and moisture of fines (*w*). The new settlement equation is a modified version of that proposed by Li and Selig as shown in Eqs. (7-1) and (7-2) (Li et al., 2015). The coefficient A associated with plastic strain after the initial cycle of repeated loading is adapted to consider both ballast fouling and moisture. Additionally, it incorporates the ratio between the stress invariant quantity (*t*) and the Mohr–Coulomb failure criterion (t_{mc}) for a more universal/flexible approach that can be applied to all track layers. Considering the need to regularly update the track profile, the equation is also further refined to account for the settlement from previous axle passages in the build-up of plastic settlement, rather than simply consider the total number of cycles as is common in settlement modelling. This modification enables computation at each iterative step. This offers multiple benefits, for example being able to better capture the non-linearity of track settlement and greater flexibility in considering the rate of growth of track geometry (e.g. due to different magnitudes of axle loads (C. Charoenwong et al., 2022)). The computation of permanent strain can be formulated as Eq. (7-3), considering Eqs. (7-1) and (7-2):

$$\varepsilon_p = \bar{A}N^b \tag{7-1}$$

$$\bar{A} = \bar{a}\left(\frac{\sigma_d}{\sigma_s}\right)^m \quad \textbf{(7-2)}$$

where ε_p is the cumulative plastic strain (%); σ_d is the deviator stress; σ_s is the material static strength; $\bar{a}$, b and m are material constants for different soil types corresponding to clay content and soil plasticity as determined by (Li, 1994).

$$\Delta\varepsilon_{p\_b,i} = ((w+1)\cdot c) \times (FI \cdot d) \times \left(\frac{t}{t_{mc}}\right)^a \times \left[\left(((dN \cdot i) + N_{lb})^b - 1\right) - \left(\left((dN \cdot (i-1)) + N_{lb}\right)^b - 1\right)\right] \quad \textbf{(7-3)}$$

The corresponding settlement is then:

$$\Delta S_{b,i} = \sum_{j=1}^{k} \Delta\varepsilon_{p\_b,i_j} \cdot h_j \quad \textbf{(7-4)}$$

The term $\frac{t}{t_{mc}}$ defines the stress invariant quantity (t) and the Mohr–Coulomb failure criterion (t_{mc}) which can be calculated as follows:

$$t = \sqrt{2}\sqrt{J_2} \quad \textbf{(7-5)}$$

$$t_{mc} = \frac{\sqrt{2}\sin\emptyset' s' + \sqrt{6}\cos\emptyset' c'}{\sin\theta\sin\emptyset' + \sqrt{3}\cos\theta} \quad \textbf{(7-6)}$$

θ is the lode angle, defined as:

$$\theta = -\frac{1}{3}\sin^{-1}\left[\frac{3\sqrt{3}}{2}\left(\frac{J_3}{J_2^{3/2}}\right)\right] \quad \textbf{(7-7)}$$

$J_2$and J_3 are the 2nd and the 3rd invariant of deviatoric stress, defined as:

$$J_2 = \frac{1}{6}[(\sigma_1' - \sigma_2')^2 + (\sigma_2' - \sigma_3')^2 + (\sigma_3' - \sigma_1')^2] \quad \textbf{(7-8)}$$

$$J_3 = (\sigma_1' - \sigma_m')(\sigma_2' - \sigma_m')(\sigma_3' - \sigma_m') \quad \textbf{(7-9)}$$

s' is the stress invariant quantity, defined as:

$$s' = \sqrt{3}\,\sigma'_m \quad \textbf{(7-10)}$$

σ'_m is the mean effective stress, defined as:

$$\sigma'_m = \frac{(\sigma'_1 + \sigma'_2 + \sigma'_3)}{3} \quad \textbf{(7-11)}$$

where $\Delta\varepsilon_{p\_b,i}$ is the ballast permanent strain increment; i is the iterative step; N_{lb} is the number of load cycles after the last ballast renewal/tamping; $\Delta S_{b,i}$ is the ballast settlement increment; h_j is the thickness of each layer; k is the number of sublayers; dN is the frequency of load application; FI is the ballast fouling index (%) where $FI \geq 5$ & $FI \leq 40$; w is the moisture of fines (%) where $w \leq 9$; $\emptyset'$ is friction angle; $c'$is cohesion; $\sigma_1{}'$, $\sigma_2{}'$, $\sigma_3{}'$ are the principal effective stresses; and a, b, c, d are empirical constants.

The model was fitted to the test data, as illustrated in Figure 7.1 for ballast fouling index and Figure 7.2 for moisture of fines. The empirical constants, represented as a, b, c and d, are: 2.15, 0.38, 0.013, and 0.0042, respectively. The proposed equation exhibits a good fit with the experimental data. However, it is important to acknowledge that the lowest value of FI employed in the proposed model is FI = 5, even though it originates from test data with FI = 0. This adjustment is necessary since it is challenging to substantiate the assumption that fresh ballast has a FI value of 0 in real-world scenarios.

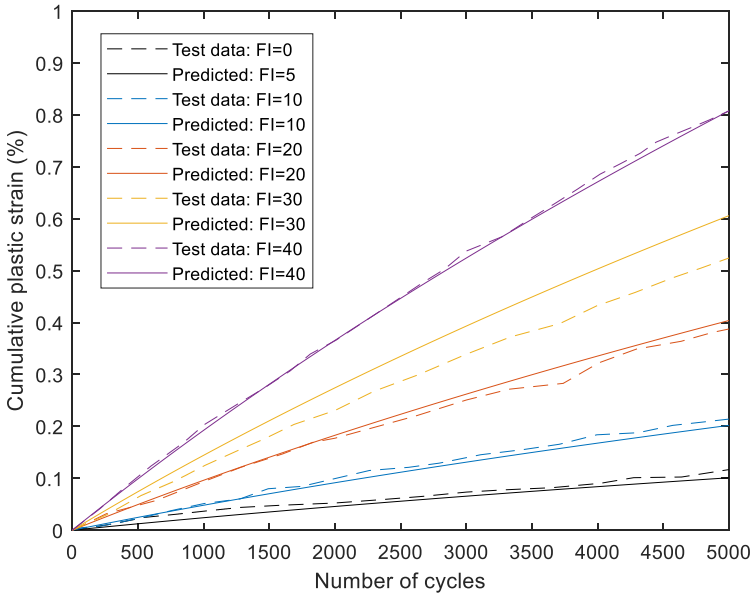

Figure 7.1 Comparison of proposed ballast settlement model with experimental data with ballast fouling indices varied from 0 to 40

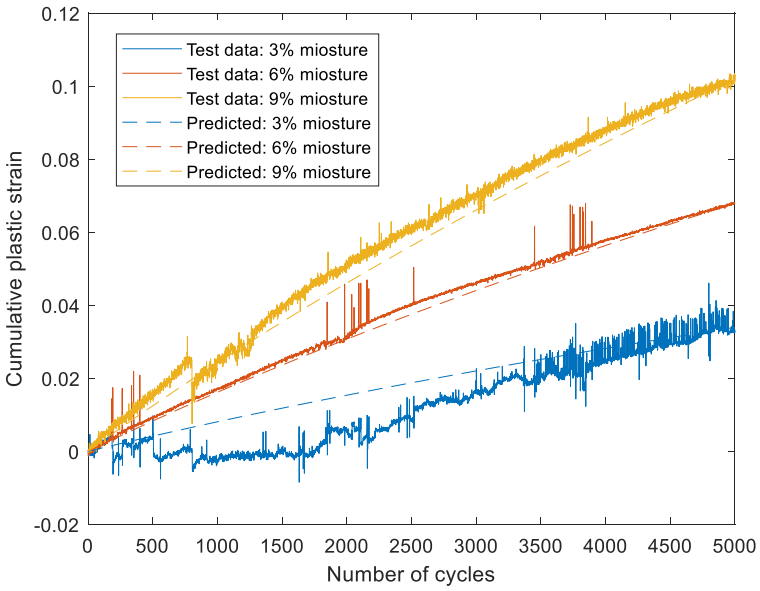

Figure 7.2 Comparison of proposed ballast settlement model with experimental data with moisture of fines 3, 6 and 9%

7.3 Case studies

The model is used to perform four analyses. Firstly it is used to analyse the effect of ballast fouling on differential track settlement under dry subgrade conditions. Secondly, it is used to investigate the effect of differing levels of moisture of fines within heavily fouled ballast. Thirdly, it is used to examines the effect of a reduced embankment stiffness considering different levels of ballast

FI and moisture content. Finally, it is used to assesses the effect of linespeed under various ballast conditions, considering different speeds.

7.3.1 Track parameters

The finite element track mesh remains consistent with the ballasted track case, shown in Figure 6.1. The track parameters including the characteristics of the rails, rail pads, sleepers, ballast and sub-ballast also remain consistent and presented in Table 6.1. The subgrade properties are shown in Table 7.1.

Table 7.1 Subgrade properties

Component	Parameter	Value
Subgrade (Sand/Silt)	Height (m)	5
	Young's modulus (Pa)	$70x10^6$
	Density (kg/m^3)	2000
	Poisson's ratio	0.35
	Hysteretic damping coefficient	0.03

7.3.2 Track geometry profile and traffic parameters

The initial track irregularity profile for both tracks is artificially generated using the PSD function (Federal Railroad Administration, 1980), considering 40 frequencies. The values of parameters A, k_2 and k_3 are set as 0.043×10^{-6} m^2·rad/m, 14.639×10^{-2}rad/m and 82.474×10^{-2}rad/m respectively, resulting in a track geometry profile with a starting standard deviation (SD) of 1.69mm. It is intended that the initial track geometry falls within a definition of good track quality, suitable for a linespeed of 200 km/h (Network Rail, 2015). For both cases, it is assumed that the ballast has previously been subject to either traffic or dynamic track stabilisation to reduce the rapid initial rearrangement of ballast particles. The rolling stock is an Alfa Pendular passenger train operating at a linespeed of 200 km/h and the traffic volume is 25 million gross tons (MGT) per year. In order to replicate the long-term evolution of differential settlement, both case studies are subject to 25MGT of traffic per year and simulated for a period of three years.

7.4 The effect of FI under dry subgrade conditions

Three dry scenarios are examined, involving variations of ballast FI from 5 to 40. These scenarios are defined as those with zero moisture of fines (0%). The assumed rate of fouling generation resulting from ballast deterioration is

0.025% per 1 MGT. Considering 3 years, the cumulative traffic is 75 MGT, representing an approximately 2% rise in FI. For instance, an initial FI of 5 at the commencement of the first year is expected to gradually escalate to 7 by the end of the third year.

Figure 7.3 compares the evolving geometry SD over time from the initial SD value in year 1 until year 3 for three different ranges of ballast FI. The corresponding SD after 3 years of traffic is summarised and compared in Table 7.2. The calculated SD after 3 years of traffic for initial FI values of 5, 15, and 30 are 1.703 mm, 1.717 mm, and 1.739 mm, respectively. These values demonstrate that the deterioration of track geometry is not linear but rather accelerates with increasing ballast fouling. Using FI = 5 as the baseline, the predicted SD for starting FIs of 15 and 30 increases by 0.014 mm and 0.037 mm, corresponding to an increase of 0.85% and 2.15%, respectively. It is seen that the greater the initial fouling, the more pronounced the impact on track geometry.

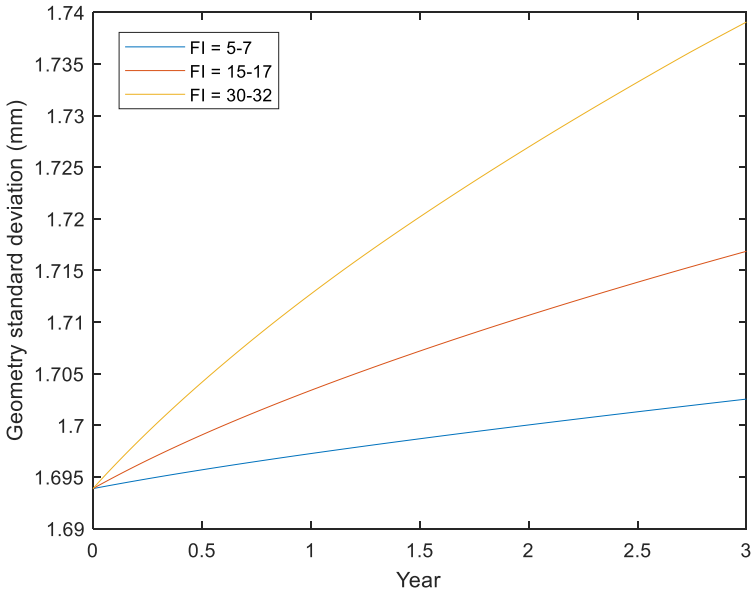

Figure 7.3 Standard deviation evolution over time for varying FI

Table 7.2 Predicted SD after 3 years of traffic for varying FI

FI from year 1 to year 3	SD after 3 years of traffic (mm)	SD increase (mm)	Percentage increase
5 –> 7	1.703	Baseline	0%
15 –> 17	1.717	0.014	0.85%
30 –> 32	1.739	0.037	2.15%

7.5 The effect of moisture of fines on fouled ballast

Continuing in a manner similar to the prior investigation, four scenarios are explored, but comparing varying levels of moisture of fines within heavily fouled ballast. The moisture content of fines considered are 0%, 3%, 6%, and 9%, with all scenarios being simulated at a constant ballast FI of 40.

Figure 7.4 illustrates the evolving SD over a period from year 1 to year 3 for four distinct moisture content levels. The corresponding SD's after 3 years of traffic are summarised and compared in Table 7.3. The calculated SD after 3 years of traffic for moisture contents of 0%, 3%, 6%, and 9% are 1.7528mm, 1.963mm, 2.238mm, and 2.570mm, respectively. The data clearly indicates that as the moisture content in the ballast increases, there is a significant escalation in the SD of track geometry. Using a moisture content of 0% as the baseline, the predicted SD moisture of fines 3%, 6%, and 9% is increased by 0.211mm, 0.485mm and 0.817mm, equating to 12.01%, 27.67%, and 46.61%. These substantial percentage escalations demonstrate a progressive deterioration in track geometry with increasing moisture levels.

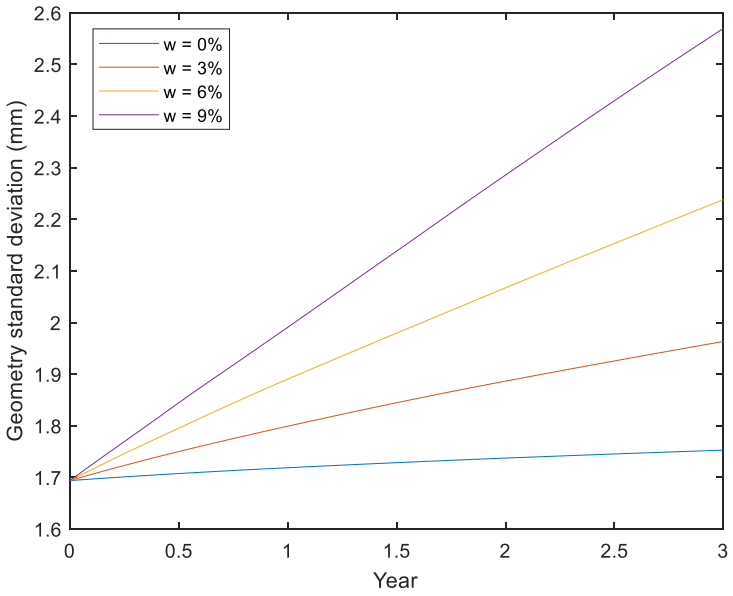

Figure 7.4 Standard deviation evolution over time for varying moisture contents

Table 7.3 Predicted SD after 3 years of traffic for varying moisture contents

Moisture of fines %	SD after 3 years of traffic (mm)	SD increase (mm)	Percentage increase
0	1.753	Baseline	0%
3	1.963	0.211	12.01%
6	2.238	0.485	27.67%
9	2.570	0.817	46.61%

7.6 The effect of embankment stiffness

This section extends the investigation into the effects of embankment stiffness on settlement, considering varying levels of fouled ballast. To do so, the Young's modulus of the embankment is reduced from the baseline value of 200 MPa to a stiffness value of 100 MPa.

Figures 7.5 and 7.6 illustrate the evolving SD over a period from year 1 to year 3 for three distinct FI and four distinct moisture content levels respectively. The corresponding SD's after 3 years of traffic are summarised and compared in Tables 7.4 and 7.5. Considering the low stiffness case, the predicted SD after 3 years of traffic for initial FI's of 5, 15, and 30 are 1.708mm, 1.731mm, and 1.767mm, corresponding to increases from the baseline case of 0.31%, 0.82%, and 1.62%, respectively. Similarly, for moisture contents of 0%, 3%, 6%, and 9%, the predicted SDs after three years are 1.790mm, 2.153mm, 2.647mm, and 3.248mm, corresponding to an increase from the baseline case of 2.13%, 9.63%, 18.26%, and 26.37%, respectively. These results reveal a clear trend: reduced earthwork stiffness leads to increased SD values, especially at high moisture contents. Reduced stiffness earthworks tend to exacerbate the effects of both ballast fouling and moisture content, leading to more pronounced settlement over time.

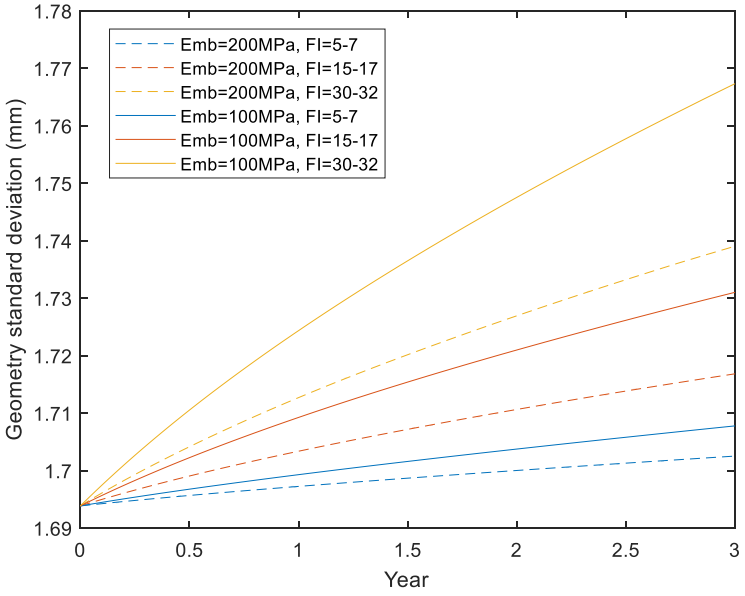

Figure 7.5 Standard deviation evolution over time considering varying embankment stiffness and varying ballast FI

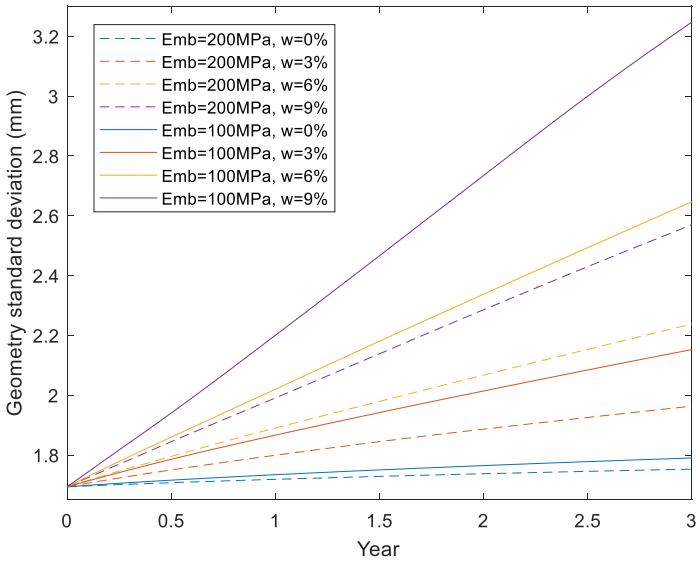

Figure 7.6 Standard deviation evolution over time considering varying embankment stiffness for varying moisture contents

Table 7.4 Predicted SD after 3 years of traffic considering varying embankment stiffness and varying ballast FI

FI from year 1 to year 3	SD after 3 years of traffic in mm		Percentage increase
	Embankment E = 200MPa (Baseline case)	Embankment E = 100MPa	
5 –>7	1.703	1.708	0.31%
15 –> 17	1.717	1.731	0.82%
30 –>32	1.739	1.767	1.62%

Table 7.5 Predicted SD after 3 years of traffic considering varying embankment stiffness and varying moisture contents

Moisture of fines %	SD after 3 years of traffic in mm		Percentage increase
	Embankment E = 200MPa (Baseline case)	Embankment E = 100MPa	
0	1.753	1.790	2.13%
3	1.963	2.153	9.63%
6	2.238	2.647	18.26%
9	2.570	3.248	26.37%

Considering the worst-case scenario of a ballast FI of 40 and moisture content (w) of 9%, Figures 7.7(a) and 7.7(b) present the distribution of deviatoric stresses across the depths of the track-bed under quasi-static and dynamic excitations respectively. In these plots, the track-bed layers are defined as ballast, sub-ballast, and embankment. Observations indicate the reduced stiffness of the embankment influence the distribution of deviatoric stress within the track-bed. A stiffer embankment leads to an increase in deviatoric stresses within the embankment layer but a decrease in deviatoric stresses within the ballast layer. Specifically, within the ballast layer, the deviatoric stresses in the case of the reduced stiffness embankment are markedly higher compared to those in the baseline scenario. It should be noted that deviatoric stress (i.e. rather than solely vertical stress) is a key factor affecting settlement, with the majority of the settlement predominantly occurring within the ballast layer (Charoenwong et al., 2023).

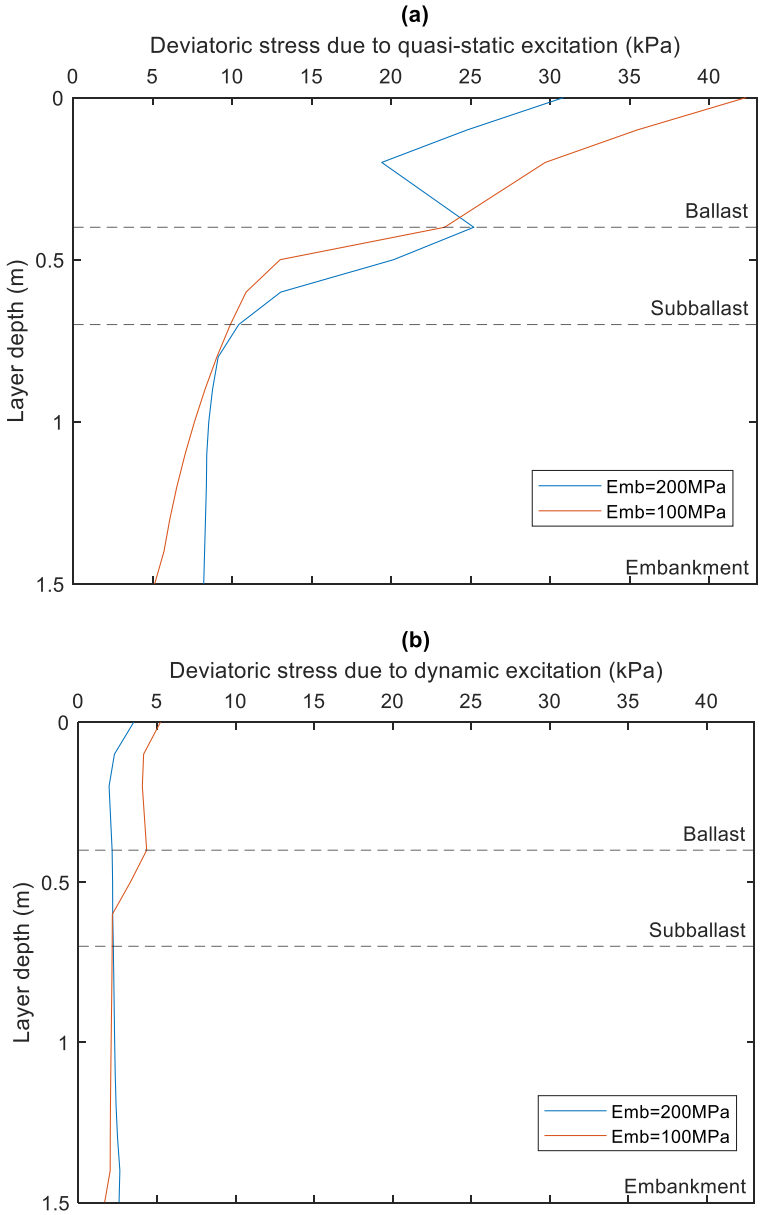

Figure 7.7 Deviatoric stresses within the track-bed considering varying embankment stiffness: (a) quasi-static excitation (b) dynamic excitation

7.7 The effect of linespeed

Using the same track properties and initial track profile from the previous analyses, this section studies the impact of train speed on settlement, in the presence of fouled ballast. The investigation involves the simulations of three different speeds: 100, 150, and 200 km/h.

Figures 7.8(a), 7.8(b), and 7.8(c) illustrate the evolving SD over a period from year 1 to year 3 for three speeds, each considering a different ballast FI. The corresponding SD's after 3 years of traffic are summarised and compared in

Table 7.6. Using the speed of 150 km/h as a baseline case, it is found that for initial FI's of 5, 15, and 30, increasing the speed to 200 km/h results in SD increases of 0.25%, 0.66%, and 1.30%, respectively. Conversely, reducing the speed to 100 km/h leads to decreases in SD of 0.01%, 0.03%, and 0.06%, respectively. These results demonstrate that increased train speed results in higher track settlement. Specifically, when the speed is increased from 150 km/h to 200 km/h, there is a noticeable increase. This trend is consistent and escalates with higher FIs, suggesting that faster trains exert more stress on the track, exacerbating the settlement issues, particularly for fouled ballast conditions. While the reductions are relatively small, they indicate that slower train speeds marginally counteract the impact of ballast fouling on track settlement.

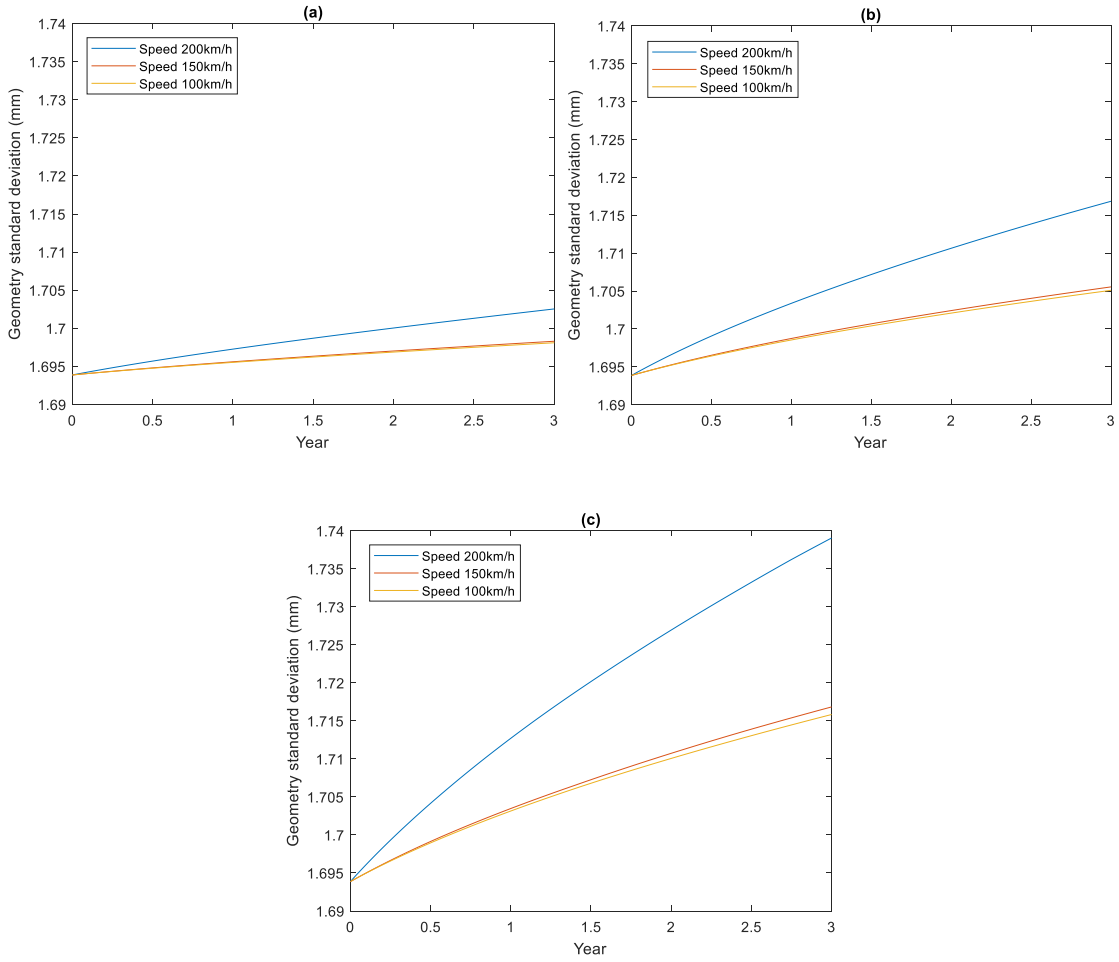

Figure 7.8 Standard deviation evolution over time considering varying train speeds: (a) FI = 5 (b) FI = 15 and (c) FI = 30

Table 7.6 Predicted SD after 3 years of traffic considering varying train speeds for varying ballast FI

FI from year 1 to year 3	SD after 3 years of traffic in mm *(Percentage change)*		
	200km/h	**150km/h**	**100km/h**
5 –> 7	1.703 *(0.25% increase)*	1.698 *(Baseline)*	1.698 *(0.01% decrease)*
15 –> 17	1.717 *(0.66% increase)*	1.706 *(Baseline)*	1.705 *(0.03% decrease)*
30 –> 32	1.739 *(1.30% increase)*	1.717 *(Baseline)*	1.716 *(0.06% decrease)*

Similarly, Figures 7.9(a), 7.9(b), and 7.9(c) demonstrate the SD evolution over the same period for varying train speeds, this time accounting for four different levels of moisture content. The corresponding SD's after 3 years of traffic are summarised and compared in Table 7.7. When the speed is increased from 150 km/h to 200 km/h, the SD rises by 1.68%, 7.64%, 15.16%, and 22.95%, respectively. Conversely, when the speed is decreased to 100 km/h, the SD reduces by 0.08%, 0.45%, 1.28%, and 2.92% for each respective moisture content level. These results are consistent with the earlier trend: increasing the speed from 150 km/h to 200 km/h results in significant rises in SD. The substantial increases in SD with higher moisture contents at increased speeds highlight the compounded effect of moisture and speed on track settlement. Conversely, reducing the speed to 100 km/h leads to a reduction in SD.

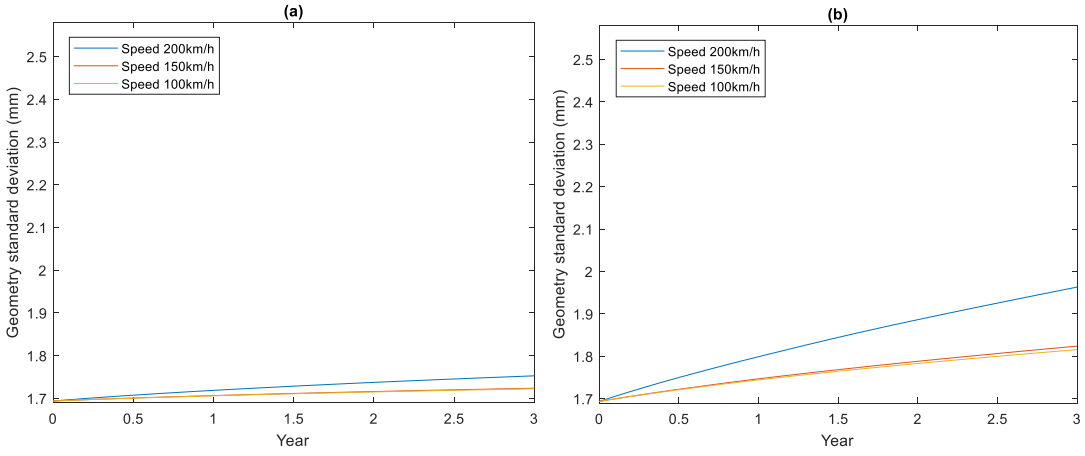

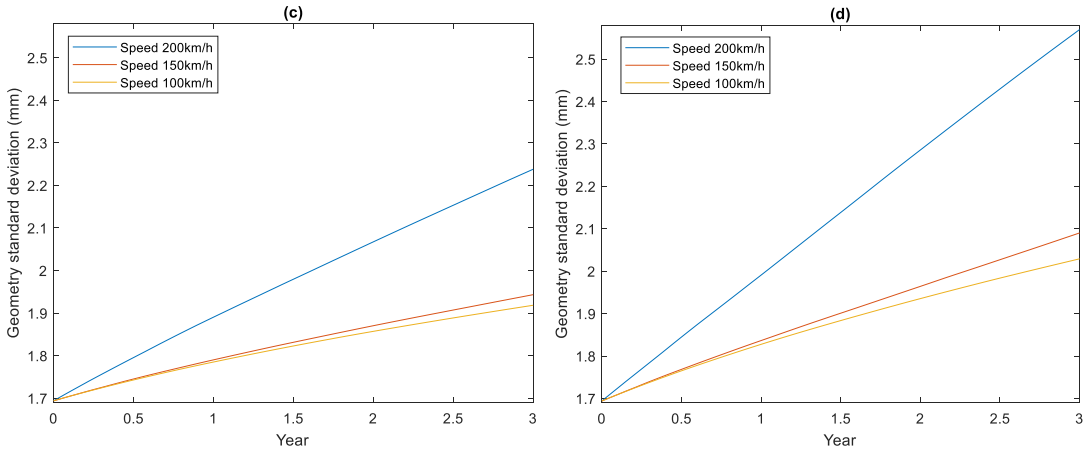

Figure 7.9 Standard deviation evolution over time considering different train speeds: (a) w = 0% (b) w = 3% (c) w = 6% and (d) w = 9%

Table 7.7 Predicted SD after 3 years of traffic considering different train speeds and varying moisture contents

Moisture of fines %	SD after 3 years of traffic in mm *(Percentage change)*		
	Speed 200km/h	**Speed 150km/h**	**Speed 100km/h**
0	1.753 *(1.68% increase)*	1.724 *(Baseline)*	1.723 *(0.08% decrease)*
3	1.963 *(7.64% increase)*	1.824 *(Baseline)*	1.816 *(0.45% decrease)*
6	2.238 *(15.16% increase)*	1.943 *(Baseline)*	1.918 *(1.28% decrease)*
9	2.570 *(22.95% increase)*	2.090 *(Baseline)*	2.029 *(2.92% decrease)*

Considering the scenario exhibiting the most pronounced effects (ballast FI is 40 and the moisture content (w) is 9%), Figures 7.10(a) and 7.10(b) illustrate the distribution of deviatoric stresses throughout the depths of the track-bed under quasi-static and dynamic excitations, respectively. Observations indicate that a reduction in speed from 150 km/h to 100 km/h results in a slight decrease in deviatoric stresses caused by both quasi-static and dynamic excitations along the track-bed. Conversely, an increase in speed from 150 km/h to 200 km/h leads to a more significant escalation in deviatoric stresses, for both excitation types, compared to those observed at a speed of 100 km/h.

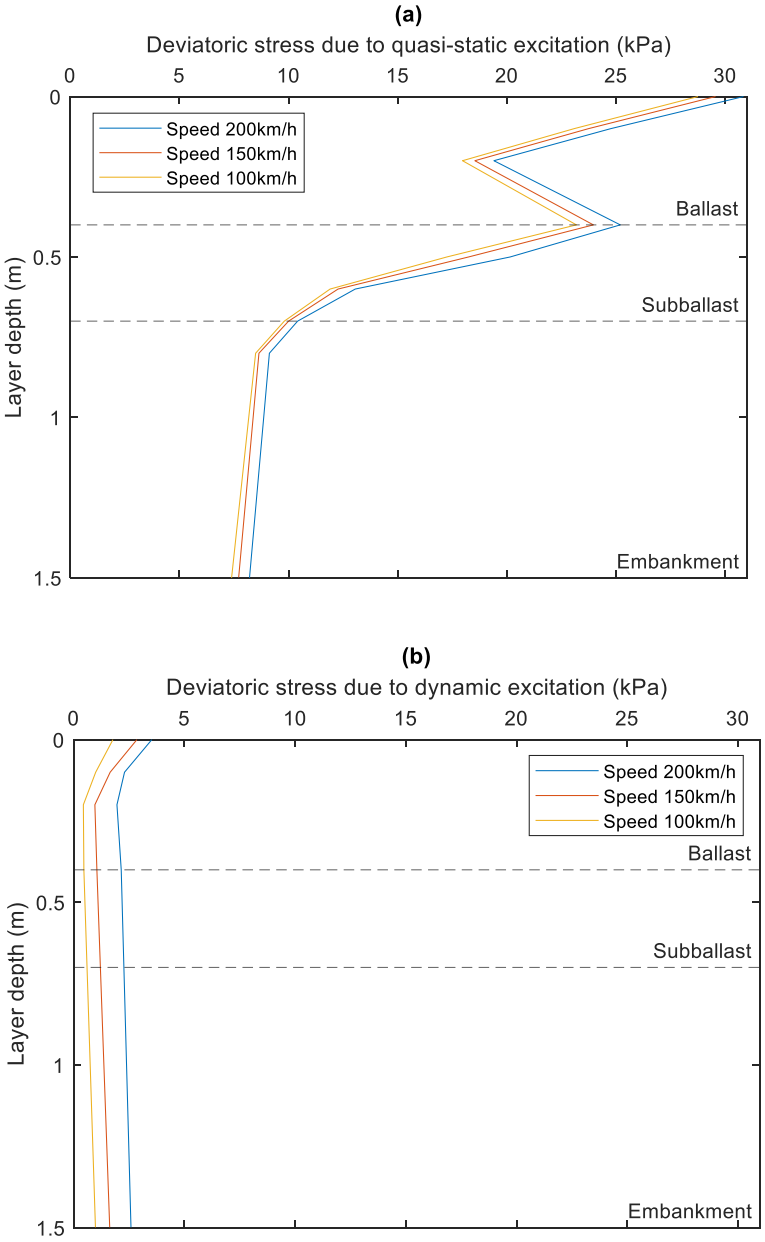

Figure 7.10 Deviatoric stresses within the track-bed considering different train speeds: (a) quasi-static excitation (b) dynamic excitation

7.8 Discussion

It is evident that ballast moisture content and ballast fouling index have a linked effect on differential track settlement, as shown in Table 7.8. When the fouling index is low, water can flow freely through the ballast and can quickly exit the track. However, when fouling index is high, water drains more slowly and/or gets trapped in the ballast matrix. This can be effected depending upon whether the fouling material is primarily cohesive (e.g. from mud pumping) or granular (e.g. from ballast particle abrasion). Then in the presence of elevated

water content there is greater scope for ballast particulates to rearrange, this leading to more rapid settlement. This is in contrast to the case of when fouling index is high but moisture content is low. In this scenario the fines have a limited effect on the rearrangement of ballast particles and any increases in settlement rate are marginal. The effects of fouling index and moisture content are magnified when the train speed is increased or the earthworks stiffness is low. This is because both scenarios lead to elevated deviatoric stresses within the ballast and supporting earthworks. This then induces increased settlement.

These findings underscore the importance of moisture management in maintaining track stability. Effective drainage and ballast quality are crucial to managing track geometry. Additionally, the track geometry should be kept in a condition suitable for the linespeed and the earthworks should give adequate support to the track. Note that in Table 7.8, the case of a low fouling index and high moisture content is classified as ‘situation dependent’. This is because the presence of high levels of standing water, particularly if moving, can destabilise the ballast through the movement of stones, and erosion of the trackbed. This can result in rapid track settlement after the line is reopened and trains commence running at normal linespeed.

Table 7.8 Correlation of Fouling Index, Moisture Content, and Settlement Rate

Fouling index	Moisture content	Settlement rate
Low	Low	Low
Low	High	Site dependent
High	Low	Moderate
High	High	High

Chapter 8
Analysis of rolling stock characteristics

8.1 Introduction

The settlement of railway trackbed is non-linear (Ramos et al., 2020), and thus changes in a track quality index (TQI) are also often non-linear. Thus, to analyse changes in different settlement and TQI requires a numerical model that is capable of simulating daily rolling stock patterns, accounting for interactions between the different traffic types that operate in the railway infrastructure. For example, if a solely passenger line was upgraded to carry multiple freight train movements, the track resulting geometry would likely be different depending upon whether these freight trains were all run consecutively, or interspersed between passenger movements. Therefore, to most faithfully replicate changes in TQI, the traffic timetable should closely replicate true operation conditions, and vertical track profile should be updated after every axle passage.

To determine the relationship between TQI and tamping frequency, and thus economic cost, marginal cost analysis (Smith et al., 2021) is a useful tool. It is an important area academically and in practice given the vertical separation between infrastructure management and train operations, requiring track access charges to be set. For example, EU legislation (Directive 2012/34/EU, and the European Commission's Implementing Regulation EU 2015/909) stipulates that those charges should be based on direct costs of a train service, which can contribute to an efficient use of the infrastructure.

In this chapter, an engineering-economic approach is used to calculate marginal costs considering the evolution of railway track geometry. The model is used to calculate marginal costs of two scenarios: 1) increasing the linespeed on a passenger line, and 2) increasing the number of passenger or freight movements on a predominantly passenger line.

8.2 Engineering-economic modelling

A combination of engineering and economic modelling is used to predict tamping intervals and marginal costs as outlined in Figure 8.1. The details of the engineering model are described in Chapter 3.

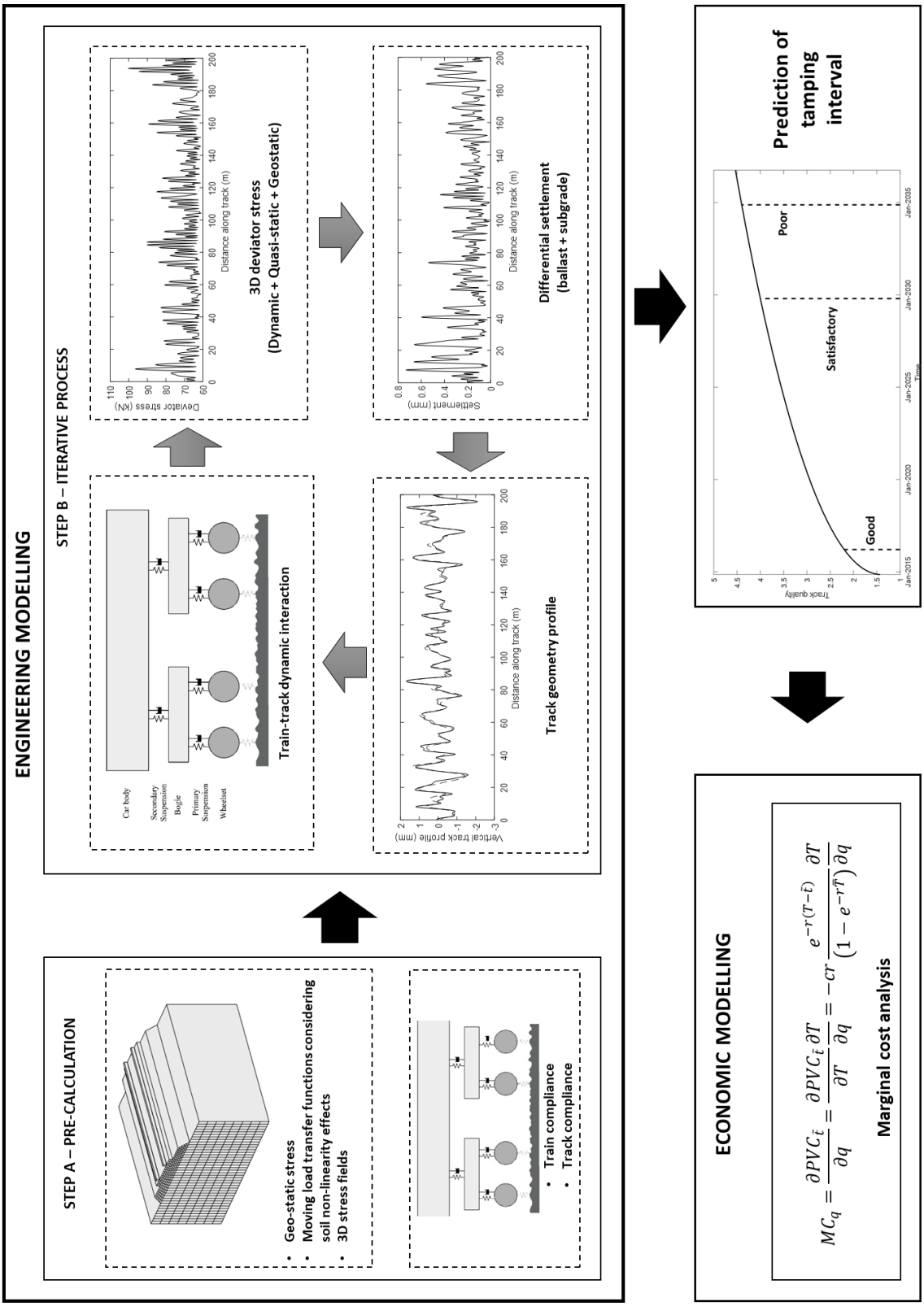

Figure 8.1 Engineering-economic model overview

The engineering model provides the inputs for the economic model. The generalised, coupled modelling approach for direct cost calculation is:

1) Simulate the damage from increasing the linespeed or running more trains using the engineering model
2) Determine the timeframe until damage correction is required
3) Calculate a unit cost of damage correction to give additional cost of increased linespeed or extra traffic on the network

The cost calculations only consider changes in tamping intervals and do not include investments in the capability of the line, i.e. fixed inputs in the production of infrastructure services. The calculated costs therefore comprise short-run marginal costs rather than long-run marginal costs. This makes the estimates consistent with the concept of direct costs for the purposes of setting track access charges.

Assuming tamping is the primary form of maintenance used to improve the SD of track, the present value cost (PVC) of an infinite time series of tamping activities at time T with constant intervals $\bar{T}$ is:

$$\lim_{n\to\infty} PVC = c\frac{1}{(1-e^{-r\bar{T}})} \quad \textbf{(8-1)}$$

Where $\lim_{n\to\infty}$ represents the limit as the number of tamping activities approaches infinity; c is the tamping cost per track kilometre, and r is the annual discount rate.

Following the marginal cost calculation for track renewals in (Andersson et al., 2016), a track section that is observed at time $\tilde{t}$ is considered, which is before the first tamping activity at T. The time until the next tamping activity is thus $T-\tilde{t}$. The PVC of the track section analysed in time $\tilde{t}$ is:

$$PVC_{\tilde{t}} = ce^{-r(T-\tilde{t})}\frac{1}{(1-e^{-r\bar{T}})} \quad \textbf{(8-2)}$$

To calculate a marginal cost of additional train movements, a temporary increase in tonnes Δq at time $\tilde{t}=0$ is considered, which will make the first tamping interval shorter, and all the subsequent intervals will be scheduled earlier. The subsequent intervals will have the same length as before since

the traffic increase is temporary, i.e. the calculation considers the effect of one extra traffic unit running on the line. This is illustrated in Figure 8.2 where T_1 is the first tamping time for the baseline case (no change to traffic), $T_1 + \bar{T}$ is the second interval etc., whilst T_2 and $T_2 + \bar{T}$ are the corresponding intervals for the scenario where traffic (temporarily) increases. The tamping activities are typically determined by a track geometry SD limit, as shown in Figure 8.2. Note that railway administrations may also monitor the rate of change of track geometry SD and intervene if it increases suddenly, rather than only focusing on a limit value. This type of increase is more ad-hoc and can be associated with a variety of alternative deterioration mechanisms, including shrink-swelling of clay embankments. Therefore this approach focuses upon planned interventions.

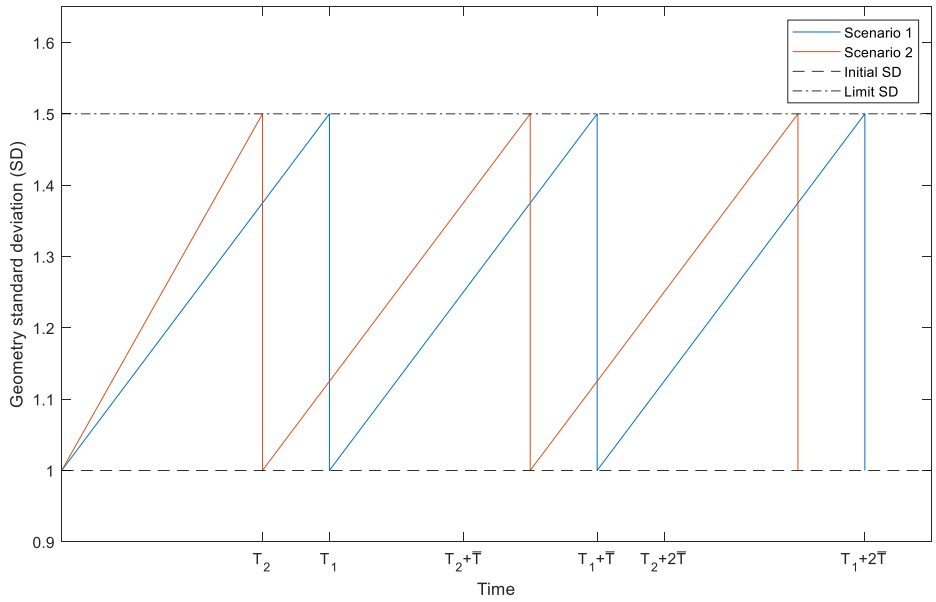

Figure 8.2 Idealised tamping interval concept for two scenarios

The marginal cost is expressed as:

$$MC_q = \frac{\partial PVC_{\tilde{t}}}{\partial q} = \frac{\partial PVC_{\tilde{t}}}{\partial T}\frac{\partial T}{\partial q} = -cr\frac{e^{-r(T-\tilde{t})}}{(1-e^{-r\bar{T}})}\frac{\partial T}{\partial q} \quad \textbf{(8-3)}$$

In this calculation, an increase in traffic during the first tamping interval is considered which can be expressed as the change in the average annual tonnes, $\frac{\partial \bar{q}_1}{\partial q}$. As noted by (Andersson et al., 2016; Öberg et al., 2007), this

change can be approximated as $\frac{\partial \bar{q}_1}{\partial q} \approx \frac{1}{T}$, which has a decreasing error the more stable the traffic volume is. That is, the change in tamping interval due to a (percentage) change in tonnes:

$$\frac{\partial T}{\partial q} = \frac{\partial T}{\partial \bar{q}_1}\frac{\partial \bar{q}_1}{\partial q} = \frac{\partial T}{\partial \bar{q}_1}\frac{1}{T} \quad \textbf{(8-4)}$$

This is expressed in terms of a deterioration elasticity, $\gamma_q = \frac{\partial T}{\partial \bar{q}_1}\frac{\bar{q}_1}{T}$. The marginal cost in eq. (8-1) is expressed as:

$$MC_q = \frac{\partial PVC_{\tilde{t}}}{\partial q} = -cr\frac{e^{-r(T-\tilde{t})}}{(1-e^{-r\bar{T}})}\frac{\gamma_q}{\bar{q}_1} \quad \textbf{(8-5)}$$

Note that c is the cost per track-km, which is multiplied by one over tonnage ($\frac{1}{\bar{q}_1}$), and the marginal cost is thus a cost per tonne per track-km, i.e. cost per tonne-km.

The marginal cost calculation for a temporary change in the speed (v) for traffic is like the calculation for an increase in tonnage. The deterioration elasticity γ_v is the percentage change in tamping interval after a percentage change in speed, and $\bar{v}_1$ is the annual speed during the first tamping interval. This marginal cost calculation also uses cost per track-km (c), which is multiplied by one over speed ($\frac{1}{\bar{v}_1}$) and the marginal cost is thus expressed as a cost per v per track-km (i.e. cost per v-km). In other words, it is the extra cost per v (km/h) for a train running on one km of track.

$$MC_v = \frac{\partial PVC_{\tilde{t}}}{\partial v} = \frac{\partial PVC_{\tilde{t}}}{\partial T}\frac{\partial T}{\partial v} = -cr\frac{e^{-r(T-\tilde{t})}}{\left(1-e^{-r\bar{T}}\right)}\frac{\partial T}{\partial v} = -cr\frac{e^{-r(T-\tilde{t})}}{(1-e^{-r\bar{T}})}\frac{\gamma_v}{\bar{v}_1} \quad \textbf{(8-6)}$$

8.3 Case studies

The validated model is used to perform two analyses. Firstly it is used to analyse the effect of increasing line speed on differential track settlement, comparing speeds of 201, 209, 217 and 225km/h (125, 130, 135 and 140mph).

Secondly, it is used to investigate the effect of adding additional passenger or freight trains on the settlement of an existing track.

8.3.1 Track parameters

The finite element track mesh is shown in Figure 8.3. The track parameters including the characteristics of the rails, rail pads, sleepers, ballast, sub-ballast and subgrade are summarised in Table 8.1. Considering the two applications under investigation (linespeed and additional trains), the only track difference is the vertical geometry track profile.

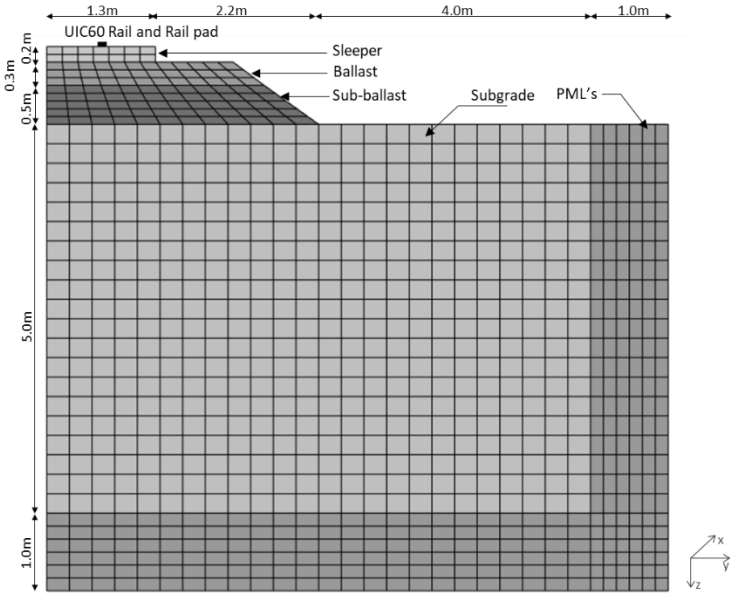

Figure 8.3 Finite element mesh of the track model (case studies)

Table 8.1 Ballasted track properties (case studies)

Component	Parameter	Value
UIC 60 Rail (single rail)	Height (m)	0.172
	Length in transversal direction (m)	0.015
	Section area (m^2)	7.677×10^{3}
	Moment of Inertia y-y (m^4)	3.038×10^{-5}
	Moment of Inertia z-z (m^4)	0.512×10^{-5}
	Young's modulus (Pa)	2.11×10^{11}
	Density (kg/m^3)	7850
	Poisson's ratio	0.3
	Hysteretic damping coefficient	0.01

Component	Parameter	Value
Railpad (spring element)	Continuous stiffness (N/m^2)	255x10^6
	Viscous damping (Ns/m^2)	22.5x10^3
Sleeper (G44)	Height (m)	0.2
	Length in transversal direction (m)	2.5
	Sleeper spacing (m)	0.65
	Young's modulus (Pa)	3x10^{10}
	Density (kg/m^3)	2500
	Poisson's ratio	0.15
	Hysteretic damping coefficient	0.01
Ballast	Height (m)	0.3
	Length in transversal direction (m)	2.8
	Young's modulus (Pa)	180x10^6
	Density (kg/m^3)	1650
	Poisson's ratio	0.27
	Hysteretic damping coefficient	0.06
Sub-ballast (Sand-gravel)	Height (m)	0.5
	Length in transversal direction (m)	3.5
	Young's modulus (Pa)	180x10^6
	Density (kg/m^3)	2300
	Poisson's ratio	0.3
	Hysteretic damping coefficient	0.05
	Settlement parameter a	0.52
	Settlement parameter b	0.15
	Settlement parameter m	1.49
	Compressive strength (kPa)	350
Subgrade (Lean clay)	Height (m)	5
	Young's modulus (Pa)	70x10^6
	Density (kg/m^3)	1900
	Poisson's ratio	0.35
	Hysteretic damping coefficient	0.03
	Settlement parameter a	260
	Settlement parameter b	1.10
	Settlement parameter m	0.16
	Compressive strength (kPa)	2.0

8.3.2 Operational parameters

The operational parameters are kept similar to the validation case, with a traffic volume per year of 19.58 million gross tons (MGT), and an average traffic volume per day of 0.054 MGT. The traffic volume is converted to passenger trains assuming an 11-car train with 17 tonne axle loads.

$$\text{Number of trains per MGT} = \frac{10^6}{(44 * 17)} \approx 1337 \text{ trains}$$

The MGT per passenger train is thus approximately $\left(\frac{1}{1337} \approx\right)$ 0.00075. For freight trains, the calculation is based on a 50-car train with 25 tonne axle weights.

$$\text{Number of trains per MGT} = \frac{10^6}{(160 * 25)} \approx 250 \text{ trains}$$

The MGT per freight train is thus $\left(\frac{1}{250} =\right)$ 0.004.

8.3.3 Tamping costs

A tamping cost per track-km is required to calculate a marginal cost. It is assumed tamping is performed using machines with an output of 400 m/h, and a mean cost per shift of £9k. The on-site working time is approximated as 3-4 hours (e.g. 07/08 Plasser or equivalent Matisa machines), however it is recognised that productive time is highly variable, due to the many factors that influence transit from the stabling point to site and return. This means approximately 1.6 track-km can be tamped during a shift. The tamping cost per track-km is then £5,625. The engineering simulations cover 200 metre lengths of track, however it is assumed the machine and shift will do a longer section, and calculate costs per track-km.

8.4 Engineering analysis

Two analyses are performed. First, the influence of linespeed on differential track settlement is investigated, considering four linespeeds: 201, 209, 217 and 225km/h (125, 130, 135 and 140mph). The second analysis is the influence of increased passenger and freight train movements on the settlement of a predominantly passenger-only line.

8.4.1 The influence of linespeed on track settlement

The profile used for the previous validation case is worse than typically allowable on a track with a linespeed of 225km/h. Therefore a starting track geometry profile is artificially generated using the PSD function (Federal Railroad Administration, 1980). Wavelengths between 3-35m are used because the aim of the model is to predict automated tamping intervals, and this range is typically associated with the faults that can be corrected via tamping. An initial track profile characterised by a SD of 1.03mm over 200m length is generated and it is assumed the track historically experienced 100k cycles of passenger train axles prior to the start of the simulations. This is intended to replicate the influence the dynamic track stabilisation process commonly performed post-renewal. Then the model simulates differential settlement evolution due to traffic, to a threshold of 1.5mm for four moving speeds: 201, 209, 217 and 225km/h. For all speeds the track and its vertical profile remain fixed.

Figure 8.4 illustrates the 3D track-ground displacement contour for the passenger train at 201km/h and the response propagating from the rail into supporting track-ground structure. Note that for Figure 8.4(a), although the domain shown is the full 200m track section with a 158.9m long train, to maximise viewability, the x-axis is scaled by a factor of 8 compared to the y and z-axis.

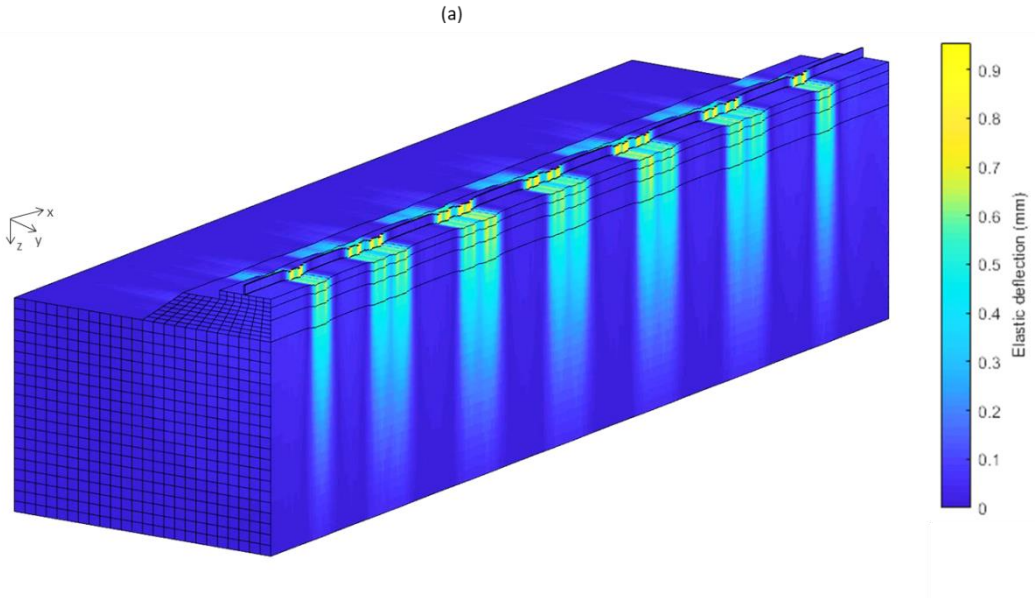

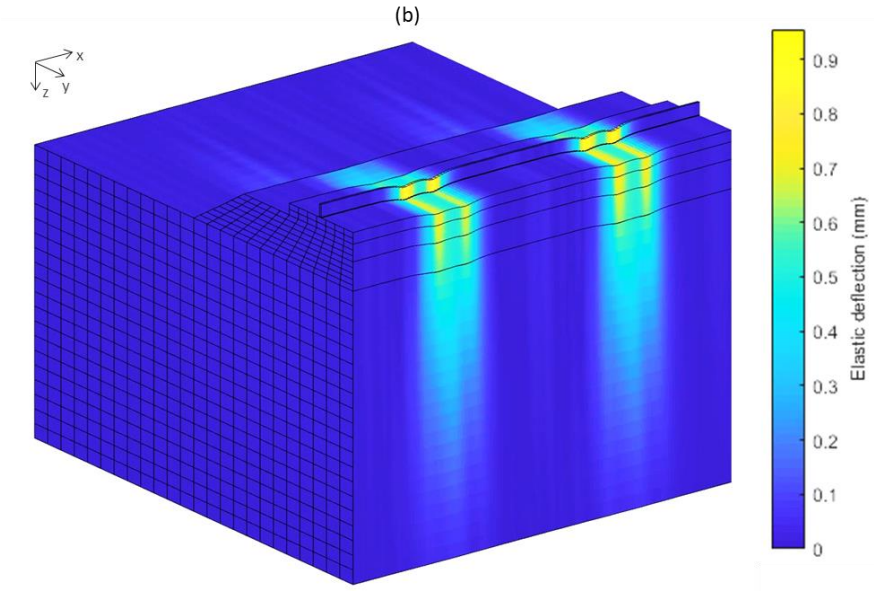

Figure 8.4 3D track-ground deflection profile (slice along track centreline considering both quasi-static and dynamic excitation): (a) a full vehicle over a 200m track length with an XYZ aspect ratio of [8 1 1] (b) one car zoomed in over a 40m track length

Figure 8.5 shows the vertical track geometry profiles for the four different speeds at the instant they reach the threshold limit. Similarly, Figure 8.6 compares the evolving geometry SD over time from the initial SD value until the threshold limit. The corresponding time until threshold exceedance is summarised and compared in Table 8.2. The time until threshold exceeded when running passenger trains with speeds 201, 209, 217 and 225km/h are 697, 620, 585 and 568 days, respectively. These correspond to reductions of: 11%, 16.1%, and 18.5%.

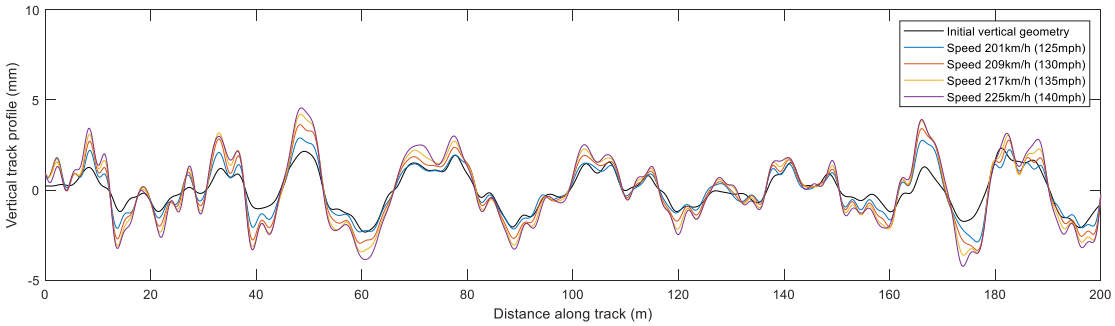

Figure 8.5 Vertical track profiles after reaching the threshold limit for four train speeds (3-35m wavelength filter)

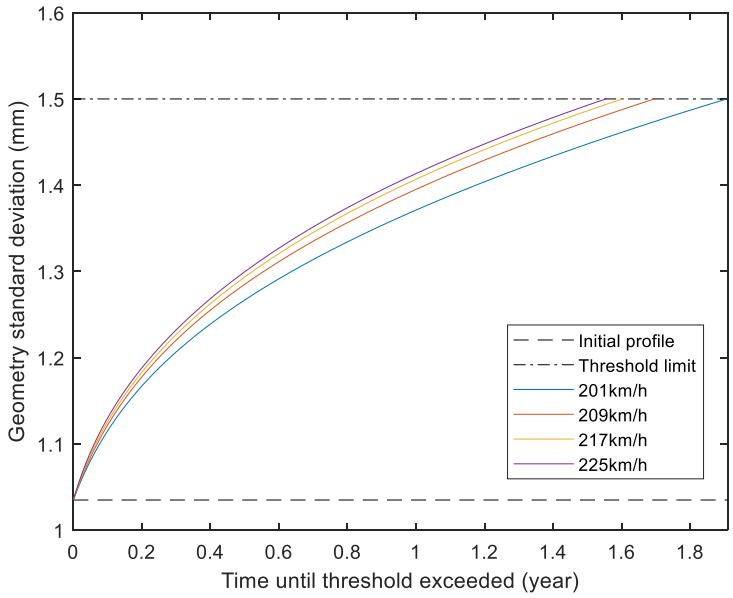

Figure 8.6 Vertical rail profile standard deviation evolution over time for varying linespeeds

Table 8.2 Time until threshold exceedance for varying linespeeds

Linespeed (km/h)	Time until threshold exceeded (days)	Percentage decrease
201	697	0%
209	620	11.0%
217	585	16.1%
225	568	18.5%

These reductions show linespeed increases can have an important impact on differential track settlement, and the time until threshold exceedance is significantly reduced. This is further confirmed in Figure 8.7, which shows rates of SD change per year for each linespeed. The rate of SD change per year is approximately 0.244mm for a speed of 201km/h and increases to 0.274, 0.290 and 0.299mm when increasing line speed to 209, 217 and 225km/h respectively. Also, Figure 8.8 illustrates the moving average of SD over time, for each line speed. It should be noted that the degradation is sensitive to the rolling stock dynamics, and it is assumed that the speed of existing rolling stock would just be increased. In real life, considering the increased speed, dedicated high speed trains might be chosen, with different dynamics and wheel profiles, depending on the radius of curves on the route. Further, track improvements (e.g. under sleeper pads) might also be installed to improve the

track's structural response, before increasing linespeed. These factors would influence track settlement.

To further investigate the drivers behind the growth in settlement, the deviatoric stresses due to the vehicle's quasi-static and dynamic loading components are shown in Figure 8.9 and Figure 8.10. Quasi-static excitation represents the rolling stock components that are not excited during vehicle-track interaction, and thus act as a constant moving force. The relevance of this excitation mechanism grows when approaching the track-ground critical velocity (Connolly et al., 2020; Connolly & Costa, 2020), but is insensitive to track irregularities. Alternatively, the dynamic excitation is related to the train-track interaction, and heavily influenced by the wheel-rail irregularities and vehicle suspension. Table 8.3 summarises the percentage differences in mean deviatoric stress measured at subgrade surface when increasing linespeed. Considering the stress field in 3D, the deviatoric stress is calculated which is dependent on the sum of squares of the differences of the principal stresses. It is shown that quasi-static deviatoric stresses increase by 1.8%, 3.7% and 5.8%, while the dynamic deviatoric stresses increase by 4.1%, 7.8% and 12.7%, when increasing linespeed to 209, 217 and 225km/h, respectively. Considering deviatoric stress is directly related to permanent deformation, the increase in dynamic excitation contributes more dominantly to the differential settlement than quasi-static.

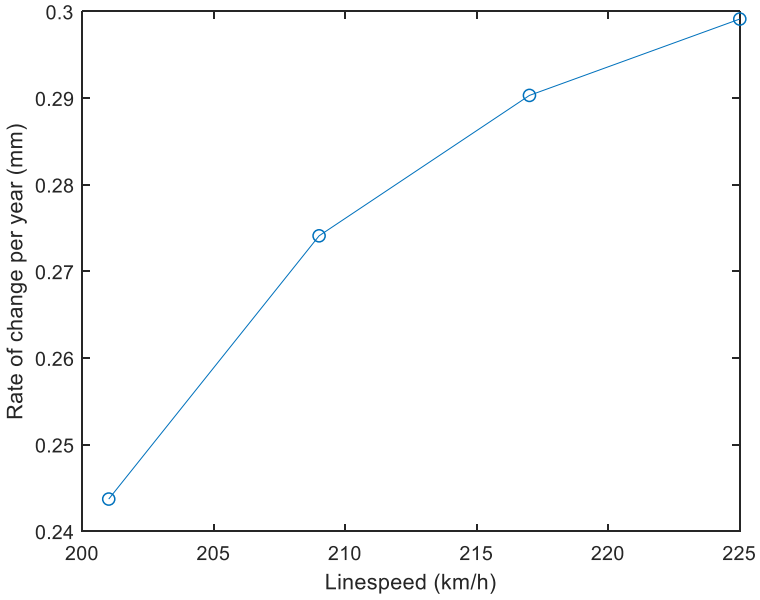

Figure 8.7 Rates of average SD change per year for each line speed

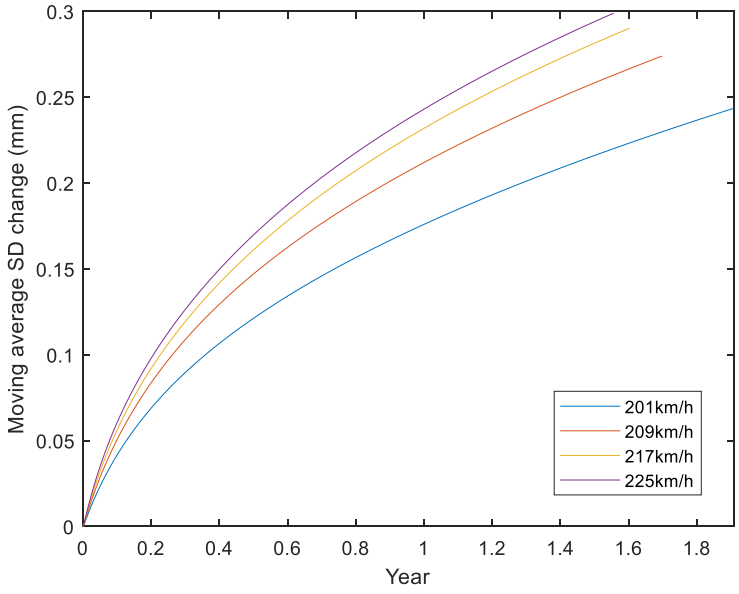

Figure 8.8 Moving average SD change over time

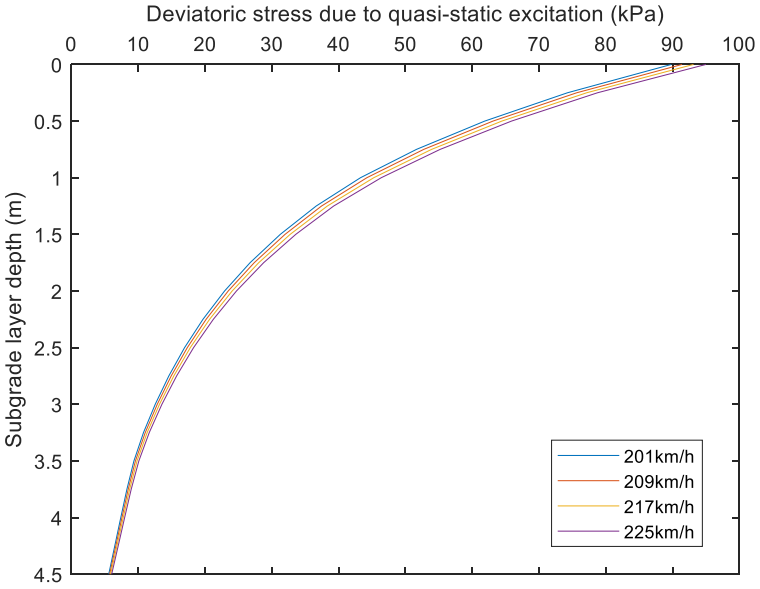

Figure 8.9 Deviatoric stress vs depth, due to quasi-static vehicle excitation

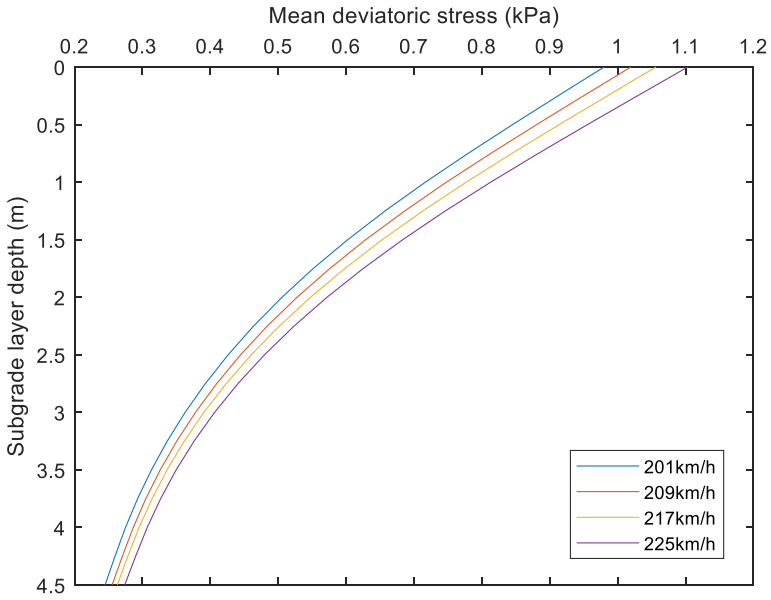

Figure 8.10 Deviatoric stress vs depth, due to dynamic vehicle excitation

Table 8.3 Percentage differences in deviatoric stress

Linespeed (km/h)	Percentage difference in deviatoric stress	
	Quasi-static excitation	Dynamic excitation
201	0%	0%
209	1.8%	4.1%
217	3.7%	7.8%
225	5.8%	12.7%

8.4.2 The influence of increased train movements on track settlement

Four traffic scenarios are simulated. Firstly, the case of 100% passenger trains acts as the baseline case. Then, three additional scenarios are simulated to understand the effect of adding additional passenger or freight services to the baseline case: B) adding 1 passenger train, C) adding 1 freight train, and D) adding 2 freight trains. The relationship between these scenarios and annual operational tonnage is summarised in Table 8.4. The passenger and freight trains are operated at constant speeds of 200 and 97km/h, respectively. For all cases, the number of passenger train movements are equal, or higher, than the baseline case. Considering the high number of passenger movements per day on the line, it is challenging to add slow-moving freight movements between individual passenger trains during the hours of peak travel. Instead, on such a line is realistic to assume that passenger services run during the day, while

freight movements are confined to evenings/nights. To simulate such a scenario, the required daily number of passenger trains are run in a row, followed by the daily number of freight trains. Therefore there is interdependency between the differential settlements induced by both vehicle types.

Table 8.4 Operational mixed railway traffic scenarios

	Scenario A	Scenario B	Scenario C	Scenario D
Passenger trains/day	72	73	72	72
Freight trains/day	0	0	1	2
Passenger MGT/day	0.054	0.05475	0.054	0.054
Freight MGT/day	0	0	0.004	0.008
Passenger MGT/year	19.58	19.5875	19.58	19.58
Freight MGT/year	0	0	1.46	2.92
Total MGT	19.58	19.5875	21.04	22.50

The same track is considered as for the previous linespeed analysis. However, considering the lower maximum linespeed under consideration, and that the line experiences mixed traffic, the typical SD is likely to be higher. Therefore, assuming a maximum operational linespeed of 200km/h, an initial track profile is artificially generated with SD=1.7mm, and the threshold limit is set as 2.4mm. To keep the analysis consistent, as for the linespeed analysis, it is assumed that the track has also experienced 100k loading cycles at the start of the numerical simulations. In reality, this number is likely to be higher unless maintenance activity is performed prior to introducing the additional traffic movements. Also, note that it is assumed the track has experienced freight traffic in the past and therefore has experienced equivalent stress states. Thus, the empirical relationship between settlement and deviatoric stress is valid for both passenger and freight vehicles.

Regarding simulation results, the evolving geometry SD over time, from the initial SD value until the threshold limit value is compared in Figure 8.11, and summarised in Table 8.5. The durations until threshold exceedance for scenarios A, B, C and D are 579, 573, 539 and 504 days respectively. Note that the time until the threshold is exceeded in the baseline scenario A is shorter (579 days) than in the previous linespeed analysis (697 days) because a different initial track profile and threshold limit is under consideration.

It is found when adding 1 passenger train per day (1.4% MGT) the time-to-maintenance reduces by 1.0%. In contrast, the time reduces by 6.9% when adding 1 freight train per day (7.4% MGT) and 13.0% when adding 2 daily freight trains (14.8% MGT).

This shows the effect of additional freight traffic is more pronounced in comparison to adding additional passenger services, which is due to differing dynamic characteristics of the vehicles and also quasi-static load. This is shown in greater depth in Figure 8.12 which displays the effect of traffic on SD evolution between days 2.8 and 3.1, for scenario D. The gradient of SD change is greater during the hours of freight train passage, compared to passenger.

The relationship between the effect of each scenario on MGT and the duration until threshold exceedance is also shown in Table 8.5. It is seen that there is a positive correlation between both, however for the additional passenger train case, compared to the freight case, the increase in maintenance relative to MGT increase is lower.

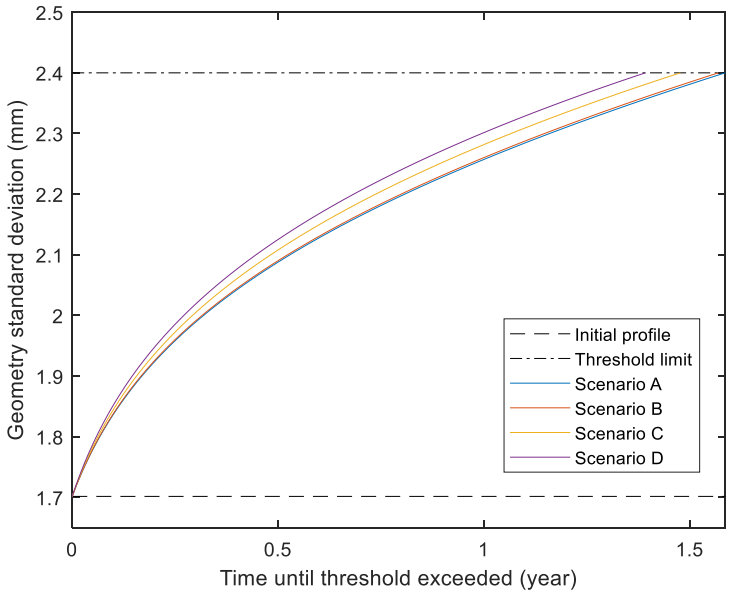

Figure 8.11 Standard deviation with duration until threshold exceedance for four scenarios

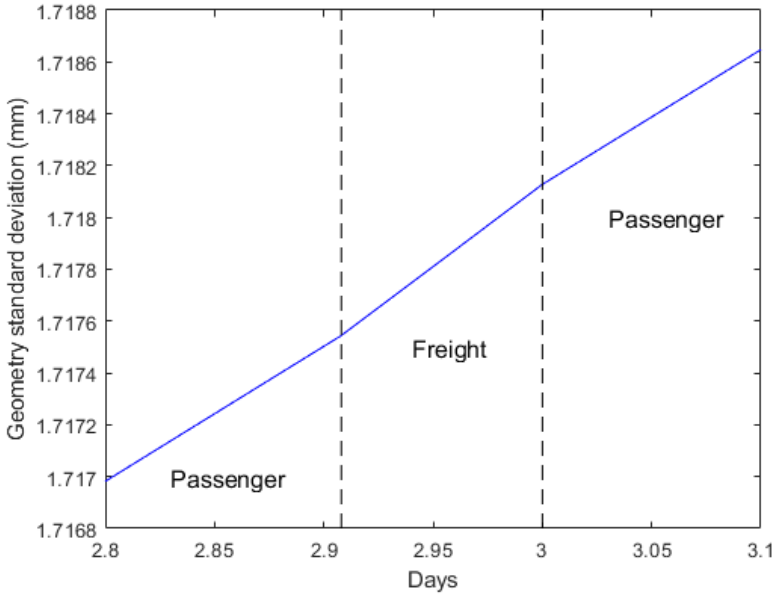

Figure 8.12 Standard deviation change over 24 hours for scenario D

Table 8.5 Time until threshold exceeded for additional passenger and freight scenarios

Traffic scenario	Percentage increase in MGT	Time until threshold exceeded (days)	Percentage decrease in time
(A) 100% passenger trains	0%	579	0%
(B) Adding 1 passenger train per day	1.4%	573	1.0 %
(C) Adding 1 freight train per day	7.4%	539	6.9%
(D) Adding 2 freight trains per day	14.8%	504	13.0%

8.5 Marginal tamping cost analysis

8.5.1 The influence of linespeed on cost

The deterioration elasticity with respect to speed, $\gamma_v = \frac{\partial T}{\partial \bar{v}_1}\frac{\bar{v}_1}{T}$, is calculated using the percentage change in tamping intervals divided by the percentage change in km/h. The same approach is used when calculating the deterioration elasticity with respect to gross tonnes, $\gamma_q = \frac{\partial T}{\partial \bar{q}_1}\frac{\bar{q}_1}{T}$. These elasticities are negative because increased linespeed or increased gross tonnes reduces the time until the threshold for track geometry SD is exceeded. The elasticities are combined with tamping costs per track-km to calculate marginal tamping costs

with respect to track settlement – see eq. (8-5) and eq. (8-6). A discount rate of 3.5% is used, as recommended in the Transport Analysis Guidance (TAG) published by the UK Department for Transport.

The elasticities for the different linespeed scenarios are presented in Table 8.6. The marginal costs are expressed as an average marginal cost per km/h/1000 train-km since the increases in speed apply to all trains running on the line, which is 26,176 passenger trains per year. Although there are limited number of studies on the effect of changing linespeed on marginal costs, as a comparison based on visual inspection of reported data points in (Öberg et al., 2007) the difference in marginal cost for settlement between vehicles with speeds of 140 km/h and 200 km/h (16 tonne axle load) indicates an extra cost of SEK 224.40 per 1000 train-km in 2021 prices, and SEK (Swedish Krona) 3.74 per km/h/1000 train-km. Using the conversion rate £ 1 = SEK 12, the marginal cost is £0.400 per km/h/1000 train-km.

Although this is similar, albeit lower than the figures shown in Table 8.6, there are important differences between the analyses: 1) (Öberg et al., 2007) is based on changes in speed from 140 to 200 km/h, which is lower than the speeds considered in the scenarios in Table 8.6. This is important because higher speeds result in higher train-track dynamic effects; 2) At the lower speeds considered by (Öberg et al., 2007), the SD band between threshold values is wider than for higher speeds. For example, this analysis considers a SD change of 0.5mm (1-1.5mm), while later in this paper for freight analysis on a lower speed line considers a SD change of 0.7mm (1.5-2.4mm). Therefore, at lower speeds, the threshold will take longer to meet, thus lowering marginal cost. Further, it is likely that (Öberg et al., 2007) considered changes within the 3-25m wavelength range, while this work considers 3-35m; 3) (Öberg et al., 2007) uses costs from 2001. Industry changes (e.g. improvements in health and safety and sustainability) are likely to have resulted in tamping price costs rising above the standard measure of inflation. This will manifest as higher marginal costs when considering current prices.

Table 8.6 Marginal cost per km/h/1000 train-km with 200 km/h as the baseline

Scenario	Elasticity	Marginal cost, £ per km/h/1000 train-km
(A2) Increasing speed to 209 km/h	-2.78	1.445
(A3) Increasing speed to 217 km/h	-2.02	1.012
(A4) Increasing speed to 225 km/h	-1.55	0.750

8.5.2 The influence of Rolling stock movements on cost

The elasticities and marginal costs for the different scenarios of increased train movements are presented in Table 8.7. This indicates that adding 1 passenger train per day has a similar influence on tamping costs as adding 2 freight trains per day, whilst the highest marginal cost is generated by adding 1 freight train per day.

These costs are lower than, but in the same order of magnitude as, the marginal costs in the econometric literature on rail infrastructure maintenance costs. For example, the marginal cost per 1000 tonne-km for track maintenance in France (ECOPLAN/IMDM, 2020) is €0.380 and €0.934 for freight traffic and passenger traffic, respectively, which corresponds to £0.317 and £0.778 using the conversion rate £1 = €1.20. Note, however, that these are estimates that consider all types of track damages and track maintenance activities and not only settlement and tamping. Moreover, (Smith et al., 2021) make use of a hybrid model that combines engineering and econometric methods and reports marginal costs for track settlement for different vehicle types. The average marginal cost per 1000 tonne-km for settlement is £ 0.565 for a freight train and £ 0.456 for a passenger train (based on their model with explanatory variables for RCF, wear, and settlement). These costs are also higher than the marginal costs in Table 8.7, but this is expected since (Smith et al., 2021) consider costs for tamping as well as all other track maintenance activities that can be triggered by settlement.

The results in Table 8.7 are similar to the engineering results on the marginal cost for track settlement in (Andersson et al., 2016). Based on visual inspection of an illustration with marginal costs for passenger cars, locos, and coaches, the average marginal cost per 1000 tonne-km for a passenger train (1 loco and 11 cars) is SEK 1.119 in 2021 prices which is £ 0.093 using the conversion rate £ 1 = SEK 12. These trains are running at 160 km/h and the cars have an axle load at 13 tonnes. The corresponding cost for a coach with a vehicle speed at 200 km/h (axle load 16 tonnes) is £ 0.190. The average marginal cost per 1000 tonne-km for a freight train (1 loco and 50 wagons) is £ 0.185.

Table 8.7 Marginal cost per 1000 tonne-km

Scenario	Elasticity	Marginal cost, £ per 1000 tonne-km
(B) Adding 1 passenger train per day	-0.75	0.131
(C) Adding 1 freight train per day	-0.93	0.153
(D) Adding 2 freight trains per day	-0.87	0.134

8.6 Discussion

The preceding sections highlight the changes to track tamping intervals and costs when changing linespeed and adding additional tonnage. For both analyses, the initial compacted state of the ballast plays a dominant role. It is the initial cycles where settlement is most rapid, and during this period the train-induced dynamic stresses can rapidly alter the differential settlement characteristics of the track, thus exasperate changes in standard deviation. Therefore, as an example, regarding the aforementioned freight analysis, if the line was not assumed to have been recently renewed, then initial assumption of 100k cycles would be higher, and the marginal cost would be lower.

Further, differential settlement is closely related to dynamic train-track interaction, and thus affected by rolling stock properties. For freight vehicles, in practise there are often limited details related to their payload magnitudes, load distribution across neighbouring axles/cars and sometimes even rolling stock schedule. Also, freight vehicle characteristics (e.g. suspension) can vary vastly between trains.

Regarding costs, only the cost of vertical track geometry correction is considered, while the effect of additional damage is ignored (e.g. rolling contact fatigue). Although an average cost of tamping is assumed, this is subject to variability due to a wide range of factors. For example, how close is the nearest tamper stabling point, how long is the possession, is a pre- and post-work track recording vehicle run needed…etc. Note that the marginal costs in Table 8.6 and Table 8.7 can be re-calculated with respect to alternative unit costs (£ c_{new} in 2021 prices) using the multiplication factor $c_{new}/5625$, where 5625 is the unit cost (tamping cost per track kilometre) assumed in this paper.

Considering the above, it should be noted that the analysis in this paper is based upon a single set of simulation parameters, and the results are sensitive to these. When investigating the effect of speed and rolling stock characteristics in practise, it is recommended this should done on a case-by-case basis to maximise accuracy.

Chapter 9
Conclusions and recommendations

9.1 Conclusions

The main objective of this work is to develop numerical tools designed for efficiently and accurately predicting future track geometry. This study introduces a novel numerical approach, capable of predicting track irregularity evolution across various scenarios. It has the following novel characteristics:

1. It is solved using a mixed frequency-wavenumber and time-space approach. This optimised solution procedure then allows for the track geometry profile to be updated after every load passage
2. The track and ground are fully coupled and modelled explicitly. This allows for 3D stress fields to be computed, which are important for accurate settlement calculation
3. The effect of strain on track and ground material properties is accounted for using an iterative equivalent linear approach
4. Modified settlement laws are used that can account for the differing forces induced due to evolving track profiles.

Five aspects of the model were validated. These are its ability to accurately perform short-term prediction of both ballasted and slab tracks, its ability to accurately simulate track-ground dynamics and non-linearity, its ability to model train-track interaction, and its ability to predict future changes in vertical track profile. The validated model is used to perform the four main analyses, leading to the following conclusions:

a) The analysis confirms the significance of frequently updating the track geometry profile, especially in the context of softer soils. Furthermore, stiffer soils lead to significantly reduced settlement, emphasising the importance of a well-constructed track subgrade.
b) Considering the ballasted track, the majority of settlement arises from the ballast layer, due to the rearrangement of particles, rather than the earthworks. Considering the slab track, it is elevated bending stiffness results in a more uniform distribution of stress on the earthworks, resulting lower train-induced strains in the earthwork compared to the ballasted track. Ballasted track exhibits higher differential settlement compared to the slab track. At higher linespeeds the degradation of

track geometry is more pronounced for the ballasted track compared to slab. This increases further with additional axle passages.

c) Higher ballast fouling levels lead to faster deterioration in track geometry, particularly in the presence of moisture. When the ballast is heavily fouled and the moisture of fines is high, rapid deterioration occurs. Earthwork stiffness exacerbates the effects of ballast fouling and moisture content, leading to increased settlement when the earthworks are soft. This is in-part due to the distribution of deviatoric stress within the track-bed layers. Higher train speed increases differential settlement rate for all scenarios studied. However, the effect is low when the ballast has minimal fines and is kept dry. In contrast, when the ballast is heavily fouled and is subject to elevated levels of moisture, the track geometry degrades significantly faster when subject to higher speeds.

d) Additional train movements increase the rate of track degradation and marginal costs, particularly if the additional traffic is freight. This is because freight vehicles typically have one only layer of (stiff) suspension, thus generating elevated dynamic forces compared to passenger cars. If two freight trains are added per day it can cause a reduction of the tamping interval of 13%. Therefore if planning to increase linespeed or add additional freight traffic, the future cost of maintenance should be considered.

9.2 Recommendations for future work

In this section, suggestions for future work are proposed regarding improvements to the model and its potential other applications.

- Further refinement of the numerical tool could be explored, particularly in areas involving more advanced track geometries, such as considering different types of track systems or materials, as well as load dynamics, including various types of trains and scheduling.
- While this study highlighted the importance of updating the track geometry frequently, especially for softer soils, future research can focus on establishing a guideline for when and how often this updating should occur to optimise simulation runtime.
- An investigation of the cause-and-effect relationship between track geometry alterations and differential settlement will provide more comprehensive insights into best practices for track maintenance.
- In this study, the empirical settlement equations were formulated based on experimental data. It is recommended that subsequent research

undertakes more testing to delve deeper into the settlement behaviours of diverse railway materials under varying conditions.

- Regarding the simulation of concrete slab track, there is a variety of concrete slab track products in practice, including both precast and in-situ poured variants. Future research should aim to evaluate the performance and characteristics of each type under varying conditions. The 2.5D modelling procedure used in this study assumes that the concrete slab track is infinitely long and lacks expansion joints. As a result, it does not account for the additional plastic settlement caused by movements near these joints. Consequently, the findings are more indicative of slab track systems that have wider spacings between joints. To investigate the impacts of such discontinuities, a 3D model should be explored in future research.
- A novel ballast settlement equation was formulated that integrates both the ballast fouling index and the moisture of fines. This equation was subsequently employed to examine the impact of the fouling index and moisture of fines on fouled ballast in the context of dry subgrade conditions. A potential avenue for future studies would be to model saturated subgrades, aiming to discern the influences on differential settlement under varying climatic conditions.
- While this research provides valuable insights regarding rolling stock characteristics, the actual effect of speed and rolling stock characteristics can differ based on specific cases. When implementing these findings in real-world scenarios, it is advisable to conduct individual analyses tailored to the unique conditions of each case to ensure accuracy and appropriateness.
- The current model relies on the 2.5D technique (Step A), which assumes that the elastodynamic properties of the track in the direction of train movement are consistent with those of the 2D cross-section. This approach proves beneficial and computationally efficient during iterative simulations (Step B) when calculating differential settlement over a large number of load passages. However, caution is advised in its application, as the material properties of the real-life track may vary along the route.

References

Abadi, T., Le Pen, L., Zervos, A., Powrie, W., 2016. A Review and Evaluation of Ballast Settlement Models using Results from the Southampton Railway Testing Facility (SRTF). Procedia Engineering 143, 999–1006. https://doi.org/10.1016/j.proeng.2016.06.089

Ali, L., Amin, S., Wehbi, M., 2021. Backpropagation algorithms of neural networks to construct the railway track deterioration model. 2021 7th International Conference on Models and Technologies for Intelligent Transportation Systems, MT-ITS 2021. https://doi.org/10.1109/MT-ITS49943.2021.9529272

Alves Costa, P., 2010. Vibrações do sistema via-maciço induzidas por tráfego ferroviário. Modelação numérica e validação experimental.

Alves Costa, P., Calçada, R., Silva Cardoso, A., 2012. Track-ground vibrations induced by railway traffic: In-situ measurements and validation of a 2.5D FEM-BEM model. Soil Dynamics and Earthquake Engineering 32, 111–128. https://doi.org/10.1016/j.soildyn.2011.09.002

Alves Costa, P., Calçada, R., Silva Cardoso, A., Bodare, A., 2010. Influence of soil non-linearity on the dynamic response of high-speed railway tracks. Soil Dynamics and Earthquake Engineering 30, 221–235. https://doi.org/10.1016/j.soildyn.2009.11.002

Andersson, M., Björklund, G., Haraldsson, M., 2016. Marginal railway track renewal costs: A survival data approach. Transportation Research Part A: Policy and Practice 87, 68–77. https://doi.org/10.1016/j.tra.2016.02.009

Ando, K., Sunaga, M., Aoki, H., Haga, O., 2001. Development of slab tracks for Hokuriku Shinkansen line. Quarterly Report of RTRI (Railway Technical Research Institute) (Japan) 42, 35–41. https://doi.org/10.2219/rtriqr.42.35

Arcos, R., Soares, P.J., Alves Costa, P., Godinho, L., 2021. An experimental/numerical hybrid methodology for the prediction of railway-induced ground-borne vibration on buildings to be constructed close to existing railway infrastructures: Numerical validation and parametric study. Soil Dynamics and Earthquake Engineering 150, 106888. https://doi.org/10.1016/j.soildyn.2021.106888

Auersch, L., Said, S., 2019. Measurement of slab track behaviour at different sites, in: Proceedings of the 26th International Congress on Sound and Vibration, ICSV 2019. pp. 1–8.

Auersch, L., Said, S., 2017. Track-soil dynamics – Calculation and measurement of damaged and repaired slab tracks. Transportation Geotechnics 12, 1–14. https://doi.org/10.1016/j.trgeo.2017.06.003

Bai, L., Liu, R., Sun, Q., Wang, F., Xu, P., 2015. Markov-based model for the prediction of railway track irregularities. Proceedings of the Institution of Mechanical Engineers, Part F: Journal of Rail and Rapid Transit 229, 150–159. https://doi.org/10.1177/0954409713503460

Bastin, R., 2006. Development of German non-ballasted track forms. Proceedings of the Institution of Civil Engineers: Transport 159, 25–39. https://doi.org/10.1680/tran.2006.159.1.25

Bian, X., Jiang, H., Chang, C., Hu, J., Chen, Y., 2015. Track and ground vibrations generated by high-speed train running on ballastless railway with excitation of vertical track irregularities. Soil Dynamics and

Earthquake Engineering 76, 29–43. https://doi.org/10.1016/j.soildyn.2015.02.009

Biot, M.A., 1962. Mechanics of deformation and acoustic propagation in porous media. Journal of Applied Physics 33, 1482–1498. https://doi.org/10.1063/1.1728759

Burrow, M.P.N., Shi, J., Wehbi, M., Ghataora, G.S., 2017. Assessing the damaging effects of railway dynamic wheel loads on railway foundations. Transportation Research Record 2607, 62–73. https://doi.org/10.3141/2607-09

Charoenwong, C., Connolly, D.P., Colaço, A., Alves Costa, P., Woodward, P.K., Romero, A., Galvín, P., 2023. Railway slab vs ballasted track: A comparison of track geometry degradation. Construction and Building Materials 378, 131121. https://doi.org/10.1016/j.conbuildmat.2023.131121

Charoenwong, C., Connolly, D.P., Costa, P.A., Galvín, P., Romero, A., 2024. The effect of ballast moisture content and fouling index on railway track settlement. Transportation Geotechnics 45, 101193. https://doi.org/10.1016/j.trgeo.2024.101193

Charoenwong, C., Connolly, D.P., Odolinski, K., Alves Costa, P., Galvín, P., Smith, A., 2022. The effect of rolling stock characteristics on differential railway track settlement: An engineering-economic model. Transportation Geotechnics 37, 100845. https://doi.org/10.1016/j.trgeo.2022.100845

Charoenwong, C, Connolly, D.P., Woodward, P.K., Galvín, P., Alves Costa, P., 2022. Analytical forecasting of long-term railway track settlement. Computers and Geotechnics 143, 104601. https://doi.org/10.1016/j.compgeo.2021.104601

Chen, C., McDowell, G.R., 2016. An investigation of the dynamic behaviour of track transition zones using discrete element modelling. Proceedings of the Institution of Mechanical Engineers, Part F: Journal of Rail and Rapid Transit 230, 117–128. https://doi.org/10.1177/0954409714528892

Chumyen, P., Connolly, D.P., Woodward, P.K., Markine, V., 2023. A comparison of earthwork designs for railway transition zones. Construction and Building Materials 395. https://doi.org/10.1016/j.conbuildmat.2023.132295

Colaço, A., Costa, P.A., Connolly, D.P., 2016. The influence of train properties on railway ground vibrations. Structure and Infrastructure Engineering 12, 517–534. https://doi.org/10.1080/15732479.2015.1025291

Connolly, D., Giannopoulos, A., Forde, M.C., 2013. Numerical modelling of ground borne vibrations from high speed rail lines on embankments. Soil Dynamics and Earthquake Engineering 46, 13–19. https://doi.org/10.1016/j.soildyn.2012.12.003

Connolly, D.P., Costa, P.A., 2020. Geodynamics of very high speed transport systems. Soil Dynamics and Earthquake Engineering 130, 105982. https://doi.org/10.1016/j.soildyn.2019.105982

Connolly, D.P., Dong, K., Alves Costa, P., Soares, P., Woodward, P.K., 2020. High speed railway ground dynamics: a multi-model analysis. International Journal of Rail Transportation 8, 324–346. https://doi.org/10.1080/23248378.2020.1712267

Cooley, J.W., Tukey, J.W., 1965. An algorithm for the machine calculation of complex Fourier series. Mathematics of computation 19, 297–301.

Costa, P.A., Calçada, R., Cardoso, A.S., 2012. Influence of train dynamic modelling strategy on the prediction of track-ground vibrations induced

by railway traffic. Proceedings of the Institution of Mechanical Engineers, Part F: Journal of Rail and Rapid Transit 226, 434–450. https://doi.org/10.1177/0954409711433686

Dahlberg, T., 2001. Some railroad settlement models - A critical review. Proceedings of the Institution of Mechanical Engineers, Part F: Journal of Rail and Rapid Transit 215, 289–300. https://doi.org/10.1243/0954409011531585

Dong, K., Connolly, D.P., Laghrouche, O., Woodward, P.K., Alves Costa, P., 2019. Non-linear soil behaviour on high speed rail lines. Computers and Geotechnics 112, 302–318. https://doi.org/10.1016/j.compgeo.2019.03.028

Dong, K., Connolly, D.P., Laghrouche, O., Woodward, P.K., Alves Costa, P., 2018. The stiffening of soft soils on railway lines. Transportation Geotechnics 17, 178–191. https://doi.org/10.1016/j.trgeo.2018.09.004

Dyvik, R., Kaynia, A.M., 2018. Large-Scale Triaxial Tests on Railway Embankment Material, in: Stark, T., Swan, R., Szecsy, R. (Eds.), Railroad Ballast Testing and Properties. ASTM International, West Conshohocken, PA, pp. 173–190. https://doi.org/10.1520/STP160520170031

ECOPLAN/IMDM, 2020. Modelling railway infrastructure maintenance and renewal costs in France. Overview of estimates. Final report. (mimeo).

EN 13848-5:2008+A1, 2010. Railway applications — Track — Track geometry quality — Part 5: Geometric quality levels — Plain line.

Esen, A.F., Woodward, P.K., Laghrouche, O., Čebašek, T.M., Brennan, A.J., Robinson, S., Connolly, D.P., 2021. Full-scale laboratory testing of a geosynthetically reinforced soil railway structure. Transportation Geotechnics 28. https://doi.org/10.1016/j.trgeo.2021.100526

Esveld, C., 2001. Modern railway track. MRT-productions Zaltbommel.

Federal Railroad Administration, 1980. Statistical Representations of Track Geometry : Volume I. US Department of Transportation, Washington, D.C.

Ferreira, L., Murray, M.H., 1997. Modelling rail track deterioration and maintenance: Current practices and future needs. Transport Reviews 17, 207–221. https://doi.org/10.1080/01441649708716982

Ferreira, P.A., 2010. Modelling and prediction of the dynamic b haviour of railway infrastructures at very high speeds.

François, S., Schevenels, M., Lombaert, G., Degrande, G., 2010. A 2.5D displacement-based PML for elastodynamic wave propagation. Computational Mechanics 2–3.

Grossoni, I., Powrie, W., Zervos, A., Bezin, Y., Le Pen, L., 2021. Modelling railway ballasted track settlement in vehicle-track interaction analysis. Transportation Geotechnics 26, 100433. https://doi.org/10.1016/j.trgeo.2020.100433

Guo, Y., Xie, J., Fan, Z., Markine, V., Connolly, D.P., Jing, G., 2022. Railway ballast material selection and evaluation: A review. Construction and Building Materials 344, 128218. https://doi.org/10.1016/j.conbuildmat.2022.128218

Guo, Y., Zhai, W., 2018. Long-term prediction of track geometry degradation in high-speed vehicle–ballastless track system due to differential subgrade settlement. Soil Dynamics and Earthquake Engineering 113, 1–11. https://doi.org/10.1016/j.soildyn.2018.05.024

Guo, Y., Zhao, C., Markine, V., Jing, G., Zhai, W., 2020. Calibration for discrete element modelling of railway ballast: A review. Transportation Geotechnics 23, 100341. https://doi.org/10.1016/j.trgeo.2020.100341

Hardin, B.O., Drnevich, V.P., 1972. Shear modulus and damping in soils: design equations and curves. Journal of the Soil mechanics and Foundations Division 98, 667–692.

Hardy, G.H., Littlewood, J.E., n.d. An additional note on Parseval's theorem. Mathematische Zeitschrift. 34.

Indraratna, B., Nimbalkar, S., 2013. Stress-Strain Degradation Response of Railway Ballast Stabilized with Geosynthetics. Journal of Geotechnical and Geoenvironmental Engineering 139, 684–700. https://doi.org/10.1061/(asce)gt.1943-5606.0000758

Indraratna, B., Thakur, P.K., Vinod, J.S., 2010. Experimental and numerical study of railway ballast behavior under cyclic loading. International Journal of Geomechanics 10, 136–144.

Indraratna, B., Thakur, P.K., Vinod, J.S., Salim, W., 2012. Semiempirical Cyclic Densification Model for Ballast Incorporating Particle Breakage. International Journal of Geomechanics 12, 260–271. https://doi.org/10.1061/(asce)gm.1943-5622.0000135

Ionescu, D., 2004. Ballast Degradation and Measurement of Ballast Fouling, in: Railway Engineering Proceedings. pp. 169–180.

Ishibashi, I., Zhang, X., 1993. Unified dynamic shear moduli and damping ratio of sand and clay. Soils and Foundations 33, 182–191.

Karlström, A., Boström, A., 2006. An analytical model for train-induced ground vibrations from railways. Journal of Sound and Vibration 292, 221–241. https://doi.org/10.1016/j.jsv.2005.07.041

Kawaguchi, A., Miwa, M., Terada, K., 2005. Actual data analysis of alignment irregularity growth and its prediction model. Quarterly Report of RTRI (Railway Technical Research Institute) (Japan) 46, 262–268. https://doi.org/10.2219/rtriqr.46.262

Knothe, K., Wu, Y., 1998. Receptance behaviour of railway track and subgrade. Archive of Applied Mechanics 68, 457–470. https://doi.org/10.1007/s004190050179

Kouroussis, G., Connolly, D.P., Verlinden, O., 2014. Railway-induced ground vibrations – a review of vehicle effects. International Journal of Rail Transportation 2, 69–110. https://doi.org/10.1080/23248378.2014.897791

Lamprea-Pineda, A.C., Connolly, D.P., Hussein, M.F.M., 2022. Beams on elastic foundations – A review of railway applications and solutions. Transportation Geotechnics 33, 100696. https://doi.org/10.1016/j.trgeo.2021.100696

Lee, J.S., Hwang, S.H., Choi, I.Y., Choi, Y., 2020. Deterioration Prediction of Track Geometry Using Periodic Measurement Data and Incremental Support Vector Regression Model. Journal of Transportation Engineering, Part A: Systems 146, 04019057. https://doi.org/10.1061/jtepbs.0000291

Lekarp, F., Isacsson, U., Dawson, A., 2000. State of the art. II: Permanent strain response of unbound aggregates. Journal of Transportation Engineering 126, 76–83. https://doi.org/10.1061/(ASCE)0733-947X(2000)126:1(76)

Li, D., 1994. Railway track granular layer thickness design based on subgrade performance under repeated loading. University of Massachusetts, Amherst, Mass.

Li, D., Hyslip, J., Sussmann, T., Chrismer, S., 2015. Railway geotechnics. CRC Press.

Li, D., Selig, E.T., 1996. Cumulative Plastic Deformation for Fine-Grained Subgrade Soils. Journal of Geotechnical Engineering 122, 1006–1013. https://doi.org/10.1061/(asce)0733-9410(1996)122:12(1006)

Li, X., Ekh, M., Nielsen, J.C.O., 2016. Three-dimensional modelling of differential railway track settlement using a cycle domain constitutive model. International Journal for Numerical and Analytical Methods in Geomechanics 40, 1758–1770.

Liu, J., Xiao, J., 2010. Experimental Study on the Stability of Railroad Silt Subgrade with Increasing Train Speed. Journal of Geotechnical and Geoenvironmental Engineering 136, 833–841. https://doi.org/10.1061/(asce)gt.1943-5606.0000282

Lopes, P., Costa, P.A., Calçada, R., Cardoso, A.S., 2013. Numerical modeling of vibrations induced in tunnels: A 2.5D FEM-PML approach, in: Traffic Induced Environmental Vibrations and Controls: Theory and Application.

Lopes, P., Costa, P.A., Ferraz, M., Calçada, R., Cardoso, A.S., 2014. Numerical modeling of vibrations induced by railway traffic in tunnels: From the source to the nearby buildings. Soil Dynamics and Earthquake Engineering 61–62, 269–285. https://doi.org/10.1016/j.soildyn.2014.02.013

Madshus, C., Kaynia, A.M., 2000. High-speed railway lines on soft ground: dynamic behaviour at critical train speed. Journal of Sound and Vibration 231, 689–701. https://doi.org/10.1006/jsvi.1999.2647

Marolt Čebašek, T., Esen, A.F., Woodward, P.K., Laghrouche, O., Connolly, D.P., 2018. Full scale laboratory testing of ballast and concrete slab tracks under phased cyclic loading. Transportation Geotechnics 17, 33–40. https://doi.org/10.1016/j.trgeo.2018.08.003

Menan Hasnayn, M., John McCarter, W., Woodward, P.K., Connolly, D.P., Starrs, G., 2017. Railway subgrade performance during flooding and the post-flooding (recovery) period. Transportation Geotechnics 11, 57–68. https://doi.org/10.1016/j.trgeo.2017.02.002

Miura, S., Takai, H., Uchida, M., Fukada, Y., 1998. The Mechanism of Railway Tracks. Japan Railway & Transport Review 3, 38–45.

Network Rail, 2015. Track geometry - Inspections and minimum actions - NR/L2/TRK/001/mod11. London, UK.

Neuhold, J., Landgraf, M., Marschnig, S., Veit, P., 2020. Measurement Data-Driven Life-Cycle Management of Railway Track. Transportation Research Record 2674, 685–696. https://doi.org/10.1177/0361198120946007

Nielsen, J.C.O., Li, X., 2018. Railway track geometry degradation due to differential settlement of ballast/subgrade – Numerical prediction by an iterative procedure. Journal of Sound and Vibration 412, 441–456. https://doi.org/10.1016/j.jsv.2017.10.005

Öberg, J., Andersson, E., Gunnarsson, J., 2007. Track access charging with respect to vehicle characteristics. Rapport LA-BAN 31, 2007.

ORE, 1970. Question D71: Stresses in the Rails, the Ballast and in the Formation Resulting from Traffic Loads. Stresses in the formation (results of the third phase ; measurements under dynamic conditions). International Union of Railways, Office for Research and Experiments.

Profillidis, V.A., 2000. Railway engineering.

Qian, Y., Tutumluer, E., Hashash, Y.M.A., Ghaboussi, J., 2022. Triaxial testing of new and degraded ballast under dry and wet conditions. Transportation Geotechnics 34, 100744. https://doi.org/10.1016/j.trgeo.2022.100744

Ramos, A., Gomes Correia, A., Calçada, R., Alves Costa, P., Esen, A., Woodward, P.K., Connolly, D.P., Laghrouche, O., 2021. Influence of track foundation on the performance of ballast and concrete slab tracks under cyclic loading: Physical modelling and numerical model calibration. Construction and Building Materials 277, 122245. https://doi.org/10.1016/j.conbuildmat.2021.122245

Ramos, A., Gomes Correia, A., Indraratna, B., Ngo, T., Calçada, R., Costa, P.A., 2020. Mechanistic-empirical permanent deformation models: Laboratory testing, modelling and ranking. Transportation Geotechnics 23. https://doi.org/10.1016/j.trgeo.2020.100326

Rollins, K.M., Singh, M., Roy, J., AKKOÇ, B., 2020. Simplified Equations for Shear-Modulus Degradation and Damping of Gravels. Journal of Geotechnical and Geoenvironmental Engineering 146, 04020076. https://doi.org/10.1061/(asce)gt.1943-5606.0002300

Sasidharan, M., Burrow, M.P.N., Ghataora, G.S., Marathu, R., 2022. A risk-informed decision support tool for the strategic asset management of railway track infrastructure. Proceedings of the Institution of Mechanical Engineers, Part F: Journal of Rail and Rapid Transit 236, 183–197. https://doi.org/10.1177/09544097211038373

Sato, Y., 1995. Japanese Studies on Deterioration of Ballasted Track. Vehicle System Dynamics 24, 197–208. https://doi.org/10.1080/00423119508969625

Saussine, G., Cholet, C., Gautier, P.E., Dubois, F., Bohatier, C., Moreau, J.J., 2006. Modelling ballast behaviour under dynamic loading. Part 1: A 2D polygonal discrete element method approach. Computer Methods in Applied Mechanics and Engineering 195, 2841–2859. https://doi.org/10.1016/j.cma.2005.07.006

Sayeed, M.A., Shahin, M.A., 2018. Design of ballasted railway track foundations using numerical modelling. Part I: Development1. Canadian Geotechnical Journal 55, 353–368. https://doi.org/10.1139/cgj-2016-0633

Selig, E.T., Waters, J.M., 1994. Track geotechnology and substructure management, University of Massachusetts USA. https://doi.org/10.1680/tgasm.20139

Shan, Y., Zhou, S., Zhou, H., Wang, B., Zhao, Z., Shu, Y., Yu, Z., 2017. Iterative method for predicting uneven settlement caused by high-speed train loads in transition-zone subgrade. Transportation Research Record 2607, 7–14. https://doi.org/10.3141/2607-02

Sharma, S., Cui, Y., He, Q., Mohammadi, R., Li, Z., 2018. Data-driven optimization of railway maintenance for track geometry. Transportation Research Part C: Emerging Technologies 90, 34–58. https://doi.org/10.1016/j.trc.2018.02.019

Sheng, X., 2001. Ground vibrations generated from trains. University of Southampton.

Sheng, X., Jones, C.J.C., Thompson, D.J., Wu, T.X., Thompson, D.J., 2003. A comparison of a theoretical model for quasi-statically and dynamically induced environmental vibration from trains with measurements. Journal of Sound and Vibration 267, 621–635. https://doi.org/10.1016/S0022-460X(03)00728-4

Shenton, M.J., 1985. Ballast deformation and track deterioration. Track Technology 253–265.

Shi, J., Chan, A.H., Burrow, M.P.N., 2012. Influence of unsupported sleepers on dynamic responses of railroad embankment below a heavy haul railway line using simulation techniques. RRUKA Annual Conference 1–6.

Shi, S., Gao, L., Hou, B., Xu, M., Xiao, Y., 2022. Numerical investigation on multiscale mechanical properties of ballast bed in dynamic stabilization maintenance. Computers and Geotechnics 144, 104649. https://doi.org/10.1016/j.compgeo.2022.104649

Shih, J.Y., Grossoni, I., Bezin, Y., 2019. Settlement analysis using a generic ballasted track simulation package. Transportation Geotechnics 20, 100249. https://doi.org/10.1016/j.trgeo.2019.100249

Shih, J.Y., Thompson, D.J., Zervos, A., 2017. The influence of soil nonlinear properties on the track/ground vibration induced by trains running on soft ground. Transportation Geotechnics 11, 1–16. https://doi.org/10.1016/j.trgeo.2017.03.001

Shimatake, M., 1997. A track maintenance model for high-speed rail: a systems dynamics approach. Massachusetts Institute of Technology.

Smith, A.S.J., Odolinski, K., Hossein-Nia, S., Jönsson, P.A., Stichel, S., Iwnicki, S., Wheat, P., 2021. Estimating the marginal maintenance cost of different vehicle types on rail infrastructure. Proceedings of the Institution of Mechanical Engineers, Part F: Journal of Rail and Rapid Transit 235, 1191–1202. https://doi.org/10.1177/0954409721991309

Smith, I.M., Griffiths, D.V., Margetts, L., 2013. Programming the finite element method. John Wiley & Sons.

Suiker, A.S.J., de Borst, R., 2003. A numerical model for the cyclic deterioration of railway tracks. International Journal for Numerical Methods in Engineering 57, 441–470. https://doi.org/10.1002/nme.683

Tadeu, A.J.B., Kausel, E., 2000. Green’s functions for two-and-a-half-dimensional elastodynamic problems. Journal of Engineering Mechanics, ASCE 134, 1093–1097.

Tayabji, S.D., Bilow, D., 2001. Concrete slab track state of the practice. Transportation Research Record 87–96. https://doi.org/10.3141/1742-11

Thom, N.H., Brown, S.F., 1987. Effect of moisture on the structural performance of a crushed-limestone road base. Transportation Research Record 50–56.

Thompson, D., 2008. Railway noise and vibration: mechanisms, modelling and means of control. Elsevier.

Vale, C., M. Lurdes, S., 2013. Stochastic model for the geometrical rail track degradation process in the Portuguese railway Northern Line. Reliability Engineering and System Safety 116, 91–98. https://doi.org/10.1016/j.ress.2013.02.010

Wu, T.X., Thompson, D.J., 2001. Vibration analysis of railway track with multiple wheels on the rail. Journal of Sound and Vibration 239, 69–97. https://doi.org/10.1006/jsvi.2000.3157

Xu, Q., Xiao, Z., Liu, T., Lou, P., Song, X., 2015. Comparison of 2D and 3D prediction models for environmental vibration induced by underground railway with two types of tracks. Computers and Geotechnics 68, 169–183. https://doi.org/10.1016/j.compgeo.2015.04.011

Yan, T.H., Corman, F., 2020. Assessing and Extending Track Quality Index for Novel Measurement Techniques in Railway Systems. Transportation

Research Record 2674, 24–36. https://doi.org/10.1177/0361198120923661

Yu, Z., Woodward, P.K., Laghrouche, O., Connolly, D.P., 2019. True triaxial testing of geogrid for high speed railways. Transportation Geotechnics 20, 100247. https://doi.org/10.1016/j.trgeo.2019.100247

Zhai, W., 2020. Vehicle--Track Coupled Dynamics Models, in: Vehicle--Track Coupled Dynamics: Theory and Applications. Springer Singapore, Singapore, pp. 17–149. https://doi.org/10.1007/978-981-32-9283-3_2

Zuada Coelho, B., Varandas, J.N., Hijma, M.P., Zoeteman, A., 2021. Towards network assessment of permanent railway track deformation. Transportation Geotechnics 29. https://doi.org/10.1016/j.trgeo.2021.100578